DISSERTATION

HIGH-POWER DEEP-UV LASER FOR IMPROVED AND NOVEL EXPERIMENTS ON HYDROGEN

Submitted by

Zakary Neumann Burkley

Department of Physics

In partial fulfillment of the requirements

For the Degree of Doctor of Philosophy

Colorado State University

Fort Collins, Colorado

Spring 2019

Doctoral Committee:

Advisor: Dylan Yost

Jacob Roberts
Mark Bradley
Carmen Menoni

ABSTRACT

HIGH-POWER DEEP-UV LASER FOR IMPROVED AND NOVEL EXPERIMENTS ON HYDROGEN

This dissertation details the design, performance, and cavity enhancement of a novel, high-power coherent 243.1 nm laser system, and through simulations, its ability to trap hydrogen in a magic wavelength optical trap. This wavelength of light is necessary to address the 1S–2S two-photon transition in hydrogen, and the primary motivation behind development of this laser system is obtaining high enough 243.1 nm powers for two-photon cooling of hydrogen. Due to the light mass of hydrogen, high precision spectroscopy of hydrogen is limited by unwanted motional effects, which could be mitigated with laser cooling and confinement in an optical trap. Besides laser cooling, a high power deep-UV laser system at this wavelength has great utility for improving spectroscopy of hydrogen and other exotic simple systems.

High-power fiber lasers from 1-1.2 μm have flourished as a result of advances in ytterbium(Yb)-doped fiber amplifiers. In addition, high-power Yb-fiber lasers between 975-980 nm have also been developed—a notable accomplishment due to gain competition in the > 1 μm spectral region. These systems initially lacked sufficiently narrow spectral bandwidth for efficient harmonic generation, motivating further development since there is significant interest in frequency doubling and quadrupling these sources to produce coherent blue radiation and deep-UV radiation. Here, we generate coherent, high-power deep-UV radiation through frequency quadrupling of a high-power, highly coherent Yb-fiber amplifier at 972.5 nm. The Yb-fiber amplifier system consists of a frequency stabilized master oscillator power amplifier (MOPA) that can be referenced to a coherent frequency comb. This MOPA can be amplified to > 10 W of narrow linewidth power at 972.5 nm in the Yb-fiber amplifier. This is a technically challenging and notable result for this wavelength as gain is much more readily obtained in Yb-doped fibers at the absorption/emission cross-section

peak near 975 nm and in the > 1 μm spectral region where the emission cross-section is much larger than the absorption cross-section. This system successfully combated unwanted gain at these wavelengths by using a relatively short (≈ 10 cm), angle-polished Yb-fiber with a large core-cladding ratio, along with aggressive spectral filtering and large amounts of seed power at 972.5 nm.

With this narrow linewidth Yb-fiber amplifier, efficient frequency conversion of high power 972-976 nm radiation to 243-244 nm radiation is possible through intracavity doubling. Through successive resonant doubling stages, this system demonstrates > 1 W of highly stable, continuous-wave (CW) 243.1 nm power. To the author's knowledge, this is a record amount of CW deep-UV power below 266 nm, and is made possible thanks to advances in the production of a relatively new non-linear crystal for robust deep-UV generation, cesium lithium borate (CLBO). The precise frequency control of this radiation is established via excitation of the 1S–2S transition in hydrogen, and the viability for two-photon laser cooling on this transition is shown through enhancement of this power to > 30 W of intracavity power in a deep-UV enhancement cavity. At these powers, UV-induced mirror degradation was observed and mitigated by flushing the enhancement cavity mirrors with ultra-pure oxygen. With these powers, rapid two-photon laser cooling of a hydrogen atomic beam approaches reality. The 243.1 nm powers offered by this laser system also offer unique methods for capturing hydrogen in an optical trap. Explored via simulations, single optical scatter capture of hydrogen in a magic wavelength dipole trap is demonstrated, promising exciting new avenues for high precision spectroscopy of hydrogen.

ACKNOWLEDGEMENTS

The work presented in this thesis is the result of the hard work and support from many wonderful people. First and foremost, I would like to thank my wife, Jillian, for always supporting my pursuit of a physics education, pushing me to excel at all aspects of my life, and starting our own, incredible family during our time in Fort Collins. My family's constant uplifting encouragement and visits always elevated my spirits. Mom, Dad, and Keenan, thank you. I wouldn't be here without you.

The entirety of this work wouldn't be possible without my advisor and mentor, Dylan Yost. Building an atomic and optical physics lab from scratch and working alongside you has been a privilege and tremendous learning experience. You have motivated me to continually hone my physical intuition and scientific scrutiny. Dylan, I appreciate your humor, genuine curiosity and steadfast dedication to understanding questions of any kind. Thank you for everything.

During my research, I had the opportunity to work with three outstanding colleagues, Adam, Cory, and Scoop. The work presented in this thesis wouldn't be possible without them, and working alongside these three was always an enjoyable experience. Near the end of my work, I had the chance to work alongside Michael Morrison. Michael's kindness and devotion to mentoring students continues to positively impact me, and I know he will continue to be a great asset to future AMO graduate students in our department.

Outside of these main individuals there are many more to thank. Jacob Roberts, the department chair, always provided sound advice and direction to relevant scientific literature. Our group had joint meetings with Jacob Roberts' group, which always help shed light and solutions to any problems we were facing in our lab. Bob Adame, the machinist for the physics shop was a patient and wise and teacher. Building an AMO lab from scratch, Bob's advice and help was invaluable for my research and our lab. Brian Jones, director of the Little Shop of Physics, organized teaching development lunches for graduate students, and always motivated us to get out there and inspire others through physics education. I am also extremely grateful for my committee consisting of

Mark Bradley, Carmen Menoni, and Jacob Roberts. Your time and comments have strengthened the quality and understanding of my research.

Working behind the scenes, the front office staff have helped in countless ways during my time here. Thank you Veronica, Vanay, Wendy, Sharon, Alicia, and Kristin for all the questions you have helped me answer and issues you have helped me straighten out. Thank you to the AMO professors that helped build up the reputable program in our department with high quality research: Siu Au Lee, Bill Fairbank, Dave Krueger, and Steve Lundeen. Thank you to all the professors that contributed to my graduate education, and to Marty Gelfand for organizing all the Teaching Assistants. Lastly, thank you to all the graduate students in the department that have contributed to my great experience here in the CSU physics department, and CSU as a whole. Colorado State University is a fantastic institution and I cannot imagine having pursued my PhD anywhere else.

DEDICATION

To the brightest light sources in my life, Jaxon and Jillian.

TABLE OF CONTENTS

ABSTRACT ii
ACKNOWLEDGEMENTS iv
DEDICATION vi
LIST OF TABLES ix
LIST OF FIGURES x

Chapter 1 Motivation 1
1.1 Thesis Outline 6

Chapter 2 Yb-Fiber Amplifier at 972.5 nm 8
2.1 Introduction 8
2.2 Brief History of Fiber Lasers 10
2.2.1 Birth of the Yb-Fiber Laser 11
2.3 Gain near the Absorption & Emission Cross Section Peak 14
2.3.1 Photodarkening 15
2.3.2 Gain Competition at 975 nm Operation 17
2.3.3 Gain Competition at 972.5 nm Operation 19
2.4 Yb-Fiber Amplifier at 972.5 nm 20
2.4.1 Preventing Photodarkening and Parasitic Gain in our Design 20
2.4.2 Seed Laser Design 21
2.4.3 Yb-fiber Amplifier Design 24
2.4.4 Yb-fiber Amplifier Performance 29
2.4.5 Power Scaling and Power Stability 30
2.5 Frequency Stabilization and Coherent Comb Lock 34
2.6 Conclusion 39

Chapter 3 Watt-level, Coherent Deep-UV Generation via Frequency Quadrupling 41
3.1 Introduction 41
3.2 Frequency Doubling Theory and Considerations 42
3.2.1 SHG Efficiency with Gaussian Beams 42
3.2.2 CW Enhancement Cavity 49
3.2.3 Second Harmonic Generation in an Enhancement Cavity 52
3.2.4 ABCD Matrix Analysis of Bowtie Cavity with Brewster-cut Non-linear Crystal and Internal Focus 57
3.3 Frequency Doubling and Quadrupling Results 62
3.3.1 486.3 nm Generation 63
3.3.2 243.1 nm Generation 69
3.4 Conclusion 75

Chapter 4 Cavity-enhanced Deep-UV Laser . . . 77
4.1 Introduction . . . 77
4.2 One and Two-photon Scattering of a Two-level Atom . . . 78
4.3 UV Enhancement Cavity . . . 91
4.3.1 243.1 nm Laser Output and Mode-Matching . . . 92
4.3.2 Cavity Performance . . . 95
4.4 Conclusion . . . 100

Chapter 5 Single Optical Scatter Capture of Hydrogen in a Magic Wavelength Dipole Trap . . . 101
5.1 Introduction . . . 101
5.2 AC Stark Shift and Magic Wavelength . . . 102
5.3 Single Scatter Capture Feasibility and Procedure . . . 105
5.4 Simulation Procedure . . . 111
5.5 Simulation Results . . . 112
5.5.1 Single Trajectory . . . 112
5.5.2 Multiple Trajectories . . . 116
5.6 Conclusion . . . 121

Chapter 6 Summary . . . 122

Bibliography . . . 127

LIST OF TABLES

2.1 ECDL Output Power 22
2.2 TA Output Power 24
2.3 Pump Output and Absorbed Power 27
2.4 High Power Pump Output Power 32

3.1 SHG Parameters 46

LIST OF FIGURES

1.1 Single-photon versus two-photon cooling scheme for hydrogen 3
1.2 Simplified design of a high-power 243.1 nm laser system via a frequency-quadrupled, high-power and highly-coherent Yb-fiber amplifier at 972.5 nm 6

2.1 Small increases in 972.5 nm power result in large gains at 243.1 nm 9
2.2 Absorption and emission cross-section of Yb^{3+} in a phosphosilicate host 9
2.3 Energy structure of Yb^{3+} in lattice of an optical fiber 12
2.4 Key technologies for high power fiber lasers: High-power laser diode arrays and double-clad fibers 13
2.5 Yb-fiber amplifier and MOPA design 23
2.6 Shift of pump wavelength with current 28
2.7 Yb fiber amplifier spectrum with and without seed 29
2.8 6.4 W of 972.5 nm power with predicted power scaling 30
2.9 10.8 W of amplified 972.5 nm radiation 33
2.10 Long term operation of > 10 W of 972.5 nm power 34
2.11 Schematic of the 972.5 nm frequency stabilization and locking system 35
2.12 RF spectrum of coherent beat note between 972.5 nm MOPA and frequency comb . . . 36
2.13 RF spectrum of pre-stabilization cavity in-loop error signal 37
2.14 RF spectrum of frequency comb, 972.5 nm beat note with comb, and pre-stabilization cavity 38

3.1 Walkoff in a nonlinear crystal with type-I critical phase matching 47
3.2 Second Harmonic Generation in an external bow tie cavity with Brewster cut non-linear crystal 50
3.3 Second harmonic power versus fundamental input power in an external resonator for optimal and non-optimal input coupler values 56
3.4 Impedance mismatched power versus fundamental input power for optimal and non-optimal input coupler values 57
3.5 ABCD analysis of bow tie cavity with curved mirrors and Brewster elements 58
3.6 Folding angle versus horizontal and vertical focus in center of non-linear crystal 61
3.7 Beam waist at different positions in cavity for different folding angles 62
3.8 Frequency quadrupling through two successive SHG enhancement cavities 63
3.9 Generation of 2.4 W of 486.3 nm power using LBO in a resonant doubling stage 65
3.10 Impedance mismatching for LBO doubling cavity using pre power-scaled Yb-fiber amplifier 65
3.11 Generation of 4.2 W of 486.3 nm power using LBO in a resonant doubling stage 66
3.12 Impedance mismatching for LBO doubling cavity using post power-scaled Yb-fiber amplifier 67
3.13 Highly stable, high power 486.3 nm operation on hour timescales 68
3.14 Generation of 330 mW of 243.1 nm power using BBO in a resonant doubling stage . . 70
3.15 Generation of 530 mW of 243.1 nm power using CLBO in a resonant doubling stage . 70

3.16 Impedance mismatching for CLBO doubling cavity using pre power-scaled Yb-fiber amplifier . . . 71
3.17 Generation of 1.4 W of 243.1 nm power using CLBO in a resonant doubling stage . . . 72
3.18 Impedance mismatching for CLBO doubling cavity using post power-scaled Yb-fiber amplifier . . . 72
3.19 Highly stable, high power 243.1 nm operation on hour timescales . . . 73
3.20 Demonstration of the precise frequency control of our high power 243.1 nm laser system via excitation of the 1S-2S transition in hydrogen . . . 74

4.1 Full design of high-power Yb-amplifier laser system with frequency quadrupling to 243.1 nm . . . 77
4.2 Two-photon cooling cycle for atomic hydrogen . . . 79
4.3 Quenching the 2S state via mixing with the 2P state . . . 86
4.4 Quick estimation of 1S-2S two-photon transition matrix element . . . 88
4.5 Two-photon scattering rates for Doppler-free and non-Doppler-free processes . . . 89
4.6 Deep-UV enhancement cavity design . . . 92
4.7 Beam profile of high power 243.1 nm radiation after beam shaping . . . 94
4.8 Mode matching to deep-UV enhancement cavity . . . 97
4.9 Deep-UV enhancement and intracavity power as function of 243.1 nm input power . . . 98

5.1 Single scatter capture of hydrogen in a dipole trap with UV cooling laser. . . . 106
5.2 Probability of single scatter capture in dipole trap for various atomic velocities and trap depths . . . 107
5.3 The proposed experimental setup for capturing hydrogen in a dipole trap . . . 109
5.4 Energy level structure for loading hydrogen into a dipole trap. . . . 110
5.5 Capture probability in dipole trap as function of 243.1 nm detuning and quench detuning 114
5.6 Capture probability in dipole trap as a function of 243.1 nm power and quenching power. 114
5.7 Loss rate in dipole trap as a function of 243.1 nm power and quenching power. . . . 116
5.8 Capture/loss ratio in dipole trap as a function of 243.1 nm power and quenching power. 116
5.9 Capture rate in dipole trap as function of position in trapping region . . . 117
5.10 Capture rate in dipole trap as function of initial atomic velocity . . . 118
5.11 The proposed experimental setup for capturing hydrogen in a dipole trap using focusing of Helmholtz coils . . . 119
5.12 Helmholtz coils for slowing and focusing atoms into dipole trapping region . . . 119
5.13 Increased atomic flux through dipole trapping region through focusing of Helmholtz coils . . . 120

6.1 Planned 2S–8S/D Measurements . . . 124
6.2 Planned Two-Photon Laser Cooling Apparatus . . . 125

Chapter 1

Motivation

Spectroscopic measurements of hydrogen have inspired, confirmed, and ultimately improved our physical description of the universe. Owing to its simplicity and amenability to theoretical study, investigations on hydrogen have motivated the Bohr atomic model and quantum mechanics, validated the Dirac equation, and eventually revealed a flaw in Dirac's theory leading to the development of Quantum Electrodynamics (QED) [1]. This simplicity is seen by an expression of the energy levels in hydrogen, which can be written as

$$E_i = -\frac{R_\infty hc}{n_i^2}(1+\delta_i), \tag{1.1}$$

where R_∞ is the Rydberg constant, n_i is the principal quantum number of state i, and δ_i, where $|\delta_i| \ll 1$, contains details of the theory of the energy level [2].

Since the transition frequency between different energy levels is $h\nu_{ii'} = E_{i'} - E_i$, high precision spectroscopy of hydrogen can test Eq. 1.1. For example, these measurements can precisely determine the Rydberg constant, $R_\infty = \alpha^2 m_e c/2h$, which links several fundamental constants ($\alpha \rightarrow$ fine-structure constant, $m_e \rightarrow$ electron mass, $c \rightarrow$ speed of light, $h \rightarrow$ Planck's constant) and is useful for adjustment of these constants [3]. Besides this, δ_i is abundantly rich with information as it contains relativistic corrections predicted by Dirac and further relativistic corrections due to proton recoil, as well as nuclear polarizability and a multitude of QED corrections such as self-energy, vacuum polarization, and effect of the proton size [2]. Therefore, increasingly precise spectroscopic studies of hydrogen that probe Eq. 1.1 continue to test bound-state QED [3–5], provide knowledge of nuclear structure [6], and give a more precise determination of the Rydberg constant and proton radius [3, 7]. Furthermore, these studies may provide tests of the charge conjugation, parity, and time (CPT) reversal theorem by comparing certain hydrogen transitions

with the same measurements on anti-hydrogen that are now possible due to recent advancements in trapping hydrogen's anti-matter counterpart [8–12].

A common limitation to all these experiments is the non-zero atomic velocity of the hydrogen sample at finite temperature. This introduces Doppler shifts and transit-time broadening, inhibiting the precision with which hydrogen transitions can be measured. This is illustrated by measurements on the 1S-2S transition, a cornerstone of hydrogen spectroscopy due its naturally narrow linewidth of 1.3 Hz. Measured with an impressive fractional uncertainty of 4.2×10^{-15} [5], the recovered linewidth of 2 kHz is still three orders-of-magnitude larger than the natural linewidth due to transit-time broadening.

These unwanted velocity effects that impact the 1S-2S transition and other hydrogen transitions could be mitigated through laser cooling. Ubiquitous in experimental atomic, molecular, and optical (AMO) physics, laser cooling has spurred remarkable advances in high precision spectroscopy of heavier atoms [13, 14]. For example, laser cooled strontium has been trapped into an optical lattice clock with accuracy and stability at the 10^{-18} level [15]. While the potential benefits of laser cooling hydrogen have long been known, laser cooling of hydrogen has proven elusive. Instead, hydrogen spectroscopy has relied on other methods to reduce velocity effects such as two-photon spectroscopy, crossed-beam spectroscopy, and cryogenic atomic beams [3–5, 16, 17]. While commendable precision has been achieved with these techniques, rapid and robust laser cooling of hydrogen would be a much more preferable method. One can imagine the potentially revolutionary implications of laser cooled hydrogen. For example, a crowning achievement could be an optical lattice clock on the 1S–2S transition in hydrogen. The definition of time could therefore be directly related to fundamental constants instead of arbitrary transitions in heavier atomic species [18, 19]. For the purist, this would be a much more aesthetically pleasing definition of time and put us closer to having all our units defined in terms of fundamental constants.

Despite significant interest, laser cooling hydrogen has proven to be challenging. The most straightforward cooling cycle would use the single-photon 1S-2P transition shown in Fig 1.1(a). However, this single-photon cooling cycle requires Lyman-α radation at 121.6 nm. Unfortunately,

this wavelength is notoriously difficult to produce and work with. There are no lasers that directly emit this wavelength, and the next common method of frequency conversion through second harmonic generation in a nonlinear crystal does not work since transparent nonlinear crystals at this wavelength do not exist. Therefore, the general way in which Lyman-α is generated is through more complicated, less-efficient frequency conversion methods in gases [20, 21]. Once generated, Lyman-α must propagate in vacuum and the MgF_2 lenses used for collimation will transmit at best $50 - 60\%$ of the power. Due to these challenges, there has only been one demonstration of laser cooling hydrogen using Lyman-α radiation. The laser cooling took several minutes and was done on magnetically trapped spin-polarized hydrogen that was first cooled in a dilution refrigerator [22].

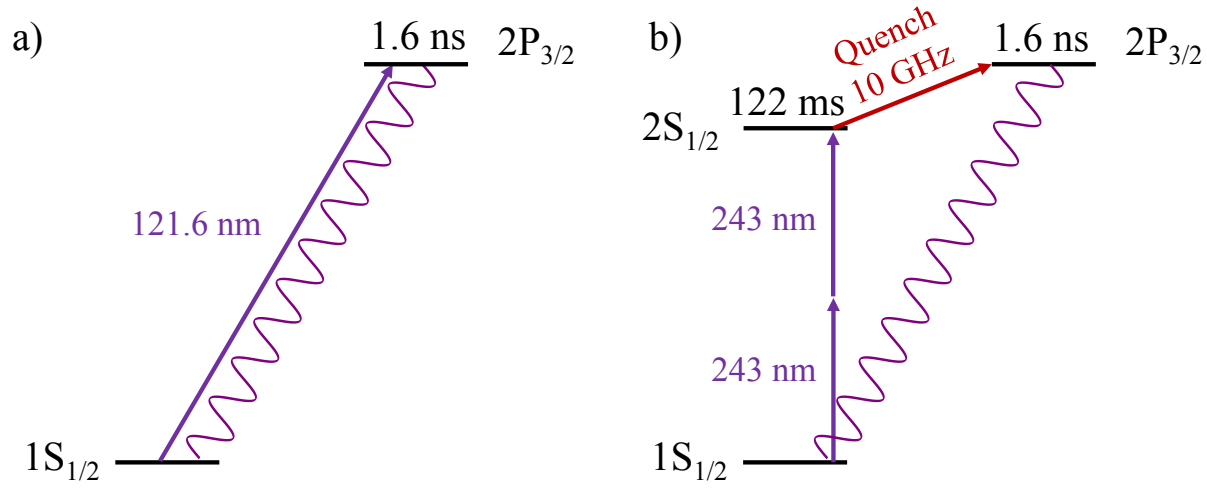

Figure 1.1: Single-photon versus two-photon cooling scheme for hydrogen. a) Single-photon scheme using Lyman-α light at 121.6 nm b) Two-photon scheme using 243.1 nm radiation and a quenching field from the metastable 2S state to the short-lived 2P state.

,

Due to the challenges posed by producing and working with Lyman-α radiation, there have been several proposals motivating two-photon cooling of hydrogen [23–26]. As seen in Fig. 1.1(b), this would require a two-photon excitation from the 1S–2S state using 243.1 nm radiation that is much easier to produce and work with than Lyman-α. However, there are two challenges with this

two-photon cooling scheme. Since the 2S state is metastable with a lifetime of $\tau_{2S} = 122$ ms, the 2S state must be quenched by mixing with the short lived 2P state ($\tau_{2P} = 1.6$ ns) to complete a cooling cycle. This could be accomplished with a 10 GHz microwave field or optical excitation to the 3P state [26]. A more significant challenge is the small absorption-cross section of this two-photon process since there is no near-resonant intermediate state between the 1S and 2S states [27]. As shown in Chapter 4, when maximally mixed with the 2P state and on resonance, the scattering rate between the 1S and 2S state is

$$\Gamma_{scat} = 6.8 \times 10^{-8} I^2 \mathrm{s}^{-1} \frac{\mathrm{cm}^4}{\mathrm{W}^2} \tag{1.2}$$

where I is the intensity of the 243.1 nm radiation. Due to the relatively large recoil velocity of hydrogen, $v_r = 3.3$ m/s, scattering rates of $\Gamma_{scat} = 1000$ s^{-1} could slow a 100 m/s atom to its recoil velocity in 30 ms over $\approx$ 1.5 m. This could be realized by overlapping the 243.1 nm radiation with the slow velocity tail of a cryogenic beam of hydrogen. However, even though the scattering rate is modest by typical laser cooling standards, due to the small probability of two-photon interactions, it would require 60 W of 243.1 nm power assuming a reasonable beam waist of 180 μm. Despite interest and development of 243.1 nm laser sources for exciting the 1S-2S transition over the last several decades [28–30], before the work presented in this dissertation, only 50-100 mW of 243.1 nm power could routinely be produced, which could be increased to $\approx$ 1 W through cavity enhancement [17].

Notwithstanding the progress made on these systems, these powers are still one to two orders-of-magnitude less than what is needed for rapid and robust two-photon cooling of hydrogen. Spurred by technological advances in high power fiber amplifier and nonlinear crystals, the primary motivation for the work presented in this dissertation is the development of a power scalable 243.1 nm laser system capable of two-photon cooling hydrogen.

As mentioned, a source of laser cooled hydrogen atoms in the ground state would prove invaluable for hydrogen spectroscopy and could enable an optical lattice hydrogen clock. Even without

laser cooling, a high power 243.1 nm laser system has significant utility for spectroscopy on hydrogen and hydrogen-like atoms. For example, a larger interaction volume for spectroscopy of the 1S–2S transition would be possible without sacrificing statistics. This would decrease transit-time broadening and increase the fraction of the atomic beam excited [5]. Increasing the interaction volume is also pertinent for 1S–2S spectroscopy of anti-hydrogen as it currently takes ≈ 300 s per data point due to the relatively large trap volume versus small interaction volume with the 243.1 nm radiation [10–12]. Similarly, with a slight tuning of the laser wavelength to 244 nm, such a laser can study muonium which is ideal for testing bound-state QED due to its lack of internal structure [31]. Measurements of muonium face low detection rates due to limited flux of muonium atoms and would benefit from increased 244 nm power [32]. Another relevant use of a high power 243.1 nm laser for hydrogen spectroscopy would be its contribution in addressing the discrepancy in the determination of the proton radius between spectroscopic comparisons of hydrogen and muonic hydrogen, known as the proton radius puzzle [1, 7, 33]. Due to their relatively narrow linewidth, the measurements on the 2S-8S/D transitions in hydrogen have significantly contributed to this discrepancy [34, 35]. These measurements used a thermal hydrogen beam at room temperature and the electron impact method used to populate the 2S state was only $\sim 10^{-6}$ efficient and further heated the beam [34, 36]. A high power 243.1 nm source could populate the 2S with unit efficiency. In tandem with a 6 K cryogenic atomic beam source this would drastically increase the statistics. This would reduce the necessary laser power needed to address the 2S-8S/D transitions which in turn would decrease the AC Stark shifts that were leading systematics in the past measurements.

Outside of the metrology of simple atomic systems, there is also utility for coherent, high-power deep-UV lasers at 243–244 nm. In Raman spectroscopy, the signal intensity follows a λ^{-4} dependence, motivating the use of UV lasers. Due to the relatively small cross sections of Raman processes, high-power UV sources could help in detection of trace gases, which would assist in identification of explosive materials [37]. While high-power 266 nm lasers are available [38], a 243–244 nm laser is preferable in some cases since the flourescence background in Raman

spectroscopy diminishes rapidly below 250 nm [39]. The 243–244 nm wavelength range also matches the semiconductor industry's standard KrF photoresists. Therefore, these laser systems could offer an alternative to the argon-ion lasers often used in laser interference lithography [40]. This technique can produce nanoscale, periodic patterns over large areas on substrates which can be used in a diverse set of versatile technologies such as 2D photonic crystal slabs, plasmonic color filters, optical data storage, and nanophotonic devices [40, 41].

1.1 Thesis Outline

Motivated by improving spectroscopy of simple and exotic atoms, the general utility of a high-power deep-UV laser, and primarily, the ability to robustly two-photon cool hydrogen, we developed a novel, high-power, coherent 243.1 nm continuous wavelength (CW) laser based on frequency quadrupling a Yb-fiber amplifier system at 972.5 nm (see Fig. 1.2), and demonstrated that this laser system can be cavity enhanced to powers practical for two-photon laser cooling. Through simulations, we explored this laser's ability to capture hydrogen in an optical trap, and show that an optical lattice hydrogen clock could be realizable with this laser system.

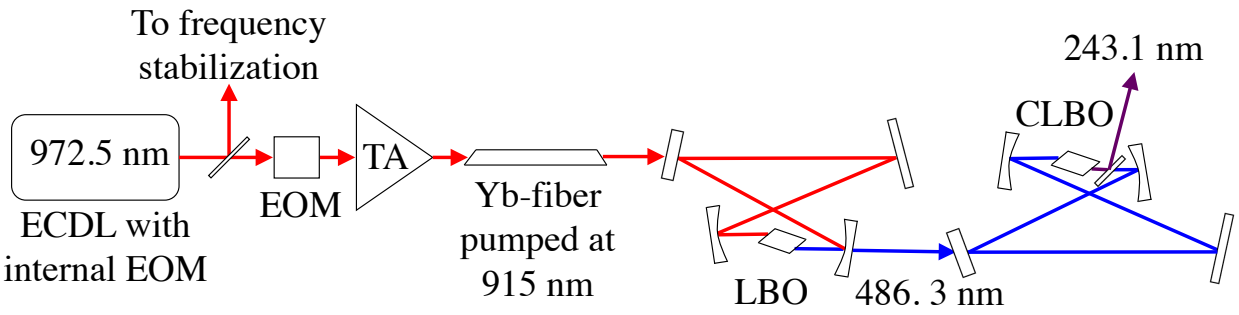

Figure 1.2: Simplified design of the Yb-fiber amplifier and resonant doubling stages. The master oscillator at 972.5 nm is an extended cavity diode laser (ECDL). A small portion of the 972.5 light is used to actively stabilize the frequency of this oscillator. This 972.5 nm light is then amplified through a tapered amplifier (TA) and Yb-doped amplifier, followed by frequency quadrupling through successive resonant doubling stages.

Chapter 2 contains a description of our high-power, narrow linewidth Yb-fiber amplifier system. As seen in Fig. 1.2, the system begins with a master oscillator power amplifier at 972.5 nm

that is then amplified within a Yb-doped fiber amplifier. Using this system, we are able to generate > 10 W of power at 972.5 nm with an estimated linewidth of < 1 kHz. Following this, Chapter 3 describes the frequency conversion of our Yb-fiber amplifier system through the successive intracavity doubling stages that follow the Yb-fiber amplifier in Fig. 1.2. These stages are able to generate > 4 W of power at 486.3 nm and > 1 W of power at 243.1 nm. Chapter 4 describes cavity enhancement of the high-power 243.1 nm output from this laser system. We demonstrate intracavity 243.1 nm powers > 30 W, which are approaching those required for robust and realizable two-photon cooling of hydrogen. Chapter 5 explores through simulations how a single two-photon cooling cycle from this 243.1 nm laser system can capture hydrogen atoms in a magic wavelength optical trap, and how this could translate to capture into an optical lattice. Chapter 6 summarizes the results and presents future planned studies built upon them.

Chapter 2

Yb-Fiber Amplifier at 972.5 nm

2.1 Introduction

The common method for generating highly coherent 243.1 nm radiation to excite the hydrogen 1S–2S transition is through a frequency-quadrupled solid-state master oscillator power amplifier (MOPA) system at 972.5 nm. MOPAs at 972.5 nm typically consist of a low power master oscillator followed by a semiconductor optical amplifier called a tapered amplifier (TA) [12, 29, 30, 42]. Limited by the TA's maximum performance, MOPAs at 972.5 nm can generate 2.5–3 W of power at this wavelength, which upon frequency quadrupling, results in 50-150 mW of radiation at 243.1 nm, depending on the efficiency of the quadrupling systems.

As seen in Fig. 2.1, second harmonic power generated behaves quadratically at low fundamental input powers when using intracavity doubling. This suggests that a factor of two to three times more power at 972.5 nm could lead to one to two orders-of-magnitude more power at 243.1 nm. This is seen in Fig. 2.1. We see that with 2.5 W of power at 972.5 nm—standard outputs for available 972.5 nm MOPA systems—frequency quadrupling results in $\approx$ 50 mW of 243.1 nm power. However, with 10 W of 972.5 nm radiation, just a factor of four more power, $\approx$ 2 W of 243.1 nm radiation is available, which is 40 times more power. Since two-photon scattering processes are quadratic with intensity, this would increase 1S–2S excitation rates by 1600!

While this factor of four increase in fundamental IR power may seem a modest task, generating further gain at 972.5 nm is technically challenging as there are no gain mediums that preferentially operate at this wavelength. However, there are gain mediums that operate close to this wavelength, such as Yb-doped fibers. The absorption and emission cross-section data for a Yb-doped fiber is shown in Fig. 2.2. As seen, gain is much more readily obtained in Yb systems above 1 μm due to the low absorption cross section in this spectral region. Gain at the emission cross-sectional peak near 975 nm is also possible but requires population inversions near 50% because the ab-

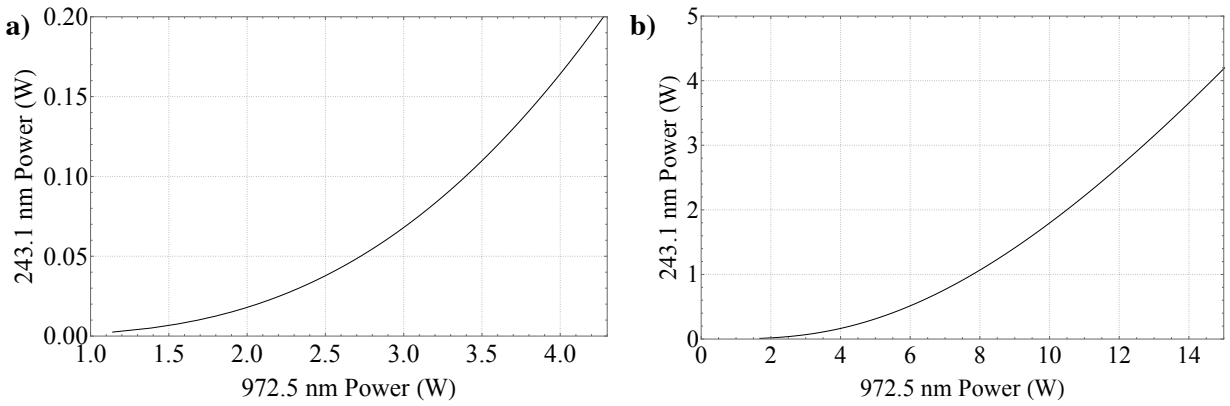

Figure 2.1: Small increases in 972.5 nm power result in large gains at 243.1 nm. Following a model for intracavity frequency doubling (described in Chapter 3), second harmonic power increases quadratically at low fundamental input power. This means that small gains at the fundamental IR power of 972.5 nm lead to drastic increases in the frequency-quadrupled UV power. a) Expected 243.1 nm output using available 972.5 nm MOPA systems. b) Expected 243.1 nm output with higher power 972.5 nm input radiation.

,

sorption cross section in that spectral region has approximately the same magnitude. Despite this difficulty, there have been demonstrations of 100 W Yb-doped fiber lasers near the emission cross-sectional peak at 975 nm [43, 44]; however, these sources were not coherent enough for frequency conversion, let alone cooling or spectroscopy.

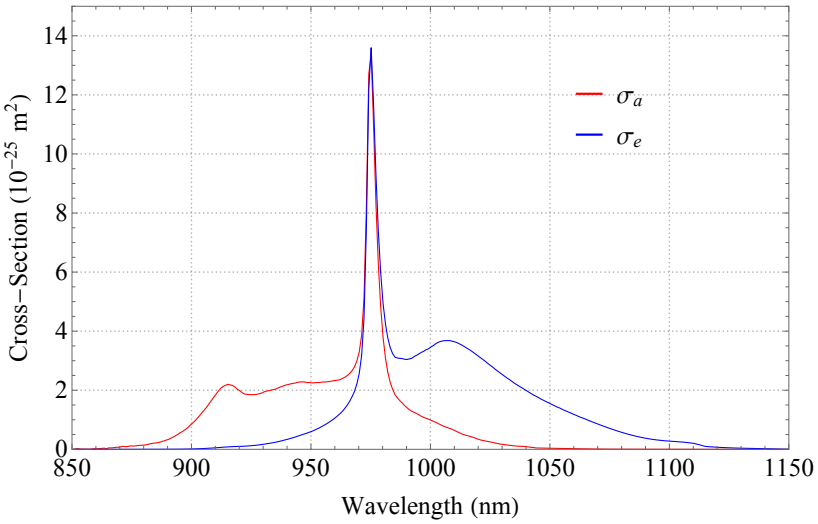

Figure 2.2: The absorption and emission cross-section versus wavelength for Yb^{3+} in a phosphosilicate host. There are three peaks of interest: 1) Absorption peak at 915 nm 2) Absorption and emission peak at 975 nm 3) Emission peak at 1010 nm. Note, the cross-section data for Yb^{3+} depends on the host material. This commercially available fiber data was provided to us by the manufacturer (CorActive DCF-YB-20/128P-FAC).

When the work presented in this thesis began, the highest power, narrow linewidth Yb-fiber laser systems at this cross-sectional peak were a few hundred mW [45], and just recently reached 10 W following a similar design to the system developed for this thesis [46]. However, all these lasers operated at or above the emission cross-sectional peak. Below this peak, the emission cross-section drops rapidly, and generating gain becomes even more challenging. To the best of our knowledge, there are limited studies of Yb-fiber laser systems being pushed to wavelengths below 975 nm [47], and these studies were only at low power ($\approx$ 10 mW).

In this chapter, a highly coherent, high power Yb-fiber laser system operating below this emission cross-section peak is presented. With its current design, the system is capable of generating 10 W of power at 972.5 nm stably over several hours. The system also possesses a narrow linewidth of $<$ 1 kHz, and can be frequency referenced to a frequency comb.

This chapter will start by briefly reviewing the history of fiber lasers leading to the birth and success of Yb-fiber lasers. Then, the difficulties of making Yb-fiber lasers at and below the cross-sectional peak will be presented. This will focus on two main challenges, photodarkening and gain competition. An explanation of each challenge and the techniques that have been developed to overcome them will be presented. The chapter will then present the design, development, and performance of our high power, single-frequency Yb-fiber amplifier laser system.

2.2 Brief History of Fiber Lasers

The first proposal and demonstration of an optical maser (i.e., laser), utilized a gain medium enclosed within a Fabry-Perot cavity [48, 49]. While confining the medium within a waveguide offers increased mode selection and stronger mode coupling compared to a Fabry-Perot, the traditional metallic waveguides utilized for masers were not viable in the optical regime. In 1961, one year after Maiman's ruby optical maser demonstration, Snitzer proposed that an optical fiber could serve as a dielectric waveguide to provide a resonant structure for optical masers [50], and took the first steps towards this goal by demonstrating optical maser action of Neodymum(Nd)$^{+3}$ in a "quasi-fiber," which consisted of a barium glass rod [51]. During this burgeoning era of optical

maser development, understanding the complicated spectra of rare-earth ions attracted significant renewed interest owing to their numerous optical and infrared transitions [52–54]. By 1963, optical maser effects had been observed in nine of the seventeen rare-earths in either divalent or trivalent form [55], including Yb^{+3} [56]. One year later, the first true rare-earth fiber laser was demonstrated using a one-meter long, helically wound Nd^{3+} fiber that was flash-pumped and seeded with a Nd^{3+} glass rod laser [57].

After this initial demonstration, the next 20 years focused on developing more robust Nd fiber laser technology, highlighted by three main advances. These were end-pumped fiber lasers [58,59] fabricating single mode fiber lasers [60], and developing low loss, uniform doping techniques with rare-earth ions [61, 62]. These advances made fiber lasers more accessible, and scientists quickly investigated other rare-earth fiber lasers. This led to the first Erbium(Er)-doped fiber lasers in the late 1980's [63, 64]. This development was critical for long range optical fiber communications as Er fibers can amplify light at 1.5μm, the lowest loss region for the silica-based telecommunication fibers [65]. Although beyond the scope of this dissertation, it should be noted the enormous impact Er fiber amplifiers have had on our modern world as they led to the development of the internet among other things.

2.2.1 Birth of the Yb-Fiber Laser

From a fundamental laser development perspective, the ability to amplify radiation within a single-mode fiber encouraged studies of other rare-earth fiber lasers besides Nd and Er, such as holium, praesodymium, and thulium [66], and in 1988, the first Yb^{3+} fiber laser was demonstrated [67]. Over the next several years, numerous results showed the versatility of Yb-fiber lasers. As demonstrated by [68, 69], and seen in Fig. 2.2, Yb-fiber lasers could emit and absorb over a $\approx$250 nm bandwidth, as well as operate with high-efficiency and high-power [70, 71].

The culmination of these results was the recognization of Yb-doped fiber lasers as future leaders in the field of high-power rare-earth fiber lasers [72, 73]. The energy structure of Yb ions in silica, seen in Fig. 2.3, boasts a small quantum defect, which reduces thermal stress, and is simple

for a rare-earth ion, with only two Stark manifolds. This simple energy structure prevents excited state absorption, allows high doping, and helps mitigate certain quenching affects [73]—all advantageous properties for building a high-power fiber laser.

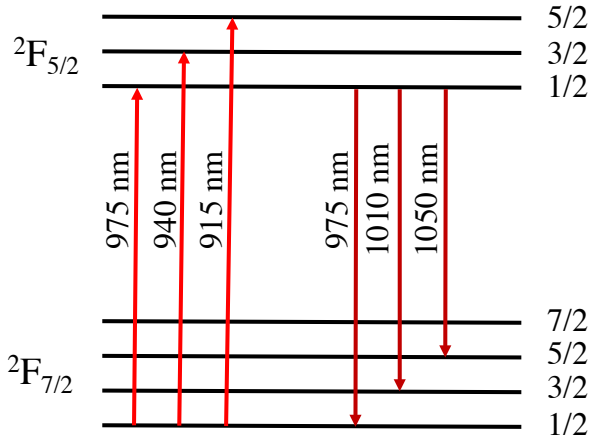

Figure 2.3: The energy structure of Yb^{3+} ions hosted in the lattice of an optical fiber consists only of a ground and excited state manifold [72]. Each manifold is split into Stark levels due to the electric field of the host lattice. The energy separation between different levels is given in nm with common pump wavelengths represented by upward arrows and lasing by downward arrows. As can be seen, lasing at 975 nm resembles a 3-level system, whereas lasing at longer wavelengths can be more appropriately described as quasi-3-level or quasi-4-level systems depending on the choice of pump wavelength. Note: The energy separation between these levels varies based on the host material. The values here represent the phosphosilicate host of our Yb-fiber.

The potential of high-power Yb-fiber lasers was demonstrated through the use of two complementary technologies that were concurrently being developed, high-power laser diode arrays [74] and double-clad fibers [75, 76]. As seen in Fig. 2.4, a double-clad fiber consists of a doped single-mode core surrounded by a much larger inner cladding, which is confined by an outer cladding. The large area of the inner cladding enables propagation of high-power multi-mode beams, which could be absorbed within the single-mode core. This enabled pumping of Yb-fibers with the newly developed high-power laser diode arrays. Numerous studies of high power multi-mode pump absorption [77–81] showed that pump absorption can be increased by breaking the symmetry of the inner-cladding. This increases mixing of the higher order modes contained in the multi-mode pump beam with the core. Therefore, double-clad Yb fibers with the proper geometries can be efficiently

pumped with high power multi-mode sources without sacrificing the single-mode quality of the lasing wavelength output. The first Yb-doped double-clad fiber was demonstrated in 1994, with an output of ≈0.5 W at 1042 nm [82]. By 1999, continuous-wavelength (CW) Yb-fiber laser power had reached 100 W [83], by 2004, 1 kW [84], and by 2009, 10 kW [85]. Similarily, femtosecond pulsed Yb-fiber lasers reached 100 W by 2005 [86] and up to 1 kW by 2009 [87]. These are just a few examples of the highlights in high power Yb-fiber laser development, and a more complete overview can be found in the following review articles [88–90].

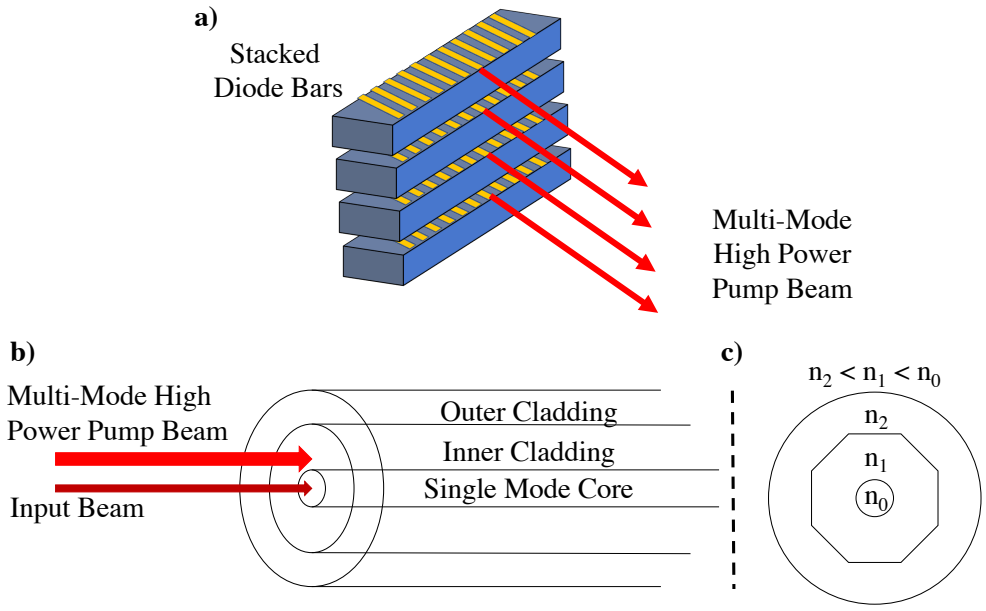

Figure 2.4: Key technologies for high-power fiber lasers: High-power laser diode arrays and double-clad fibers. a) Arrays of single emitters constitute a laser diode array. The light from all the emitters can be focused and combined with optical elements, creating a high-power multi-mode output. For increased power, the arrays can be stacked. b) Double-clad fiber geometries enable high-power multi-mode pumping. A doped single-mode core is surrounded by a much larger inner cladding, which is confined by an outer cladding. c) A common asymmetry to increase pump absorption in the core is through use of an octagonal inner cladding.

These are impressive results. However, these systems, along with the majority of Yb-fiber systems operate above 1 μm. As seen in Figs. 2.2 and 2.3, $\sigma_e >> \sigma_a$ in this spectral region and Yb-fiber lasers behave as a quasi-4-level system. This makes gain in this spectral region extremely favorable. Exciting hydrogen with a frequency-quadrupled Yb-fiber laser requires a

high-power, single-frequency Yb-fiber operating near 975 nm. At the beginning of this work, a Yb-laser satisfying these these requirements did not exist and the following section explains the difficulties that were overcome to accomplish this.

2.3 Gain near the Absorption & Emission Cross Section Peak

For a homogeneously broadened Yb-doped fiber of length L, the gain in dB can be written as

$$G(\lambda) = 10 \log_{10} \exp\Big[\int_0^L g(z)dz\Big] \text{dB} \tag{2.1}$$

$$= k \int_0^L g(z)dz, \tag{2.2}$$

where k = 4.343 dB and

$$g(z) = N_2(z)\sigma_e^\lambda - N_1(z)\sigma_a^\lambda, \tag{2.3}$$

where N_1 and N_2 correspond to the population in the ground and excited state manifolds (see Fig. 2.3), and σ_e^λ and σ_a^λ are the emission and absorption cross-section values at the laser wavelength, λ. Since $N_1(z) = N - N_2(z)$, where N is the total concentration of active Yb-ions, Eq. 2.2 can be rewritten as

$$G(\lambda) = k\big[\sigma_a^\lambda + \sigma_e^\lambda\big] \int_0^L N_2(z)dz - kNL\sigma_a^\lambda \tag{2.4}$$

Averaging the excited state population across the length of the fiber gives $\bar{N_2} = 1/L \int_0^L N_2(z)dz$. With this average, we can rewrite this form as

$$G(\lambda) = kNL\big[(\sigma_a^\lambda + \sigma_e^\lambda)n_2 - \sigma_a^\lambda\big], \tag{2.5}$$

where $n_2 = \bar{N}_2/N$ is the fraction of excited ions. From Eq. 2.5, we can see the difficulty with achieving gain near the absorption-cross section peak. The population inversion required just to reach transparency, n_{2t}, is found by setting $G(\lambda) = 0$. Using the cross-section values from Fig. 2.2, we see the inversion required for transparency for operation at 1010 nm vs 975 nm is

$$n_{2t,1010} = \frac{\sigma_a^{1010}}{\sigma_a^{1010} + \sigma_e^{1010}} = 0.15 \tag{2.6a}$$

$$n_{2t,975} = \frac{\sigma_a^{975}}{\sigma_a^{975} + \sigma_e^{975}} = 0.5 \tag{2.6b}$$

Since $n_2 \propto I_{pump}$ (see, for example [72]), the higher inversion required for gain at 975 nm requires significantly larger intensities that can optically damage Yb-fibers. Furthermore, since the pump intensity and inversion needed for gain at 1010 nm is significantly lower than 975 nm, the large inversions needed for gain at 975 nm will produce large gain at 1010 nm. A discussion of preventing damage in Yb-fibers at these high inversions and an understanding of the subsequent gain competition between these two wavelengths is therefore necessary.

2.3.1 Photodarkening

The high inversions required for gain at 975 nm lead to an unwanted effect that limits the efficiency and lifetime of Yb-fiber lasers. This effect is called photodarkening and, as the name suggests, is an optically induced process in Yb fibers that results in loss. This loss comes from structural changes, often referred to as impurities or color centers, that exhibit broadband absorption over the visible to near-IR range. As photodarkening increases with increased inversion, understanding this process has attracted significant interest from the high-power Yb-fiber community [91, 92].

This effect was first observed in Yb fibers in 1997, and labeled as lifetime quenching. It was an unexpected occurrence as the simple two-level structure of Yb fibers should preclude typical quenching mechanisms such as multi-phonon decay and concentration quenching. While the mechanism was not fully understood, the authors attributed the unwanted absorption to some impurity or structural defect in the fiber [93].

The physical mechanism behind the creation of these absorbing color centers has remained actively under debate since this initial observation. The two main competing theories attribute photodarkening to a Charge Transfer (CT) process or Oxygen Deficiency Centers (ODCs) in the fiber. In the first case, a high-energy process can excite a Yb^{3+} ion to a CT band, upon which an electron is transferred from the surrounding fiber lattice to the Yb^{3+}, forming Yb^{2+}. This creates free holes in the fiber lattice that can form color centers [94,95]. In the second case, ODCs can exist in a Yb-fiber, which upon excitation through a high-energy process can release a free electron that can form a color center [96], as well as create a variety of undesirable energy transfer mechanisms between ODCs and Yb^{3+} [97, 98].

It is experimentally difficult to distinguish between these two effects as both excitation to the CT band and exctitation of an ODC occur over a broad, highly overlapped UV range. Furthermore, strong evidence supporting both mechanisms exists. Loading a Yb-fiber with oxygen or doping the silica with aluminum reduces the amount of ODCs in a Yb-fiber, and both have been shown to reduce photodarkening [96]. However, hydrogen loading a Yb-fiber as well as co-doping the fiber with phosphorous and cerium have all shown to reduce photodarkening, and can be explained via the CT argument [95,99,100]. Furthermore, an increase of Yb^{2+} have been found in photodarkened Yb-fibers, supporting the CT mechanism [101].

Despite the uncertainty in the exact mechanism behind photodarkening, the attempts to prevent photodarkening have been very successful. Co-doping the silica glass has produced highly efficient, 100 W powers with almost no loss from photodarkening [102], and commercially available Yb-fibers co-doped with phosphorous are available and marketed as photodarkening free at high powers.

2.3.2 Gain Competition at 975 nm Operation

Besides the problems from photodarkening, the high inversions required for gain at 975 nm lead to gain competition at 1010 nm. These high inversions require signficant pump intensities, which can be achieved through double-clad fibers as high-power multi-mode pump lasers can be coupled into the inner cladding. The gain equation in Eq. 2.5 can be adjusted to account for modes that propagate in this inner cladding through the following modification [73]

$$G(\lambda) = kNA_{core}L\Psi_d^\lambda\big[(\sigma_a^\lambda + \sigma_e^\lambda)n_2 - \sigma_a^\lambda], \tag{2.7}$$

where A_{core} is the area of the doped core and Ψ_d^λ is the normalized modal intensity (in m^{-2}) averaged over A_{core}. For modes propagating purely in the core, $A_{core}\Psi_d^\lambda = A_{core}/A_{core} = 1$; however, for modes propagating in the inner cladding, $A_{core}\Psi_d^\lambda = A_{core}/A_{clad} = \beta^{-1}$. As suggested in [73], we can manipulate Eq. 2.7 to understand the gain at one wavelength based on the gain at two other wavelengths. Using superscripts to differentiate between three different wavelengths, λ^A, λ^B and λ^C, we get three equations:

$$G^A = D\Psi_d^A[(\sigma_e^A + \sigma_a^A)n_2 - \sigma_a^A] \tag{2.8a}$$

$$G^B = D\Psi_d^B[(\sigma_e^B + \sigma_a^B)n_2 - \sigma_a^B] \tag{2.8b}$$

$$G^C = D\Psi_d^C[(\sigma_e^C + \sigma_a^C)n_2 - \sigma_a^C], \tag{2.8c}$$

where $D = kNA_{core}L$. Using Eqs. 2.8b and 2.8c, D and n_2 can be eliminated in Eq. 2.8a, relating the gain at three different wavelengths purely based on their cross-sections and mode size

$$G^A = G^B \frac{\Psi_d^A(\sigma_e^A/\sigma_e^C - \sigma_a^A/\sigma_a^C)}{\Psi_d^B(\sigma_e^B/\sigma_e^C - \sigma_a^B/\sigma_a^C)} + G^C \frac{\Psi_d^A(\sigma_e^A/\sigma_e^B - \sigma_a^A/\sigma_a^B)}{\Psi_d^C(\sigma_e^C/\sigma_e^B - \sigma_a^C/\sigma_a^B)} \tag{2.9a}$$

$$= G^B \frac{\Psi_d^A}{\Psi_d^B} A_1 + G^C \frac{\Psi_d^A}{\Psi_d^C} A_2, \tag{2.9b}$$

where A_1 and A_2 are the cross-section ratios. In our case, we are interested in creating gain near the absorption/emission peak of 975 nm, while pumping at 915 nm, and beating unwanted gain at 1010 nm. Applying this specific case to Eq. 2.9a, we see that $\lambda_A = 1010$ nm, $\lambda_B = 975$ nm, and $\lambda_C = 915$ nm. Using the data from Fig. 2.2, the cross-section ratios A_1 and A_2 in Eq. 2.9b can be calculated. Furthermore, since gain at 975 nm and Amplified Spontaneous Emission (ASE) only occur in the doped core, $\Psi_d^A/\Psi_d^B = 1$, as they share the same pump modal intensity. Whereas, $\Psi_d^A/\Psi_d^C = A_{clad}/A_{core} = \beta$. With these simplifications, Eq. 2.9b takes the form

$$G_{1010} = 0.276\, G_{975} + 1.39\, \beta\alpha, \tag{2.10}$$

where α is the pump absorption in dB. From Eq. 2.10, we see that minimizing β and α reduces the gain at 1010 nm. However, for double-clad fibers, $\beta = A_{clad}/A_{core} > 1$, and for commercially available double-clad Yb-doped fibers, β is normally between 40-400. As a reference, for $\beta = 40$, just 1 dB of pump absorption would result in a tremendous gain of 55 dB at 1010 nm.

In order to make pure Yb-fiber lasers at 975 nm, laser scientists have developed numerous techniques to compete with this enormous gain above 1 μm. One method is to decrease β by making the core larger. Using rod-type photonic crystal fibers, β, and thus unwanted gain above 1 μm, can be reduced by nearly an order of magnitude. This has enabled output powers of 27 W, 94 W, and 94 W at 976 nm, 977 nm, and 980 nm, respectively in rod-type photonic crystal fibers [43, 44, 103]. This technique has produced the highest power Yb-fiber lasers at 975 nm, nearly two orders of magnitude larger than other Yb-fiber lasers (described next) at this wavelength. However, the spectral output of these systems had several nm bandwidths, which is too large for frequency doubling and spectroscopy.

Instead of increasing the core size, another approach to reducing β is decreasing the inner cladding area. The challenge here is keeping the inner cladding's numerical aperture (NA) large enough such that multi-mode pump power can still be coupled into the inner cladding. This is possible with jacketed air-cladding. More than 1.4 W of 980 nm has been achieved using this technique [104]. Another creative way to manipulate β is via ring-doping, which increases the area over which the lasing radiation can interact with pump radiation without affecting the area over which the pump radiation interacts, effectively reducing β [73]. However, neither of these techniques have demonstrated single-frequency operation or the power of the rod-type systems.

The above techniques all imposed spectral gain discrimination by geometrically altering the gain medium to increase its interaction with the pump as less pump interaction favors lasing at the 4-level 1010 nm region. More obvious spectral gain discrimination is through the use of spectral filters and short fiber lengths. This has been accomplished using dielectric mirror coatings [105], as well as distributed Bragg reflectors [45, 106, 107], reaching powers of 1 W, 45 mW, 100 mW, and 230 mW at 978 nm, 977 nm, 976 nm and 978 nm, respectively. A more creative solution to spectral filtering is through the use of photonic bandgap fibers that only allow certain wavelengths to propagate in the core. Using this technique, 130 mW at 977 nm was generated [108]. While all these powers are low (1 W or less) the work in [45, 107] demonstrated Yb-fiber sources in this wavelength region with single-frequency linewidths of < 10 kHz.

2.3.3 Gain Competition at 972.5 nm Operation

Evidenced by the numerous creative ways to combat gain near 1010 nm, achieving gain near 975 nm in a Yb-fiber laser has received significant attention. For hydrogen, the 1S-2S transition is excitable through a two-photon process with 243.1 nm radiation, which requires frequency quadrupled 972.5 nm light. As seen in Fig. 2.2, this wavelength is approximately half way down the absorption/emission cross-section peak at 975 nm. Therefore a laser at 972.5 nm will face the same 1010 nm gain competition as 975 nm, and additionally compete with gain at 975 nm. Fol-

lowing the same method used to generate Eq. 2.10, we see that the gain at these two competing wavelengths are

$$G_{1030} = 0.85\, G_{972.5} + 1.7\, \beta\alpha, \tag{2.11a}$$

$$G_{975} = 3.08\, G_{972.5} + 1.1\, \beta\alpha, \tag{2.11b}$$

which for $\beta = 40$ results in 68 dB of gain at 1030 nm and 44 dB of gain at 975 nm for every dB of pump absorption. As before, the unwanted gain competition is enormous, but now occurs at two wavelengths. With coherent 975 nm lasers only showing modest power [45, 107], it therefore seems unlikely a coherent 972.5 nm laser could be made with high power. While a pure, high-power, coherent Yb-fiber laser at 972.5 nm may be improbable, a Yb-fiber amplifier at 972.5 nm is different.

The 975 nm systems described above generated respectable powers at 975 nm by making the initial ASE at 975 nm dominate the gain competition. However, as mentioned in the introduction of this chapter, with current tapered amplifier technology, MOPAs can create up to 2-3 W of frequency stabilized power at 972.5 nm. This non-trivial amount of power at 972.5 nm can be used to seed a Yb-fiber amplifier. Pairing this with the techniques utilized above to compete with unwanted gain, e.g., short fiber lengths, spectral filtering, and decreasing β, gain at 972.5 nm is viable in a Yb-fiber amplifier.

2.4 Yb-Fiber Amplifier at 972.5 nm

2.4.1 Preventing Photodarkening and Parasitic Gain in our Design

The issues presented by photodarkening and parasitic gain at 975 nm and 1010 nm helped guide our design of a high-power Yb-fiber amplifier at 972.5 nm. We needed a Yb-fiber resistant to photodarkening at high power with a relatively large core/cladding ratio as, seen in Eqs. 2.11a and 2.11b, this reduces β and thus parastic gain. Fortunately, a Yb fiber co-doped with phosphorous

that demonstrated photodarkening free performance at high power existed commercially (CorActive DCF-YB-20/128P-FAC). Furthermore, while not a rod type photonic crystal fiber, in terms of commercially available Yb double-clad fiber, this fiber has a relatively small value of β due its large core/cladding ratio with a 20 μm core and 128μm cladding ($\beta \approx 41$). Besides decreasing β, we see from Eqs. 2.11a and 2.11b that reducing the pump absorption α also reduces gain at these parasitic wavelengths. This can be done by keeping the fiber length relatively short. In our design, we use ≈ 10 cm which makes $\alpha \approx 0.5$ dB since our fiber has a 5.5 dB/m pump absorption in the cladding. Still, this gives $\approx$ 36 dB and 26 dB of gain at 1010 nm and 975 nm, respectively, for every dB of gain at 972.5 nm. Therefore, it is advantageous to keep the gain at 972.5 nm small, which is possible using a large amount of seed power at 972.5 nm. Using the $\approx$ 2.5 W of 972.5 nm power available from MOPAs, a factor of four increase in power gives 10 W of power. As shown in Fig. 2.1, this leads to dramatic gains in UV power at 243.1 nm. This factor of four increase corresponds to 6 dB of gain at 972.5 nm, meaning the gain at 1030 nm and 975 nm would be $\approx$ 40 and 41 dB, respectively. These are still very large, and to combat them we utilize a common technique used in Yb-fibers. We angle polish the ends to prevent the fiber lasing at these wavelengths. Lastly, these large gains make it imperative that we do not seed the Yb-fiber amplifier with radiation at these wavelengths. As MOPAs use tapered amplifiers that contain a broad spectrum of ASE underneath the amplified 972.5 nm light, we aggressively filter these unwanted wavelengths amplified by the TA using $OD_{abs} > 5$ spectral filters centered at 972.5 nm with $\approx$ 4 nm FWHM bandwidth.

2.4.2 Seed Laser Design

The design of our Yb-fiber amplifier system is shown in Fig. 2.5. It begins with the Master Oscillator Power Amplifier (MOPA). We use an extended cavity diode laser (ECDL) as our master oscillator. The ECDL is in Littrow configuration and consists of a single mode laser diode (QPHOTONICS:QLD-980-300S) collimated with an aspheric lens and 1200/mm diffraction grating. The first diffracted order provides optical feedback to the laser diode, and rotating the grating tunes the wavelength. The tuning ranged needed to study exotic simple systems is 972-976 nm, as

this results in 243-244 nm radiation upon frequency quadrupling. The diode can output from 970-990 nm, and the grating has no problem tuning over this 972-976 nm window. Within the ECDL is an electro-optic modulator for fast frequency control, and for slow stabilization the diffraction grating rests upon a piezo-controlled translation stage. For increased environmental isolation, the entire system is contained on its own breadboard, surrounded by thick aluminum walls, and an Anti-Reflective(AR) coated window is used to output the 972-976 nm radiation. The diode's temperature is controlled by a peltier device upon which the diode is mounted, with feedback provided by a Thorlabs laser diode temperature controller (TEC200C). The current of the diode is controlled by a thorlabs laser diode driver (LDC205C) and Table 2.1 shows the output power of the ECDL as a function of current.

Table 2.1: ECDL Output Power

Current (mA)	Power (mW)
50	9.4
75	18.2
100	26.8
125	35.5
150	44.3

As seen in Fig. 2.5, the output of the ECDL then goes through optical isolators before it is amplified by the tapered amplifier (TA). The isolators are necessary as the TA emits significant ASE in the reverse direction, which can destabilize the master oscillator. The original system only had one optical isolator separating the TA and ECDL, and we believe we saw instabilities that went away with addition of a second isolator. The TA needs 20-30 mW of seed power, and since each isolator has $\approx 7\%$ loss, the ECDL current is generally run between 100-125 mA.

As seen in Fig. 2.5, the master oscillator radiation is then amplified within a commercial tapered amplifier (DILAS TA-0976-3000). The TA chip is in a F-mount configuration. This commercial mounting options places the TA chip first on a gold-coated copper block inset, which is then housed within a larger frame. This mounting option provides increased heat dissipation, sta-

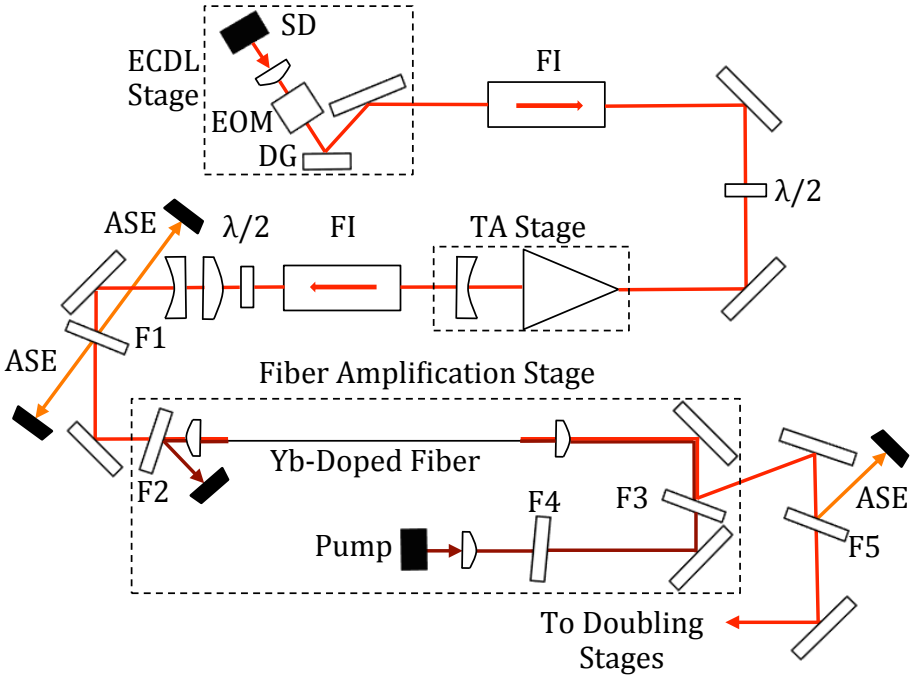

Figure 2.5: Schematic of the ECDL Master Oscillator and Amplification Stages. SD: Seed Diode, DG: Diffraction Grating, FI: Faraday Isolator, F1 and F5: Bandpass Filters, F2: Longpass Filter, F3 and F4: Shortpass Filters. The ECDL contains an electro-optic modulator (EOM) for fast frequency control.

bility, and protection of the TA chip. The F-mount is then secured on a water cooled aluminum block for temperature stabilization. Also mounted onto the block are aspheric lenses for coupling the seed radiation into the TA, as well as collimating the amplified output. The current is controlled by a Wavelengths electronic current driver and the output directly after the TA is shown in Table 2.2. While we have run the current up to 8 A, generating > 5 W of amplified power from our MOPA, the beam quality and stability of the TA output degrades past 5 A of current, which is the manufacturer recommended maximum current.

The output of the TA following following the aspheric lens is still highly astigmatic in one direction due to the tapered geometry of the output. We compensate for this with a cylindrical lens. As seen in Fig. 2.5, after the cylindrical lens, the MOPA beam is collimated, and its size reduced with a beam reducer in order to efficiently couple this light to the Yb fiber. However, before the MOPA radiation is amplified within the Yb fiber, it passes through an optical isolator to prevent optical feedback into the TA from back-reflections or ASE emitted from the fiber. The

Table 2.2: TA Output Power

Current (A)	Power after TA (W)	Power at Yb-fiber (W)
1	0.10	0.07
1.5	0.46	0.32
2.0	0.87	0.65
2.5	1.31	1.01
3.0	1.75	1.38
3.5	2.24	1.74
4.0	2.66	2.05
4.5	3.15	2.42
5.0	3.50	2.75

TA contains a broad spectrum of ASE underneath the amplified radiation. Due to the large gain at parasitic wavelengths, it is critical we filter this before amplification in the Yb fiber. Therefore the MOPA radiation is also passed through an $OD_{abs} > 5$ spectral filter (F1) centered at 972.5 nm with $\approx$ 4 nm FWHM bandwidth before amplification within the Yb-fiber. After all these components, the MOPA power is reduced from the output directly after the TA, and Table 2.2 has the measured input power before amplification within the Yb-fiber. At max settings, we have measured $\approx$ 2.5 W of 972.5 nm radiation within a TEM_{00} mode before amplification within the Yb fiber. This measurement is an estimate based on the power remaining in the MOPA beam in the far-field.

2.4.3 Yb-fiber Amplifier Design

As seen in Fig. 2.5, the output from the TA is then further amplified within the double-clad Yb-doped fiber with a 20 μm diameter core, 128 μm cladding and 260 μm outer coating (CorActive DCF-YB-20/128P-FAC). The core of this fiber has a numerical aperture of 0.075 which is large enough to support the propagation of a few higher-order modes. However, we have observed the majority of the TA output power not contained within the TEM_{00} mode exists in transverse modes of significantly higher-order. These modes cannot propagate through the fiber, thus the fiber acts as a spatial filter.

We angle polish the fiber tips to ensure efficient coupling of radiation into the fiber, as well as to prevent back-reflections off the faces of the fiber that could cause lasing at parasitic wavelengths.

The fiber is prepared by removing $\approx$ 1 cm of outer cladding from both ends using a hot jacket stripper (AFL: RS02 Thermal Stripper) with a FH-100-250 Fiber Holder. The fiber is then placed in an angled ceramic ferrule and angle-polished by hand using a variety of Thorlabs diamond, aluminium oxide, and calcined alumina lapping paper. During this process, the quality of the finish of the fiber face is inspected using a Thorlabs fiber microscope (Thorlabs: FS201). The fiber is then mounted on a stainless steel mount with a V-groove, with metal end clamps holding the fiber in place near each end.

Although the fiber preparation instructions above seem straightforward, reaching this method required a lot of very frustrating trial and error. From the beginning we knew we needed angled ends and faced several problems. The first was removing the outer jacketing from the fiber. The outer jacketing is soft and protects the brittle Yb-doped silica fiber within. We attempted to remove the jacketing with a hand-held fiber stripper, but would often break off several centimeters of the fiber in the process. With the amount of fibers we went through in the beginning as we refined our techniques, and a pricetag of $\sim$ 750 \$/m, this was very wasteful. The hot jacket stripper solved this problem. The stripper works by fixing the portion of the fiber that will remain unstripped in a slidable v-groove holder. The portion of the fiber jacketing that is stripped is then sandwiched gently between two heating plates. As the v-groove portion of the stripper is moved away from the heating plates, the jacketing is removed and the bare fiber moves away from the plates freely.

With this problem resolved, the next difficulty was achieving an angle polish. While angle cleavers and angle polishers exist, our inspection of flat cleaved fibers with the fiber microscope revealed unsatisfactory finishes to the fiber surface, and angle polishers were a significant investment. Therefore, we honed our angle polishing skills. We purchased ceramic ferrule fiber connectors (Thorlabs B30140E1) matching the inner cladding diameter of the fiber as closely as possible. We then inserted the ceramic ferrule connector into an angled polishing puck (Thorlabs D50-FC/APC) at 8°, and polished the ferrule on diamond lapping paper, creating an angled ceramic ferrule. At this point, we inserted the ceramic ferrule into a bare fiber terminator (Thorlabs BFT1). The fiber is placed through the terminator until the bare fiber is barely visibly protruding from the

ceramic ferrule tip. At this point, the terminator clamps down on the fiber jacketing, fixing the fiber in place. Originally, we used a series of different grit diamond lapping paper for angle polishing the fiber tip as diamond lapping paper is recommended for ceramic ferrules. The first step used 6 μm grit (Thorlabs LF6D). As the bare fiber is still protruding at this point, this step required the most finesse. The lapping paper must be held in free space while the fiber is gently polished flush with the ceramic ferrule with minimal pressure. The "flushness" of the fiber tip is quantifiable two ways. First, when flush and inspected with the fiber microscope, the fiber tip should come in focus with the ceramic ferrule at all points. Second, when flush, the gentle polishing on the 6μm paper should sound very smooth with no scritch-scratch sounds. If this step is done correctly, the remaining polishing is generally successful.

Originally, after the 6μm diamond lapping paper, we would then polish on 3μm followed by 1μm grit diamond lapping paper intended for polishing ceramic ferrules (Thorlabs LF3D and LF1D). These finer grit papers were not held in free space, but instead placed on a silicone polishing pad (Thorlabs NRS913A) on top of a glass polishing plate (Thorlabs CTG913). While good angle polishes could be achieved with this method, it was common for the fiber tip to get chipped severely on the edges in the process. We believe this is because the diamond lapping paper would polish off bits of the ceramic ferrule which would then collide with the fiber tip while polishing, chipping the edges. This was supported when we more carefully read the product description of the diamond lapping paper. The diamond lapping paper was recommended for ceramic ferrules, versus cheaper lapping paper like silicon carbide, as it does not cause undercutting in which the fiber material is removed more quickly than the ferrule material, creating a dip just above the fiber. This is a problem when trying to connect two ceramic ferrules as it creates a glass-air-glass interface instead of a glass-glass interface. However, for us, we wanted to removed the fiber material more quickly than the ferrule material as removing the ceramic ferrule material was damaging our polish process. Therefore, we switched to these cheaper lapping papers designed for use with stainless steel ferrules. We still start with the LF6D diamond lapping paper to make the fiber flush with the ceramic, but for the polising on the pad and plate we use 3μm and 1μm grit aluminum

oxide (Thorlabs LF3P LF1P) followed by 0.3μm grit calcined alumina paper (Thorlabs LF03P). Using this technique, we can reproduce quality angle polishes on both sides of the fiber in less than 1 hour. The best method for inspecting the quality of the final finish is by pointing the fiber microscope at a ceiling light while rotating the fiber tip, looking for any shadows formed by ridges or grooves on the surface of the fiber.

As seen in Fig. 2.5, the angle-polished fiber is pumped using a high-power, fiber-coupled (NA = 0.22) laser diode array at 915 nm from nLight photonics (nLight element e06). The pump diode is mounted on a water-cooled aluminum block and powered with a high current source. The output power of the pump as a function of current is shown in Table 2.3, along with the pump power remaining after passing through the fiber. This data was taken for a 10 cm long fiber, and no seed light was present, but is useful for optimal alignment of the pump light into the fiber.

Table 2.3: Pump Output and Absorbed Power

Current (A)	Output Power (W)	Remaining Pump Power (W)
0.60	0.37	0.22
1.0	2.60	1.73
2.0	8.24	5.90
3.0	13.90	10.20
4.0	19.40	14.36
5.0	24.75	18.28
6.0	29.80	21.90
7.0	34.25	25.20
8.0	42.30	28.20
9.0	45.70	31.26
10.0	45.71	NA

Another important characteristic about the nLight pump diode is that the wavelength shifts with current. Fig. 2.6 shows the spectrum of a higher power nlight pump diode at 915 nm (nLight element e18) taken at low and high currents (1 A and 10 A), demonstrating a near 20 nm shift in center wavelength. This is slightly greater than the manufacturers specification of 1 nm/A, which could be attributed to the pump diode heating up as there is also a 0.32 nm/°C wavelength

dependence on temperature. This effect was important when explaining the performance of our Yb-fiber as pump current increased.

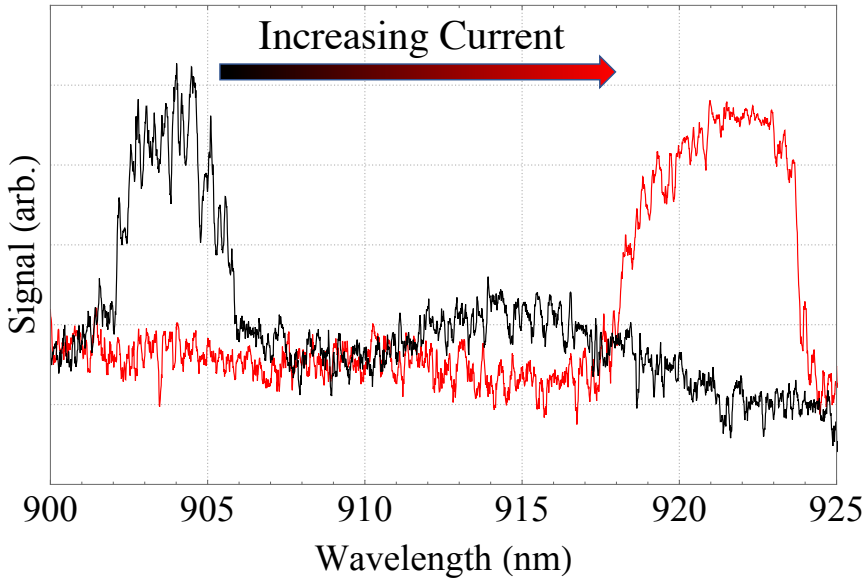

Figure 2.6: Spectrum recorded on an optical spectrum analyzer (Thorlabs OSA202C) of the 915 nm pump diode at low and high currents. The center peak shifts over $\approx$ 20 nm over this range.

As seen in Fig. 2.5, the 915 nm pump light is collimated with an aspheric lens and pumped in the reverse direction of the 972.5 nm light propagation. The pump radiation is overlapped with the 972.5 nm radiation and both are coupled to the Yb-fiber using aspheric lenses mounted on flexure stages. To overlap the pump and signal for this process we combine both beams using two shortpass filters at 950 nm (F3 and F4), and subsequently separate both beams using a longpass filter at 950 nm (F2) after the pump exits the Yb-fiber in the reverse direction. We use two shortpass filters when we combine the pump and amplified 972.5 nm light as the high power 972.5 nm radiation can damage the fiber pump diode if it is coupled into the pump. We believe this destroyed one of our first pump diodes, when we only used one shortpass filter. With two shortpass filters we have not observed this effect. After the amplified 972.5 nm light is separated from the pump radiation, it is then passed through another $OD_{abs} > 5$ spectral filter (F5) centered at 972.5 nm with $\approx$ 4 nm FWHM bandwidth to remove amplified ASE before the frequency conversion process.

2.4.4 Yb-fiber Amplifier Performance

Fig. 2.7 shows the backward propagating radiation from the Yb-fiber amplifier measured off of filter F1 in Fig. 2.5 when pumping with 22.5 W of 915 nm radiation. Without seed power, the high inversion favors gain at 975 nm. With seed power, the peak at 975 nm is still dominant; however, this is due to ASE from the TA which is incompletely attenuated by filter F1 in Fig. 2.5. Back reflections from the output facet of the amplifier fiber also cause this radiation to be amplified in the reverse direction, along with a small amount of the 972.5 nm radiation. Without seed, the integrated power in Fig. 2.7 is $\approx$ 270 mW, but this drops to only $\approx$ 9 mW when seeded. The ASE is roughly linear with pump power, and therefore does not significantly degrade the amplifier performance for this short length of fiber.

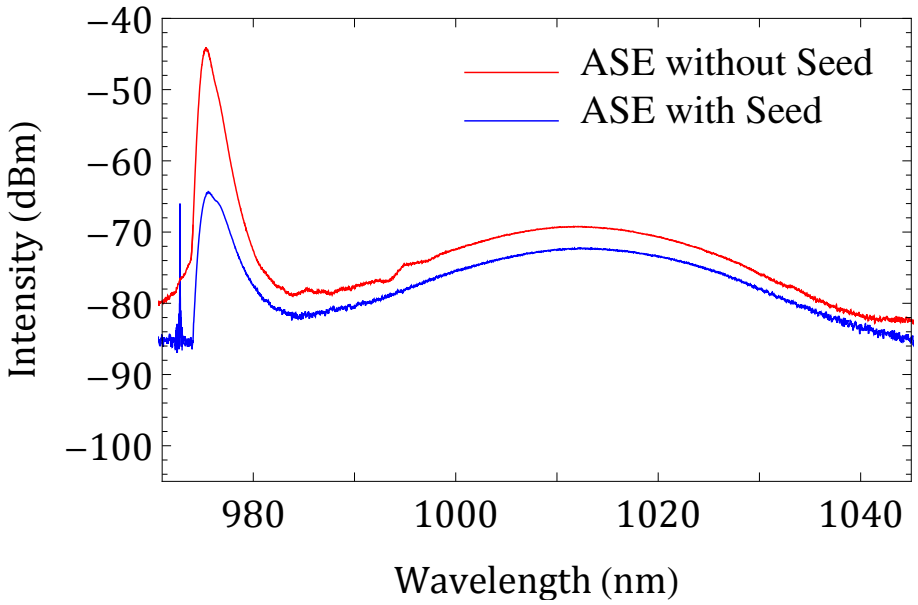

Figure 2.7: Backward propagating radiation from the Yb fiber amplifier with and without seed. Both spectra were taken with 22.5 W of pump power at 915 nm.

The 972.5 nm output power of the fiber amplifier as a function of 915 nm pump power is shown in Fig. 2.8. Amplification of the 2.4 W of seed occurs at $\approx$ 15 W of pump power. However, even with zero pump power, significant inversion of the gain medium can occur due only to the input seed radiation, so that the fiber exhibits semi-transparency before the amplification threshold. At

our maximum pump power of 41.5 W, we obtain an output power of 6.3 W at 972 nm, corresponding to a gain of 4.2 dB. The rolloff at high pump power is a result of the pump wavelength shifting away from the absorption peak at 915 nm as the diode current is increased (see Fig. 2.6). This effect is more pronounced in our system due to the low absorption of the pump. Our model predicts that more power at 972.5 nm could be obtained with a pump diode that provides 130 W of output power and reaches the 915 nm absorption peak at a higher power.

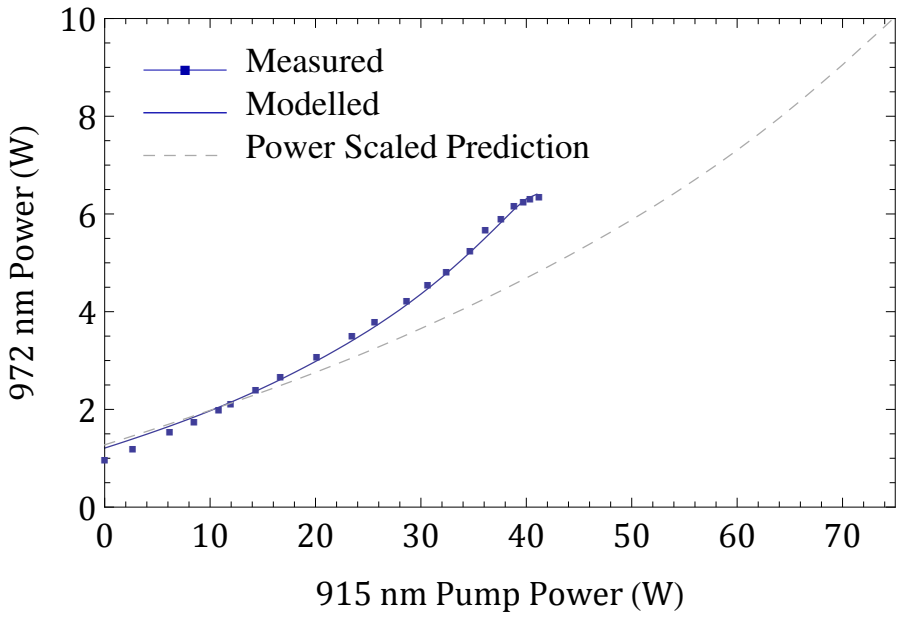

Figure 2.8: Measured radiation at the output of the fiber amplifier as a function of 915 nm pump power. A linear fit to our data indicates a slope efficiency of $\approx 13\%$. The measured values agree well with a theoretical model (solid line) based on [43]. The rolloff at high pump power is due to an increase of the pump wavelength as the diode current is increased. Our model predicts that more power at 972.5 nm could be obtained with a pump diode that provides 130 W of output power (dashed line) and reaches the 915 nm absorption peak at a higher power.

2.4.5 Power Scaling and Power Stability

While the model shown in Fig. 2.8 predicted significantly more 972.5 nm was possible by pumping our Yb-fiber amplifier with more power, replacing the lower power pump diode with one capable of 3-4 times more power required significant re-engineering of our laser system. There were two severe limitations with the Yb-fiber amplifier in the original design that would become

worse with power scaling. The first was the mounting of the fiber. The fiber was mounted on a v-groove holder (Thorlabs HFV001 or HFV002). The bare fiber would protrude from the ends of the v-groove holder, into free-space. The fiber was fixed at the edge of the v-groove holder with rubber magnetic clamps. The amount of bare-fiber protruding is important. Too much bare-fiber hanging off the v-groove holder caused instabilities due to unwanted motion of the fiber tip. While this could be mitigated with less bare fiber overhanging, if the fiber was too close to the v-groove holder, the holder could heat up from pump radiation not coupled into the fiber. Multiple times we saw the entire fiber spontaneously combust, starting at the rubber magnetic clamps on the side of the fiber in which we coupled the 915 nm pump power. We attributed this to the rubber heating up to the point of catching on fire, which would then provide enough thermal energy to catch the jacketing on fire, destroying the fiber. We mitigated this problem by securing the fiber with metallic clamps without any combustible material. These clamps were in fact just one of the V-groove holders (HFV001) placed upside down on top of the fiber. With these clamps, we have not seen the fiber spontaneously combust. Unfortunately, these clamps can only secure the jacketing portion of the fiber, whereas the rubber clamps could apply pressure to any bare fiber remaining in the v-groove holder. Therefore, we believe the fiber has more freedom for movement with these clamps.

With this problem fixed, there was still another problem with our Yb fiber we needed to address before increasing the pump power. The fiber tip would sometimes catch fire. This was different from the spontaneous combustion as the reaction would occur at the tip, and only burn a few mm. The burn would stop as the bare silica would fuse into a ball, stopping the flame from spreading. We noticed that the likelihood of the fiber tip to burn was correlated to days with increased dust activity in the lab. At this point in the laser design, there were no hepafilters on the optical tables, and the laser system was not enclosed by a box. Installing hepafilters, enclosing the laser in a box, and monitoring the dust activity with a particle counter, we were able to mitigate the fiber tip burning.

With these improvements in our laser design, we upgraded to a pump diode capable of generating 155 W of power at 915, almost quadruple our previous pump power capability. This pump diode is also a fiber coupled, laser diode array system from nLight (nLight element e18), with the same fiber NA = 0.22 as the previous low power pump diode. Table 2.4 shows the output power of this pump diode as a function of current.

Table 2.4: High Power Pump Output Power

Current (A)	Pump Power (W)	Center Wavelength (nm)
0.7	0.32	NA
1.0	3.82	903.8
2.0	16.34	904.9
3.0	28.74	905.7
4.0	41.88	906.8
5.0	55.20	907.8
6.0	71.17	909.4
7.0	83.24	910.4
8.0	96.61	912.1
9.0	109.98	913.6
10.0	123.34	915.1
11.0	136.71	917.1
12.0	150.08	919.1

A plot of the Yb fiber amplified 972.5 nm power versus launched 915 nm pump power for this more powerful pump diode is shown in Fig. 2.9. As predicted in Fig. 2.8, we see a linear increase with IR output as a function of pump power. With 120 W of pump power, we are able to generate 10.8 W of power at 972.5 nm. Fortunately, our previous engineering worked, and even with tripling the pump power we did not see spontaneous combustion of the fiber or burning of the fiber tip. However, we did see new issues caused by thermal instabilities. One of these was cracking of the achromatic lenses we were using for coupling into and out of our pump-diode and Yb-fiber. We originally used achromatic doublets with f = 10 mm and 8 mm optical diameter (Thorlabs AC-080-10-B-ML) in the low power system as we saw the best fiber coupling with these lenses. However, the achromatic doublets consist of two-optics cemented together, and at the

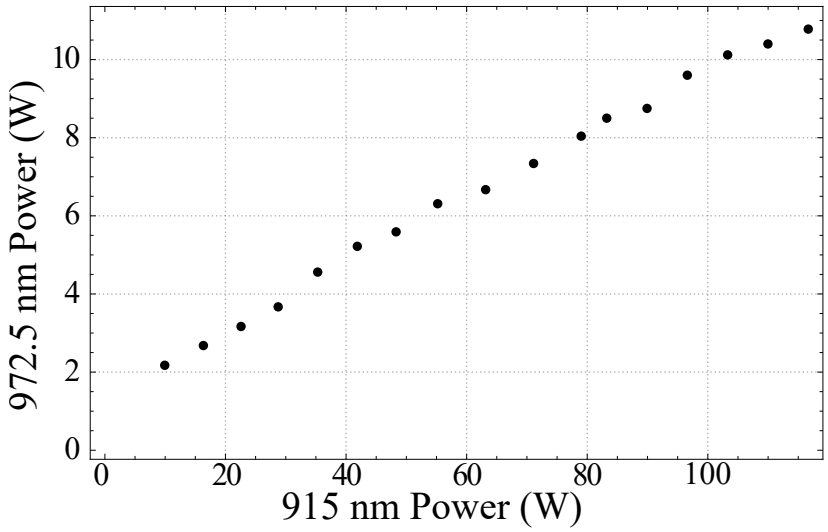

Figure 2.9: Measured 972.5 nm Yb fiber output power vs. launched 915 nm pump power for more powerful pump diode. With zero pump power, the 972.5 nm Yb-fiber output power does not pass through zero as the seed power at 972.5 nm is large enough to invert the medium to a point of semi-transparency.

high pump powers several of these doublets developed cracks. We believe the cracks could have developed by thermal stress caused by heating the mounting holding the doublets. Therefore, we switched to polished aspheres of the same focal length (f = 10 mm) (Thorlabs AL1210M-B), which had a larger optical diameter (12.5 mm diamter) and were one solid optic. These new lenses have not cracked at the increased pump powers. The increased pump power also requires significant thermal management of the fiber mount and coupling lens mounts as Fresnel reflections off the fiber tips and scatter off the optics heats these components. This causes amplitude instabilities in the 972.5 nm power output as the coupling to the fiber is highly sensitive to any thermal induced motion. We currently address these issues using radiation shields and water cooling of the lens mounts and fiber v-groove holder, as well as a water cooled beam-trap for the 915 nm pump power that is not absorbed within the fiber and reflected off of filter F1 in Fig. 5.3.

With these new thermal management techniques, we can maintain stable IR power > 10 W for time periods greater than 1 hour as seen in Fig. 2.10. We have run the system for a combined duration greater than 20 hours at these high powers, and see no evidence of degradation from photodarkening. Overall, we believe this system is still power scalable with more pump power, but further thermal management caused by the free-space coupling could prove exhausting. We

are currently investigating pump combiners that combine the signal and pump beam into one fiber, which will then be spliced to the Yb-fiber.

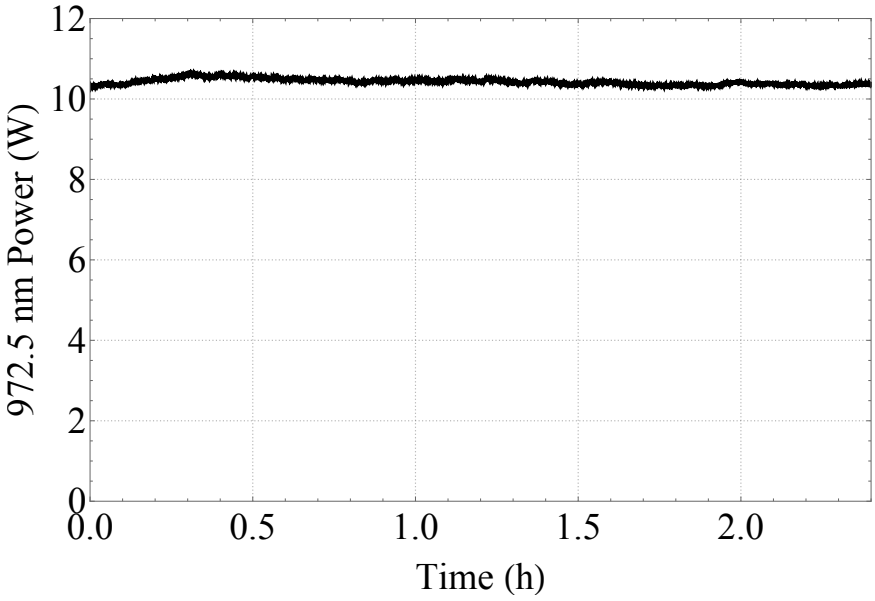

Figure 2.10: The power stability of the amplified 972.5 nm radiation.

2.5 Frequency Stabilization and Coherent Comb Lock

To perform precision spectroscopy on simple and exotic atomic species, it is imperative that the laser frequency is well-controlled and determined. Control over the absolute frequency of the 243.1 nm radiation is also necessary to perform two-photon Doppler-cooling on atomic hydrogen beams. Additionally, a narrow-linewidth laser is especially critical for a frequency-quadrupled system. For semiconductor laser sources, each two-photon process quadruples the spectral linewidth [42, 109]. Besides increasing the linewidth, these multi-photon processes associated with frequency doubling reduce the amount of power in the optical carrier, which reduces the excitation efficiency for narrow spectroscopic transitions. With a $\approx$ 1 Hz natural linewidth, this is a serious problem for two-photon spectroscopy of the 1S-2S transition in hydrogen, especially considering that three two-photon processes are involved. For two-photon spectroscopy of the 1S-2S transition in hydrogen using a frequency quadrupled 243.1 nm laser source, these three two-photon processes are: 1)

Doubling from 972.5 nm to 486.3 nm 2) Doubling from 486.3 nm to 243.1 nm, and 3) Two-photon excitation of the 1S-2S transition. These three processes reduced the excitation efficiency of earlier frequency-quadrupled MOPA 243 nm systems to 40 % compared to if all the power remained in the carrier [30,42,110]. However, in [42], they demonstrated that a long ECDL ($\approx$ 20 cm) stabilized to an ultra-stable reference cavity had no measurable losses in the excitation efficiency of the 1S–2S transition as a result of these two-photon processes.

For these reasons, and as shown in Fig. 2.11, we establish a narrow linewidth source by actively stabilizing our ECDL to a pre-stabilization reference cavity which consists of relatively high reflectivity mirrors at 972.5 nm (R = 99.8 %) mounted on a zerodur cylinder and vibrationally isolated from the environment. Then, for absolute frequency conrol, we can adjust the reference cavity's length to lock the oscillator to a coherent, GPS referenced frequency comb [111].

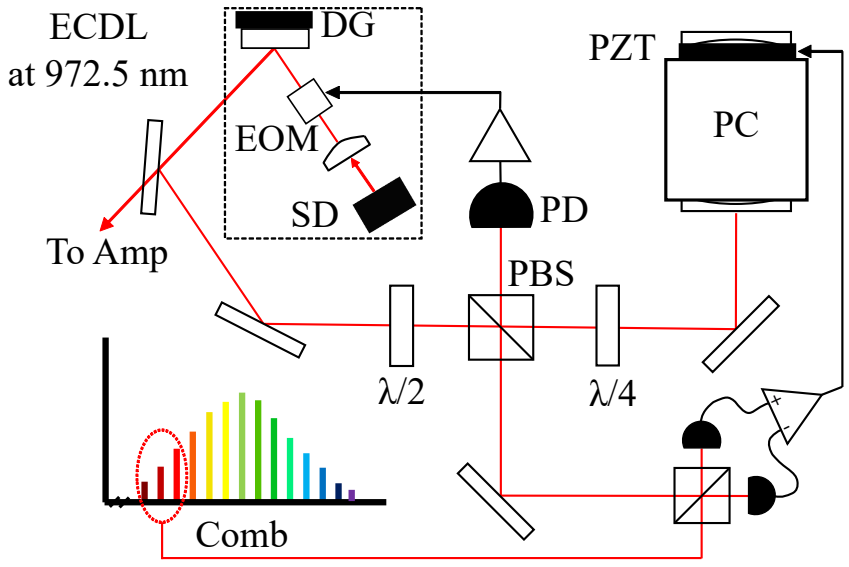

Figure 2.11: Schematic of the 972.5 nm locking system. SD: seed diode, EOM: electro-optic modulator, DG: diffraction grating, ECDL: extended cavity diode laser, $\lambda/2$: half-wave plate, $\lambda/4$: quarter-wave plate, PBS: polarization beam-splitter, PD: photodiode, PC: pre-stabilization cavity, PZT: piezo-electric transducer. Frequency stabilization of the master oscillator at 972.5 nm involves simultaneous locking to a pre-stabilization cavity and an optical frequency comb. Feedback from the PC to the master oscillator is done with an EOM internal to the ECDL, whereas a PZT on the PC is used to lock the frequency of the 972.5 nm radiation to the frequency comb.

The beat note between the oscillator and the frequency comb is shown in Fig. 2.12. This beat note, along with the in-loop error signal with the pre-stabilization cavity, quantifies the noise performance of our system. By integration of the phase noise on these signals, S_ϕ, we determine the linewidth of the 972.5 nm light, Δ, which is given by $\int_\Delta^\infty S_\phi df \approx 1\,\text{rad}^2$ [112].

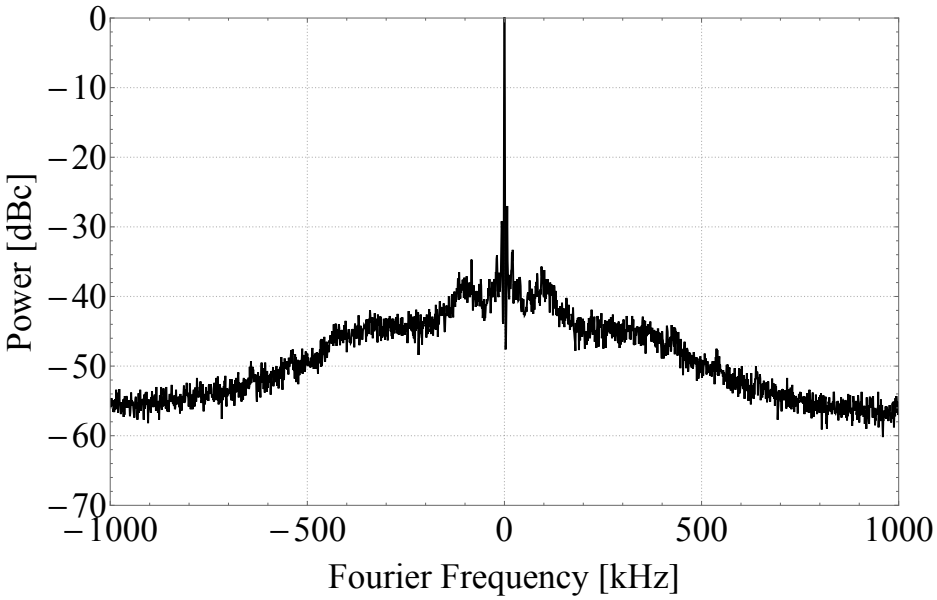

Figure 2.12: RF spectrum of the coherent beat note between the master oscillator at 972.5 nm and frequency comb taken at a resolution bandwidth of 1 kHz.

Determining the laser phase noise on the beat note requires discriminating between actual laser noise and frequency comb noise. However, the beat note in 2.12 doesn't distinguish between these two. This is why we needed to look at the frequency spectrum of the in-loop error signal and compare it to the frequency spectrum of the comb, as this tells us the pre-stabilization cavity's ability to suppress noise on the laser. The frequency spectrum of the in-loop error signal can be found by analyzing the error signal of the stabilization cavity while locked with a spectrum analyzer. The error signal power spectrum in dB can be converted to voltage. The voltage excursion of the error signal can be converted to frequency excursion through the error's signal relation to the linewidth of the cavity [113]. Therefore, the raw error signal power spectrum data can be translated to the frequency spectrum of the laser. This conversion is shown in Fig. 2.13.

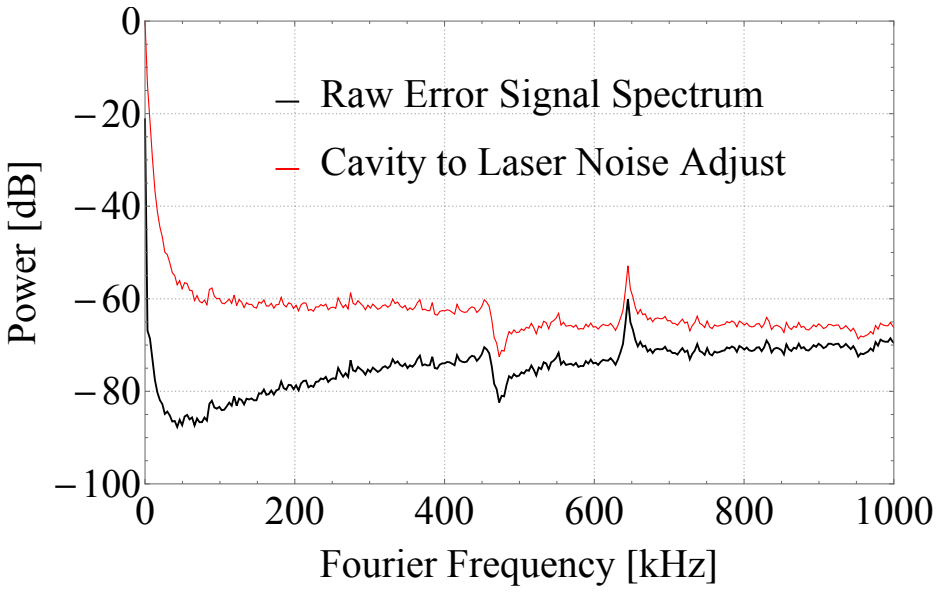

Figure 2.13: Raw RF spectrum (black) of in-loop error signal of the pre-stabilization cavity as well as the translation to laser noise (red).

We can now compare the laser noise from the pre-stabilization cavity with the noise introduced by the frequency comb. Overlapping these two signals, along with the original beatnote in Fig. 2.14, we can figure out over which spectral regions each component contributes to the noise. We see that at frequencies greater than 100 kHz, the beat note's noise matches that of the comb, which masks that the laser noise is actually much smaller due to the significantly reduced noise perfromance from the pre-stabilization cavity at these high frequencies. However, at frequencies < 100 kHz, the beat note noise does not match the comb noise, and instead increases along with the noise from the pre-stabilization cavity. Therefore, at these frequencies the beat note shows actual laser noise. Therefore, for determining the linewidth, we integrate the phase noise from the pre-stabilization cavity at frequencies greater than 100 kHz, and at frequencies less 100 kHz, integrate the phase noise from the beat note.

Using this method, we estimate that $\approx 95\%$ of our optical power at 972.5 nm is in the coherent carrier, and that the fundamental linewidth is < 100 Hz. While the percentage of power in the carrier is degraded through frequency quadrupling [42, 109], we estimate the linewidth at 243.1 nm is < 10 kHz. This is sufficient for spectroscopy on muonium and positronium due to the

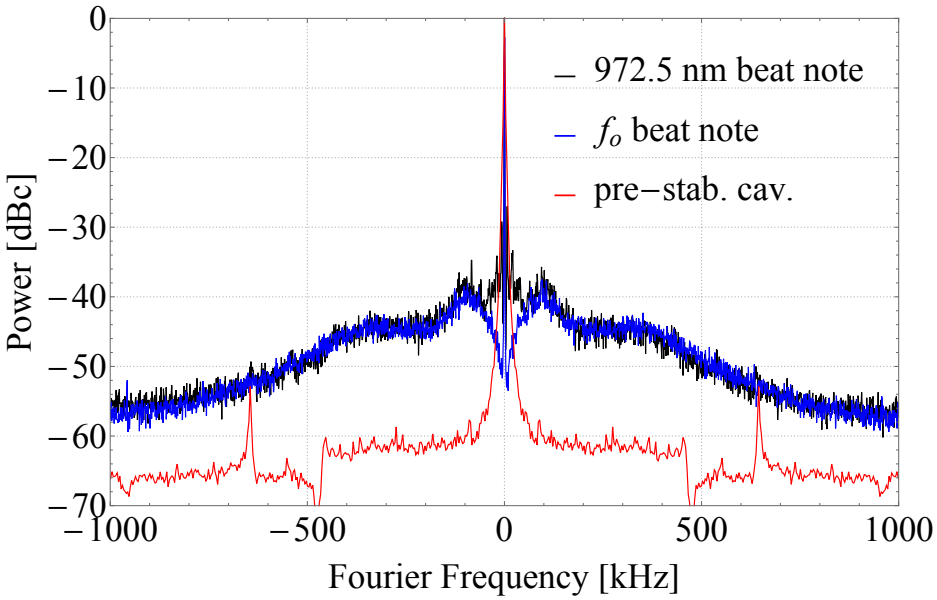

Figure 2.14: RF spectrum of frequency comb, 972.5 nm beat note with comb, and pre-stabilization cavity

short lifetime of the species; as well as two-photon laser cooling of hydrogen since the transition would be broadened substantially by coupling the 2S state to the 2P state for quenching [24, 25]. However, for state-of-the-art hydrogen spectroscopy on the 1*S*–2*S* transition [5, 110], the linewidth of our source would need to be reduced further. Currently, the pre-stabilization cavity has a relatively low finesse of $\approx$ 1000, and a higher finesse cavity would be needed to compensate for the low frequency noise that is currently dominating our linewidth, as well as further isolation from environmental noise. Nonetheless, the linewidth of our source meets the requirements for our next two proposed experiments with a frequency quadrupled 972.5 nm laser source. In both these experiments, the use of a high power 243.1 nm laser is not for spectroscopy but for strongly driving the 1S-2S transition. The first experiment is spectroscopy of the 2S-8D transition. Here, the stringent linewidth requirements are placed on the laser exciting this transition; whereas a high power 243.1 nm laser is useful for exciting a large portion of atoms to the metastable 2S state. The second proposed experiment is laser cooling where large scattering rates make the cooling faster. As explained in the introduction, this would require quenching to the 2P state, giving the 2S state an effective linewidth of 50 MHz, well above the linewidth of our laser.

2.6 Conclusion

In conclusion, we have demonstrated a power scalable, 972.5 nm laser system consisting of a MOPA and Yb-fiber amplifier [114, 115]. Currently, the system can generate > 10 W of narrow frequency, stable output power at 972.5 nm for time periods greater than one hour. This is an impressive result for a Yb-fiber system, as gain is much more favorable in Yb-fibers at wavelengths > 1 μm. While gain near the absorption/emission cross-section peak at 975 nm is also possible, only a handful of high power Yb-fiber systems exist. Of these, only one has demonstrated narrow linewidth operation, utilizing a design similar to the system described here. To the author's knowledge, achieving high-power in Yb-fibers below this absorption/emission cross-section peak is a unique and challenging accomplishment, due to the gain competition at more favorable spectral regions. We overcame these challenges by using a short fiber length with a large core/cladding ratio, large seed power, and high inversion.

The current system is limited by available pump power, but as was demonstrated, increasing pump power is a viable method for increasing the 972.5 nm output power of this system. However, our current system currently uses free space coupling for both the pump power and seed power, which requires significant thermal management for stable operation. These problems could be mitigated by switching to a majority fiber based amplifier system. Since the pump has a fiber coupled output, this could be easily spliced to a passive multi-mode fiber. As well, the seed power from the TA could be easily coupled into a passive single-mode fiber. Using a fiber pump combiner, a common piece of equipment for fiber laser systems, both the multi-mode pump fiber and single-mode seed fiber would be combined into a passive multi-mode fiber that matches the geometry of our Yb-doped fiber. This could then be spliced to the Yb-doped fiber, and the only free space coupling would be the output coupling of the amplified 972.5 nm radiation and remaining pump light. This would be a significant reduction in free space coupling of high powers compared to our current system, and should be investigated for increasing the stability and robustness of our system.

Other options to improve the performance of our system include a different fiber geometry and/or more seed power. A Yb-doped fiber with larger core/cladding ratio would help combat gain at the undesirable, more favorable spectral regions. To our knowledge, our current fiber has the largest core/cladding ratio available commercially that also has demonstrated photodarkening free performance at high powers. However, we could investigate custom solutions with commercial companies or collaboration with fiber research groups to have such a fiber developed. Regarding more seed power, our current seed power is limited by the output of the MOPA, which is limited by the tapered amplifier output of 3 W. Progress in Vertical-External-Cavity Surface-Emitter Lasers (VECSELs) have created $\approx$ 5 W of power at 972.5 nm, tunable over several nm [116]. While such a device does not commercially exists, collaboration with a VECSEL group is worth exploring.

Of all these possible improvements, the Yb-fiber amplifier remains the critical component for achieving high power. We have demonstrated the capability and reliability of this component in our laser system, but the usefulness of this system comes from frequency conversion to shorter wavelengths. As the MOPA is tunable from 972.5-976 nm with narrow linewidth output, frequency conversion could be used for positronium spectroscopy (486.3 nm) [117], muonium spectroscopy (244 nm) [32], as well as studies of hydrogen and anti-hydrogen (243.1 nm). Furthermore, these wavelengths are useful for Raman spectroscopy and laser interference lithography [37, 39, 40]. The other high power Yb-fiber lasers at 975 nm were either too broad in linewidth for efficient frequency conversion, or had not yet demonstrated frequency conversion. In the next chapter, we demonstrate that our Yb-fiber system is compatible with efficient, high-power frequency conversion into the blue and deep-UV spectrum.

Chapter 3

Watt-level, Coherent Deep-UV Generation via Frequency Quadrupling

3.1 Introduction

Motivated by improving spectroscopy of simple and exotic atoms, laser cooling hydrogen, and the general utility of a high-power deep-UV laser, we developed the Yb-fiber amplifier described in Chapter 2 that is tunable from 972.5-976 nm for the specific intention of frequency converting it to these shorter blue and deep-UV wavelengths. In this chapter, both the design and performance of the frequency doubling stages we use to generate blue and deep-UV radiation from our Yb-fiber amplifier system are presented. Through frequency quadrupling the > 10 W 972.5 nm power available through our Yb-fiber amplifier, we can generate > 1 W of narrow linewidth 243.1 nm radiation (< 10^4 Hz) that is stable for time periods greater than one hour. To the best of our knowledge, this is the highest power deep-UV, CW laser below 266 nm.

This chapter begins with a brief review of nonlinear interactions with focused Gaussian beams, with an emphasis on how to calculate the single-pass, frequency-doubling conversion efficiency for a focused Gaussian beam passing through a nonlinear crystal. The chapter then reviews the basic theory of continuous wavelength (CW) enhancement cavities, applying this theory to CW second harmonic generation with a CW enhancement cavity. This section presents many practical equations for calculating the frequency doubled power which can be achieved with a given amount of fundamental input power. The theory portion of this chapter ends with a discussion of ABCD matrix analysis for a second harmonic generation enhancement cavity, which is useful for the initial design of such a cavity.

The chapter then presents the design and performance of our first frequency doubling stage, which converts 972.5 nm radiation to 486.3 nm radiation using Lithium Triborate (LiB_3O_5) as the

nonlinear medium. Following this, the design and performance of the second doubling stage, which uses Cesium Lithium Borate ($CsLiB_6O_{10}$) as the nonlinear crystal to generate 243.1 nm radiation is presented. The chapter concludes with a demonstration of the precise frequency control of our UV radiation via excitation of the 1S-2S transition in hydrogen.

3.2 Frequency Doubling Theory and Considerations

3.2.1 SHG Efficiency with Gaussian Beams

The optical response of a medium to an electric field is describable by the polarization, which can be expressed as a power series in the electric field strength [118]

$$\mathcal{P}(t) = \epsilon_o[\chi^{(1)}E(t) + \chi^{(2)}E^2(t) + \chi^{(3)}E^3(t) + ...], \tag{3.1}$$

where $\chi^{(i)}$ is the ith order susceptibility and $E(t) = E_o e^{i\omega t}$. For sufficiently small electric fields, the non-linear optical susceptibilities (i of order 2 or higher) of a material are negligible, and the polarization only depends linearly on the electric field. For sufficiently strong electric fields, Eq. 3.1 indicates that the atomic response of a medium will include oscillations at harmonics of the electric field's fundamental frequency. If two electric fields are present, then the response will include oscillations at differences and sums of the two fundamental frequencies. Practical applications of these useful frequency conversions requires materials with large non-linear susceptibilities, as well as strong, electric fields. When the oscillation of all atoms are phase matched, the radiated power from each dipole adds constructively, resulting in a coherent beam of frequency converted radiation.

The advent of the laser gave access to intense, coherent electric fields in the optical regime. In 1961, the first demonstration of optical frequency doubling was demonstrated. Using a pulsed Ruby laser at 694 nm and quartz as the nonlinear crystal, second harmonic radiation at 347 nm was generated [119]. While the editor initially mistook the measurement as a speck of dust and

removed the result in the original publication, the importance of this initial demonstration of Second Harmonic Generation (SHG) was thankfully not lost. SHG has proved invaluable for optical physics as it has enabled generation of coherent wavelengths in spectral regions where natural gain mediums for lasing are lacking. For example, we saw in Chapter 2 that rare earths can generate extremely high power lasers in the infrared. Therefore, frequency doubling these sources can create powerful coherent radiation in the visible spectrum, which can be frequency doubled again to generate UV radiation—the technique behind the laser design in this thesis, and a common technique in commercial laser systems.

The optimization of second harmonic generation by a laser beam within a nonlinear crystal was done comprehensively by Boyd and Kleinman in their 1968 theoretical study [120]. Over the last five decades, this seminal paper has been referenced thousands of times in articles utilizing SHG. Here, I will present a rough outline of the derivation leading to the useful result

$$P_2 = \gamma P_1^2, \tag{3.2}$$

where P_2 is the power of the frequency doubled radiation, P_1 is the power of the fundamental light, and γ is a factor that depends on a large number of parameters and properties of the crystal and interacting radiation. While understanding the full derivation is beneficial, for a graduate student that wants to figure out if their non-linear crystal is performing optimally, it is more useful to understand how to easily calculate γ. Optimizing and determining γ from the original paper requires a non-trivial amount of detective work. Here, the results are summarized, listing all the parameters in one convenient table, and guided calculation of γ for one of the crystals used in our work is presented.

The paraxial approximation was used in deriving Eq. 3.2. In this approximation, the electric field of a laser propagating in the z-direction within a crystal can be written as

$$\vec{E_1}(x',y',z') = \vec{E_o}\frac{1}{1+i\tau'}\exp(ik_1 z')\exp\left(-\frac{x'^2+y'^2}{w_o^2(1+i\tau')}\right)\exp(-\frac{1}{2}\alpha_1 z') \tag{3.3}$$

where all parameters are defined in Table 3.1. From Eqs. 3.1 and 3.3, the effective component of harmonic polarization responsible for generating the second harmonic (which is zero for points outside of the the crystal), is

$$\mathcal{P}_{eff}(x',y',z') = \mathcal{P}_{o,eff}\frac{1}{(1+i\tau')^2}\exp(2ik_1 - \alpha_1 z')\exp\left(-\frac{2(x'^2+y'^2)}{w_o^2(1+i\tau')}\right), \tag{3.4}$$

where $\mathcal{P}_{o,eff} \propto dE_o^2 \propto dP_1$ where d is the effective non-linear coefficient and P_1 is the power of the fundamental field. We are interested in the total power generated by the second harmonic; therefore, we need to determine the harmonic field outside the crystal for an observer at some point (x,y,z). This is given by

$$\vec{E_2}(x,y,z) = \vec{A_2}(x,y,z)\exp(ik_2 z), \tag{3.5}$$

To find $\vec{E_2}(x,y,z)$, in [120] they added up the incremental harmonic amplitude, $\mathrm{d}A_2$, contributed by a slab of thickness, $\mathrm{d}z'$, over the entire length of the slab, which using Eq. 3.4 can be written as

$$\mathrm{d}A_2(x',y',z') = \frac{2\pi i\omega_2}{cn_2}\mathcal{P}_{eff}(x',y',z')\exp(-ik_2 z')\mathrm{d}z' \tag{3.6}$$

At this point, the derivation becomes a series of integrals, which are detailed in [120]. The harmonic field, $\vec{E_2}(x,y,z)$ is found by integrating Eq. 3.6 over all the incremental slabs and through use of Eq. 3.5. As $I_2 \propto |E_2|^2$, the intensity distribution of the harmonic field can be found, and by integrating over this intensity distribution, the second harmonic power, P_2. These integrals are all done in the far field limit of the observer, and give the following result:

$$P_2 = Klk_1 e^{-\alpha^{'} l} h(\sigma, \beta, \kappa, \xi, \mu) P_1^2, \tag{3.7}$$

where

$$h(\sigma, \beta, \kappa, \xi, \mu) = \frac{1}{4\xi} e^{\mu\alpha l} \iint_{-\xi(1+\mu)}^{\xi(1+\mu)} \frac{\exp[-\kappa(\tau+\tau^{'}) + i\sigma(\tau-\tau^{'}) - \beta^2(\tau-\tau^{'})^2]}{(1+i\tau)(1-i\tau^{'})} d\tau d\tau^{'}. \tag{3.8}$$

From Eqs. 3.7 and 3.8, we then see that γ in Eq. 3.2 is

$$\gamma = \frac{1}{4\xi} Klk_1 e^{-\alpha^{'} l} e^{\mu\alpha l} \iint_{-\xi(1+\mu)}^{\xi(1+\mu)} \frac{\exp[-\kappa(\tau+\tau^{'}) + i\sigma(\tau-\tau^{'}) - \beta^2(\tau-\tau^{'})^2]}{(1+i\tau)(1-i\tau^{'})} d\tau d\tau^{'}. \tag{3.9}$$

Table 3.1 explains and defines the parameters used Eq. 3.9. The value for K is different from the value in [120] as it has been converted to SI units here. While this table looks somewhat formidable at first glance, for the ideal case with no phase mismatch, no absorption, and a focus at the center of the crystal, numerous of these parameters go to zero ($\Delta k, \alpha, \alpha^{'}, \kappa, \mu$), greatly simplifying the calculation. However, in practice, systems never perform at their ideal values, so the full form is given here as a useful tool to understand why a system might perform derated.

While several of the terms in Table 3.1 are straightforward, some of them require further discussion. These are terms highlighted in bold in Table 3.1, and are significant parameters in determining the performance of SHG within a non-linear crystal. One of these is d, the effective nonlinear coefficient. This term is inherent to the nonlinear crystal class and directly related to $\chi^{(2)}$. As the crystal class is based on the crystal structure, which have complex geometries, $\chi^{(2)}$ is a tensor element. Therefore, d can only be given for a fixed propagation direction and polarization direction in a crystal. Fortunately, these parameters are usually well defined to satisfy phase

Table 3.1: SHG Parameters

Parameters	Definiton	Description
ξ	$\xi = l/b$	
l		length of crystal (m)
b	$b = k_1 w_o^2$	double the Rayleigh length (m)
k_1	$k_1 = 2\pi n_1/\lambda_1$	wave vector of fundamental in medium (rad/m)
λ_1		wavelength of fundamental in vacuum (m)
w_o		**minimum beam waist of radiation**
K	$K = (8\pi d^2)/(\epsilon_o c \lambda_1^2 n_1^2 n_2)$	
d		**effective nonlinear coefficient (V/m)**
ϵ_o		permittivity of free space (F/m)
c		speed of light (m/s)
n_1		index of refraction at fundamental frequency
n_2		index of refraction at doubled frequency
$\alpha^{'}$	$\alpha^{'} = \alpha_1 + \alpha_2/2$	
α_1		absorption coefficient for fundamental (1/m)
α_2		absorption coefficient for doubled (1/m)
μ	$\mu = (l - 2f)/l$	position of focus ($f = l/2$ is centered)
α	$\alpha = \alpha_1 - \alpha_2/2$	
κ	$\kappa = (1/2)\alpha b$	
$\tau^{'}$	$\tau^{'} = 2(z^{'} - f)/b$	beam propagates in z-direction
τ	$\tau = 2(z - f)/b$	
σ	$\sigma = (1/2)b\Delta k$	
Δk	$\Delta k = 2k_1 - k_2$	**phase mismatch**
k_2		wave vector of doubled in medium (rad/m)
β	$\beta = \rho/\delta_o$	
δ_o	$\delta_o = 2w_o/b$	
ρ	Defined below	**double refraction angle (rad)**

matching, which is discussed next. Nonetheless, calculation of d is not trivial and it is common to instead determine this value through measurements.

Another bolded term in Table 3.1 is Δk, which defines the phase matching between the fundamental and second harmonic radiation. Since the index of refraction increases with frequency, the frequency doubled radiation, once generated, will travel slower through the nonlinear medium than the fundamental wave. Because of this, the frequency doubled light generated at the beginning of the crystal will lag behind and destructively interfere with light generated further along in

the crystal. To compensate for this dispersion effect, birefringence is used, hence why the choice for nonlinear mediums for second harmonic generation are crystals.

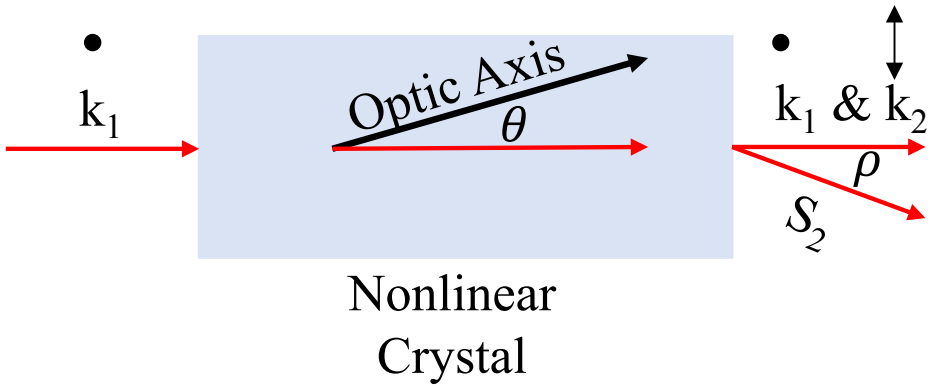

Figure 3.1: In type-I critical phase matching the fundamental radiation (k_1) is coupled into the crystal at an angle θ to the optical axis in order to make $\Delta k = 0$. This leads to walkoff of the second harmonic intensity (k_2) as the Poynting vector of this radiation (S_2) separates from the propagation direction, exiting the crystal with an angle ρ between k_2 and S_2.

A birefringent crystal has an index of refraction that depends on polarization and is generally described by an optical axis, an ordinary index (n_o), and an extraordinary index (n_e). For a negative uniaxial crystal, which are commonly used for second harmonic generation, there is one optic axis. Light that propagates along this axis does not experience birefringence and $n_o > n_e$, where n_o is independent of propagation direction, while $n_e(\theta)$ is dependent. The polarization of the fundamental is perpendicular to the plane defined by the direction of the fundamental of propagation and the optic axis, whereas the second harmonic is parallel to this plane. This angular dependence of the extraordinary index leads to the common technique of critical phase matching in which θ is varied such that $n_e(2\omega, \theta) = n_o(\omega)$. The phase matching angle is given by [121]

$$\theta_m = \arcsin \sqrt{\left(\frac{n_2^e}{n_1^o}\right)^2 \frac{[(n_2^o)^2 - (n_1^o)^2]}{[(n_2^o)^2 - (n_2^e)^2]}}, \tag{3.10}$$

where n_1^o, n_1^e are the ordinary and extraordinary index for the fundamental and n_2^o, n_2^e for the second harmonic, which can be calculated using the Sellmeier equations for a given crystal. While this method can make $\Delta k = 0$, it comes with an unwanted effect which leads to another of the bolded terms from Table 3.1, ρ, the double refraction angle. For θ_m other than 0° or 90°, the extraordinary ray experiences spatial walk-off as a result of the Poynting vector separating from the propagation direction, which is illustrated in Fig. 3.1. This reduces the overlap of the second harmonic beam with the fundamental, limiting the overall interaction region and resulting in an elliptic output beam for the second harmonic radiation. The amount of separation is called the double-refraction angle and is given by [121]

$$\rho = \arctan\left[\frac{1}{2}(n_1^o)^2\left(\frac{1}{(n_2^e)^2} - \frac{1}{(n_2^o)^2}\right)\sin(2\theta_m)\right]. \tag{3.11}$$

Although not possible in all crystals, walk-off can be mitigated by temperature phase matching, in which θ is fixed at 0° or 90° and the temperature of the crystal is varied such that $n_e(2\omega, T) = n_o(\omega, T)$. This is called noncritical phase matching.

The last bold parameter to mention in Table 3.1 is the beam waist of the fundamental laser radiation. In Boyd-Kleinman's paper, h is optimized as a function of ξ for several different values of $B = \rho\sqrt{lk_1}/2$. For example, for $\rho = 0$, $B = 0$, and $\xi_{opt} = 2.84$. As B increases, meaning increased double refraction, ξ_{opt} approaches 1.39, and [120] has several curves allowing readers to find ξ_{opt} for varying orders of double refraction in their crystal. From this the optimal focus for a defined crystal length can be calculated.

With these tools, the single pass conversion efficiency γ of a nonlinear crystal can be calculated and optimized. The calculation of γ in Eq. 3.9 can be done with Mathematica once the parameters are determined. For example, we use Cesium Lithium Triborate (CLBO) to convert 486.3 nm radiation to 243.1 nm radiation. For CLBO, $d = 0.95$ pm/V [122]. From the Sellmeier equations given in [123], the ordinary and extraordinary indices of refraction can be found for the desired operating temperature. At 20°C, the indices calculabe from [123] gives $\theta_m = 76.7°$ and $\rho = 18.6$

mrad, using Eqs. 3.10 and 3.11, respectively. For a CLBO crystal of length $l = 0.01$ m this gives $B = 3.35$, and from [120], the corresponding optimal value of $\xi_{opt} = l/(k_1 w_{o,opt}^2) \approx 1.5$. From this we see that $w_{o,opt} = 23\mu$m for a 10 mm long CLBO crystal. At the phase matching angle $\Delta k = 0$, and assuming no absorption at the fundamental or harmonic, as well as a focus in the center of the crystal, α, α', κ, and μ all go to zero. Plugging these parameters into Eq. 3.9 yields $\gamma_{CLBO} = 3.2 \times 10^{-4}$ W^{-1}.

For other common nonlinear crystals, this value is also $\sim 10^{-4}$-10^{-5} W^{-1}. This means that generation of a Watt or more power at the second harmonic could require hundreds of Watts at the fundamental power. This would require an extremely powerful CW laser. Fortunately, these powers can be reached in the CW regime by enhancing the fundamental power in a resonant enhancement cavity that also contains the nonlinear crystal.

3.2.2 CW Enhancement Cavity

Under the proper conditions, the electric field of a laser can build up inside an enhancement cavity. The result is that the intracavity power can be hundreds to thousands of times larger than the laser power outside the cavity. This buildup can compensate for the small values of γ, and the first use of enhancement cavities for second harmonic generation were described and demonstrated in the late 1960's [124–127]. Here, we present the basic theory behind optical enhancement cavities, and then intuitively apply these results to resonant second harmonic generation. The results presented mirror common theory for SHG within a resonator [126, 128, 129], with minor approximations to make the math more tractable.

The enhancement cavities described and used for frequency conversion in this laser system have a bowtie geometry. As seen in Fig. 3.2, such a cavity consists of an input coupler (IC), with electric field transmission t_o and reflectivity $r_o = 1 - t_o$. The other three mirrors are all highly reflective (HR) with reflectivities r_1, r_2, r_3. Two of these HR mirrors can have curvature, creating a focus in the cavity—a critical parameter for SHG. Ignoring the crystal and SHG at the moment,

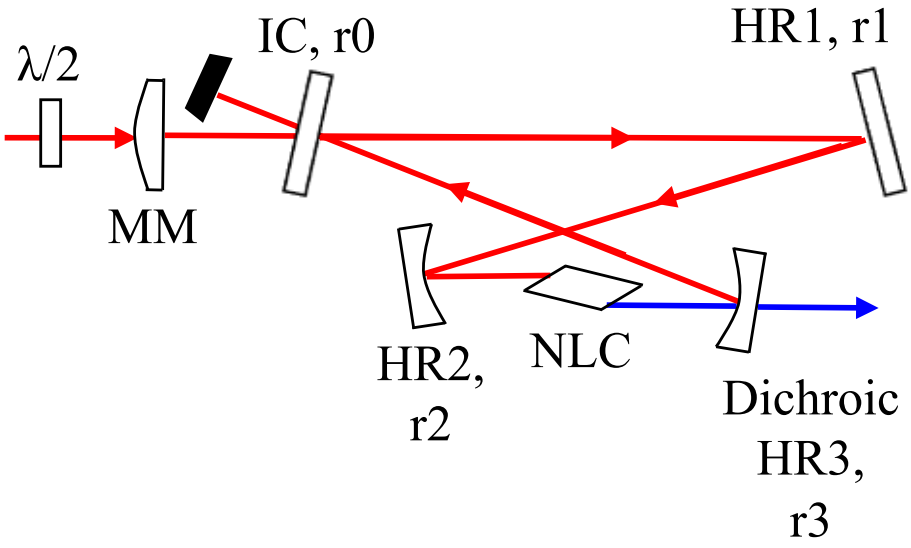

Figure 3.2: Second Harmonic Generation in an external bow tie cavity with a Brewster cut non-linear crystal (NLC). The fundamental radiation is coupled in through the input coupler, and a dichroic mirror is used to out couple the second harmonic radiation. $\lambda/2$: half-wave plate, MM: mode matching lens, IC: input coupler, HR1-HR3: high reflectivity mirrors where r_i are the electric field reflection coefficients.

the intracavity field follows the common intuitive derivation in which the electric field is added up after each round trip.

The initial field immediately after passing through the IC is $E_{cav} = E_o t_o$. After one complete round trip, $E_{cav} = E_o + E_o t_o (r_o r_n e^{i\phi})$, where $r_n = r_1 r_2 r_3$. The phase is given by $\phi = \frac{n\omega L}{c} + \phi_d(\omega)$ where n is the index of the cavity, ω is the frequency of the laser, L is the length of the cavity and $\phi_d(\omega)$ is any dispersive element. We see a pattern appearing, each round trip picks up a factor of $(r_o r_n e^{i\phi})$, meaning the total intracavity field after $N >> 1$ round trips is given by

$$E_{cav} = E o t_o (1 + r_o r_n e^{i\phi} + (r_o r_n e^{i\phi})^2 + ... + (r_o r_n e^{i\phi})^N) \tag{3.12a}$$

$$E_{cav} = \frac{E_o t_o}{1 - r_o r_n e^{i\phi}}, \tag{3.12b}$$

where the convenient form given by Eq. (3.12b) utilizes that $r_i < 1$ for all mirrors, which makes Eq. (3.12a) a convergent geometric series. In the lab, optical powers are measured; therefore, taking the squared modulus of Eq. (3.12b) gives a more convenient form

$$P_{cav} = \frac{T_o P_o}{1 + R_o R_n - 2\sqrt{R_o R_n}\cos\phi}, \tag{3.13}$$

where $R = r^2$ and $T = t^2$ are the optical reflectivity and transmission coefficients. Using $\cos\phi = 1 - 2\sin^2\phi/2$, this form can be rewritten as

$$P_{cav} = \frac{T_o P_o}{(1-\sqrt{R_o R_n})^2} \frac{1}{1 + \frac{4\sqrt{R_o R_n}}{(1-\sqrt{R_o R_n})^2}\sin^2\phi/2} \tag{3.14a}$$

$$= \beta P_o \frac{1}{1 + \mathcal{F}\sin^2\phi/2}, \tag{3.14b}$$

where $\mathcal{F} = \frac{4\sqrt{R_o R_n}}{(1-\sqrt{R_o R_n})^2}$ is the finesse and $\beta = \frac{T_o}{(1-\sqrt{R_o R_n})^2}$ can be thought of as the buildup of power in the cavity.

For a narrow linewidth, CW laser, $\phi_d(\omega)$ is ignorable. For a cavity kept on resonance, L is fixed such that $\sin^2\phi/2 = 0$. Therefore, for the CW resonant cavity described here, the intracavity power can be written as

$$P_{cav} = \beta P_o \tag{3.15}$$

$$= \frac{T_o}{(1-\sqrt{R_o R_n})^2}\, P_o, \tag{3.16}$$

which elucidates why β is referred to as the buildup. Lastly, since the reflectivities of cavity mirrors are generally quite high, writing Eq 3.16 in terms of transmission coefficients instead of reflectivity enables further simplification as the transmission coefficients are small quantities

$$\beta = \frac{P_{cav}}{P_o} = \frac{T_o}{(1-\sqrt{(1-T_o)(1-T_n)})^2}\ P_o \tag{3.17a}$$

$$\approx \frac{4T_o}{(T_o+T_i)^2}, \tag{3.17b}$$

where the approximation $\sqrt{1-T} \approx (1-T/2)$ has been used to yield the approximate form. As will be seen, this form makes the proceeding math much more tractable, and still closely agrees with the exact form.

3.2.3 Second Harmonic Generation in an Enhancement Cavity

Physically, transmission through cavity mirrors reduces the electric field within the cavity and is a loss mechanism. Besides the input coupler, an ideal enhancement cavity would have $T_n = 0$ as the ideal high reflectivity mirrors would have zero transmission. Any deviation from this can be thought of as unwanted intracavity loss. There is no reason we cannot lump other losses into T_n, which lets us write Eq. 3.17b as

$$\beta = \frac{4T_o}{(T_o+\mathcal{L})^2}, \tag{3.18}$$

where $\mathcal{L}$ is a general loss term for all loss in the cavity besides the input coupler transmission. With this intuitive change, we can now factor second harmonic generation into this equation as a loss term. We can define the total loss as $\mathcal{L} = l + l_{shg}$ where l is all intracavity loss besides the IC transmission and second harmonic conversion. The second term, which accounts for loss from second harmonic conversion can be defined as $l_{shg} = \frac{P_{shg}}{P_{cav}}$, where P_{shg} is the second harmonic power generated. Using Eq. 3.2, we know that $P_{cav} = \sqrt{P_{shg}/\gamma}$. Using all of this we can transform Eq. 3.18 into a form that directly relates the second harmonic power generated to the enhancement cavity input power. This form is convenient as these are the easiest parameters to measure in a lab, i.e, what power goes in and what power comes out. There is no requirement to measure what is happening internally in the cavity.

$$\frac{\sqrt{P_{shg}/\gamma}}{P_o} = \frac{4T_o}{(T_o + l + \frac{P_{shg}}{P_{cav}})^2} \tag{3.19}$$

$$= \frac{4T_o}{(T_o + l + \sqrt{P_{shg}\gamma})^2}. \tag{3.20}$$

Although it is physically reverse of the process that we want, this equation can be solved easily for P_o as a function of P_{shg},

$$P_o = \frac{1}{4T_o\sqrt{\gamma}}\sqrt{P_{shg}}(T_o + l + \sqrt{P_{shg}\gamma})^2. \tag{3.21}$$

This form tells us the input power required to generate a certain second harmonic power. However, Eq. 3.21 assumes that all the input power is coupled into the cavity and that all the second harmonic radiation generated by the crystal exits the cavity. In reality, these assumptions are not accurate. An optical cavity locked on resonance supports only specific transverse modes with a well-defined beam waist at all positions in the cavity. Therefore, the fundamental radiation should have high beam quality. As well, the beam size of the fundamental radiation coupled into the cavity should match the defined cavity mode and have the correct polarization for proper phase matching. This is the reason for the wave plate and lens before the ring cavity in Fig. 3.2. These parameters determine mode matching into cavity, which we will refer to as $\mathcal{M}$. For $\mathcal{M} = 1$, all the input power is coupled into the cavity and Eq. 3.21 would be valid. However, for efficient cavities, $\mathcal{M}$ generally ranges from 70-90%, which can be accounted for by multiplying P_o on the LHS of Eq. 3.21 by $\mathcal{M}$. Concerning the output of SH radiation, the mirrors in an enhancement cavity for SHG are designed for high reflectivity at the fundamental wavelength, since this is the radiation that must be built up. However, output coupling the SH radiation requires a dichroic element that is highly transmissive at the fundamental wavelength and highly reflective at the SH wavelength, or vice versa. In Fig. 3.2, we use the latter as one of the curved mirrors is dichroic. Furthermore, the

non-linear crystal must have an AR-coating at both wavelengths to combat Fresnel reflections on the faces of the crystal. Or, as in our case, if AR coatings aren't viable, the crystal can be Brewster cut to eliminate reflections off the faces for the fundamental wavelength, but this results in Fresnel reflection loss for the SH radiation when it exits the crystal. Overall, all these output coupling effects result in loss of the SH radiation, such that SH radiation measured outside the cavity is less than what theory predicts would be generated directly by the crystal. We will call this parameter $\mathcal{OC}$, and for $\mathcal{OC} = 1$, all the SH radiation generated by the nonlinear crystal is coupled out of the cavity. Factoring mode matching and output coupling into Eq. 3.21, we get the more realistic form

$$\mathcal{M}P_o = \frac{1}{4T_o\sqrt{\gamma}}\sqrt{\frac{P_{shg}}{\mathcal{OC}}}\left(T_o + l + \sqrt{\frac{P_{shg}\gamma}{\mathcal{OC}}}\right)^2, \tag{3.22}$$

where, reiterating, P_o is the fundamental power before it is coupled into the cavity and P_{shg} is the second harmonic power measured after exiting the cavity, as these are the common values measured in the laboratory.

This new form of second harmonic conversion in an enhancement cavity now has five parameters that determine the conversion efficiency of P_o to P_{shg}: $\mathcal{M}, \mathcal{OC}, \gamma, l, T_o$. So far, how the first four parameters impact the performance is clear: larger γ, $\mathcal{M}$, and $\mathcal{OC}$ will lead to higher conversion, as will decreasing l. How the last parameter, the input coupler transmission T_o, impacts the performance requires a consideration of impedance matching. For a perfectly impedance matched cavity with $\mathcal{M} = 1$, there would be no reflected power off the IC. This condition is met when the input coupler tranmission equals the total losses in the system, $T_o = \mathcal{L}$. The exact form for this expression in the case of second harmonic generation in an external resonator is given in [129] as

$$T_o^{opt} = \frac{l}{2} + \sqrt{\frac{l^2}{4} + \gamma P_o}. \tag{3.23}$$

From Eq. 3.23, we see that as second harmonic generation increases through increased P_o, so must the T_o^{opt}. This is an important consideration when designing high power second harmonic generation cavities.

As imperfect mode matching also leads to power reflected from the IC, in practice it is difficult to separate these two effects by simply measuring the reflected power. However, if P_o and P_{shg} are known, then we can calculate how much of this reflected power is from imperfect impedance matching. Using Eqs. 3.16-3.20, we see that

$$P_{leak} = P_{cav}T_o \tag{3.24a}$$

$$= \beta P_o T_o \tag{3.24b}$$

$$= \frac{4T_o^2 P_o}{(T_o + l + \sqrt{P_{shg}\gamma})^2}, \tag{3.24c}$$

where P_{leak} is the built up intracavity power that is transmitted through the input coupler. The fundamental power reflected off the input coupler is simply $P_{ref} = P_o(1-T_o)$. For a cavity locked on resonance, the leaked and reflected fields will be 180° out of phase, therefore the actual reflected power off the IC due to impedance matching, P_{IM} is

$$P_{IM} = (\sqrt{P_{leak}} - \sqrt{P_{ref}})^2 \tag{3.25a}$$

$$= \left(\sqrt{\frac{4T_o^2 P_o}{(T_o + l + \sqrt{P_{shg}\gamma})^2}} - \sqrt{P_o(1-T_o)}\right)^2. \tag{3.25b}$$

From Eq. 3.25b, it is possible to quantify the impedance matching of a second harmonic enhancement cavity purely based on the fundamental input power and outcoupled SH power. This is useful to distinguish between imperfect impedance matching and mode matching.

Putting all these results together, we can use Eq. 3.22 and generate a plot of second harmonic power generated by a non-linear crystal in an external resonator for a given fundamental input

power (see Fig. 3.3). Using Eq. 3.23, we can compare this performance for optimal and non-optimal input couplers, as well as compare the results for SHG to the exact form given by Eq. 3.17a. Lastly, we can quantify the impedance mismatching caused by non-optimal input coupler trasmission values using Eq. 3.25b (see Fig. 3.4). Both Fig. 3.3 and Fig. 3.4 use $M = OC = 0.8$, $l = 0.01$, $\gamma = 10^{-4}$ W^{-1}, which are representative of realistic values. From 3.23, this gives $T_o^{opt} = 0.037$ at the maximum value of input fundamental power, $P_o = 10$ W. As seen in 3.3, at low powers, the $T_o = 0.01$ outperforms the larger IC value as expected, but as the power increases the larger transmission IC starts to greatly outperform the lower IC value. This is supported by the impedance mismatched power versus fundamental input power for each IC shown in Fig. 3.4. As fundamental input power increases, the impedance mismatched power rapidly grows for $T_o = 0.01$ but decreases for $T_o^{opt} = 0.037$. Lastly, we see in Fig. 3.3, that the approximation going from Eq. 3.17a to Eq. 3.17b has negligible impact on the results as the theory derived without making this approximation overlaps the approximate theory very well.

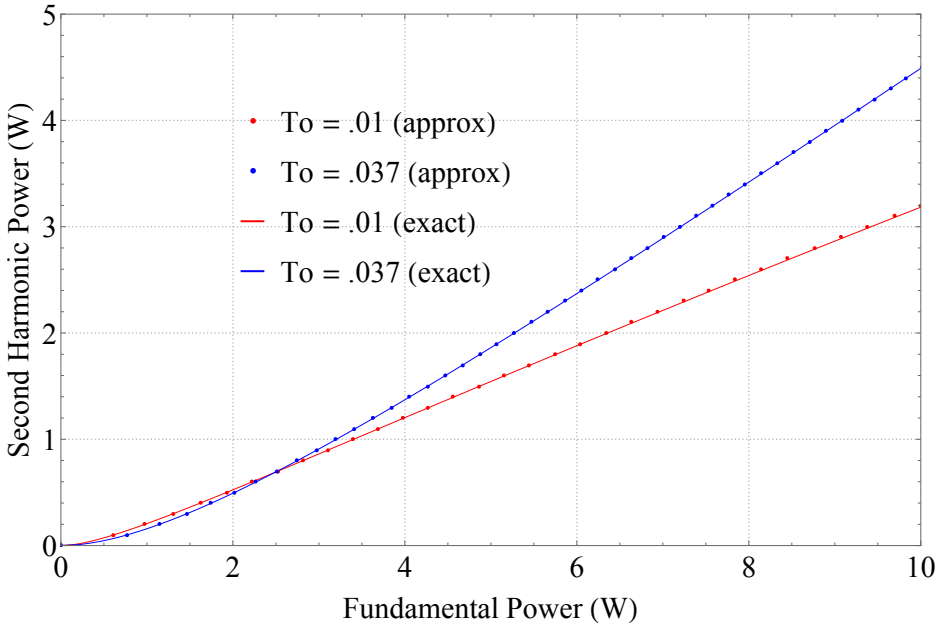

Figure 3.3: Second harmonic power versus fundamental input power in an external resonator for optimal and non-optimal input coupler values. For these plots, $M = OC = 0.8$, $l = 0.01$, $\gamma = 10^{-4}$ W^{-1}. The exact plots are generated without making the approximation going from Eq. 3.17a to Eq. 3.17b. The approximate plots are generated using Eq. 3.22, and the optimal input coupler of $T_o^{opt} = 0.037$ calculated using Eq. 3.23 for these parameters with $P_o = 10$ W.

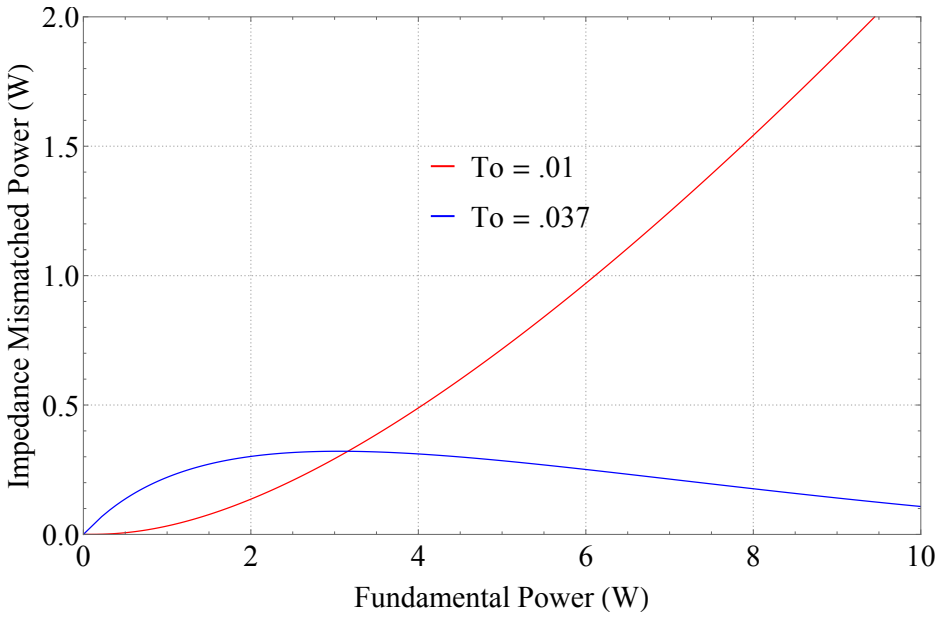

Figure 3.4: Impedance mismatched power versus fundamental input power for optimal and non-optimal input coupler values. These plots were generated using Eq. 3.25b for $M = OC = 0.8$, $l = 0.01$, $\gamma = 10^{-4}$ W^{-1}, where $T_o^{opt} = 0.037$ was calculated using Eq. 3.23 for these parameters with $P_o = 10$ W.

The analysis and results presented here were used to understand the SHG performance of our resonant bowtie doubling cavities presented in the following sections. However, before these results are presented, it also important to understand the physical design of the bowtie cavity shown in Fig. 3.2. This can be done using ABCD matrix analysis.

3.2.4 ABCD Matrix Analysis of Bowtie Cavity with Brewster-cut Non-linear Crystal and Internal Focus

We have seen that the beam size within a non-linear crystal impacts SH conversion, and that a focus is necessary to reach the high intensities for efficient conversion. The correct focus in the crystal requires a specific mirror radius of curvature and separation between these mirrors. Furthermore, proper mode matching in the cavity requires knowledge of the beam size in the remainder of the cavity. The curved mirrors required to create a focus in the non-linear crystal as well as Brewster elements introduce astigmatism, which complicates this calculation and can limit

the performance of the SHG process. All of these factors can be addressed using the right bowtie cavity geometry and dimension, which can be determined by application of the ABCD law.

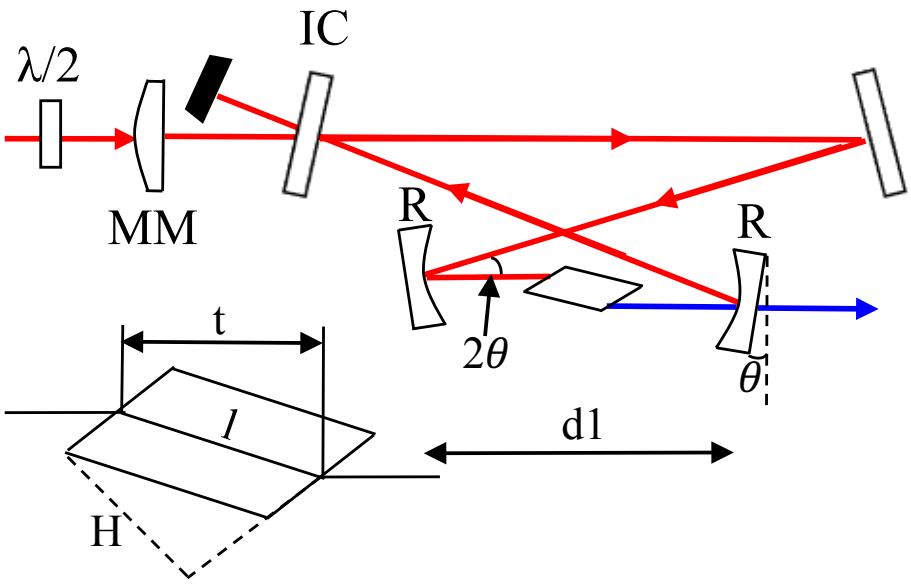

Figure 3.5: ABCD analysis of bow tie cavity with curved mirrors and Brewster elements. The curved mirrors have a separation of $d1$, the curved mirrors a radius of curvature R, and folding angle of 2θ, where θ is the incident angle of the curved mirrors. The total length of the cavity is $L = d2 + d1$, where $d2$ is the propagation distance from the dichroic curved mirror back to the first curved mirror. The parameters t,l, and H are common ways to define the dimensions of a Brewster element, and their relations are described in the text.

The bow tie cavity design that we will analyze using the ABCD law is shown in Fig. 3.5. Assuming that the characteristic cavity modes are Hermite-Gaussian that repeat their shape and phase after one round trip through the cavity requires that the complex beam parameter, q, satisfies [130]

$$q(z_1 + roundtrip) = q(z_1), \tag{3.26}$$

where

$$\frac{1}{q(z_1)} = \frac{1}{R(z)} - i\,\frac{\lambda}{\pi n w^2(z)}, \tag{3.27}$$

where $R(z) = z\big(1 + \big(z_o/z\big)^2\big)$ is the radius of curvature of the Gaussian wavefront, $z_o = \pi n w_o^2/\lambda$ is the Rayleigh length, and $w^2(z) = w_o^2\big(1 + \big(z/z_o\big)^2\big)$ is the beam waist. Using the ABCD law and the requirement set by Eq. 3.26 gives

$$q(z_1) = \frac{Aq(z_1) + B}{Cq(z_q) + D}, \tag{3.28}$$

where A, B, C, D are the components of the ray transfer matrix representing one round trip through the cavity. Solving for $1/q(z_1)$ gives

$$\frac{1}{q(z_1)} = \frac{-A - D}{2B} - i\,\frac{\big[1 - \big(\frac{A+D}{2}\big)^2\big]^{1/2}}{B}. \tag{3.29}$$

From Eq. 3.27, we see that the beam waist is

$$w^2(z_1) = \frac{\lambda B}{n\pi\big[1 - \big(\frac{A+D}{2}\big)^2\big]^{1/2}}. \tag{3.30}$$

The ray transfer matrix for one complete round trip that contains A, B, C, D in Eq. 3.30 is a product of each individual ray transfer matrix composing one complete round trip. The necessary individual ABCD ray transfer matrices are defined below:

$$\text{free space:} \quad \mathcal{M}_{fs}(z) = \begin{bmatrix} 1 & z \\ 0 & 1 \end{bmatrix} \tag{3.31a}$$

$$\text{Curved Mirror Horizontal:} \quad \mathcal{M}_{mh}(R,\theta) = \begin{bmatrix} 1 & 0 \\ -2/(R\cos\theta) & 1 \end{bmatrix} \tag{3.31b}$$

$$\tag{3.31c}$$

$$\text{Curved Mirror Vertical:} \quad \mathcal{M}_{mv}(R,\theta) = \begin{bmatrix} 1 & 0 \\ -2\cos\theta/R & 1 \end{bmatrix} \tag{3.32a}$$

$$\text{Brewster Horizontal:} \quad \mathcal{M}_{bh}(l,n) = \begin{bmatrix} 1 & l/(2n^3) \\ 0 & 1 \end{bmatrix} \tag{3.32b}$$

$$\text{Brewster Vertical:} \quad \mathcal{M}_{bv}(l,n) = \begin{bmatrix} 1 & l/(2n) \\ 0 & 1 \end{bmatrix} \quad , \tag{3.32c}$$

where n is the index of the crystal and l is the length along the light traveling direction in the Brewster element. For a Brewster cut crystal, this is simply the length of the crystal from face to face. Other ways Brewster elements are defined are by the thickness of the plate, H, which is related to l by $l = (n^2+1)^{1/2}H/n$. Another characterization is the spacing of the plate along the arm direction is $t = 2H/(n^2+1)^{1/2}$ [131]. The relation between l, H, and t are illustrated in Fig. 3.5.

Using Eqs. 3.31a-3.32c, we can determine the size of the beam at the center of the non-linear crystal, which determines the single pass conversion efficiency γ. The total ray transfer matrix in the horizontal would be:

$$\mathcal{M}_{tot} = \mathcal{M}_{bh}(\frac{l}{2}, n)\mathcal{M}_{fs}(\frac{d1-t}{2})\mathcal{M}_{mh}(R,\theta)\mathcal{M}_{fs}(d2)\mathcal{M}_{mh}(R,\theta)\mathcal{M}_{fs}(\frac{d1-t}{2})\mathcal{M}_{bh}(\frac{l}{2}, n). \tag{3.33}$$

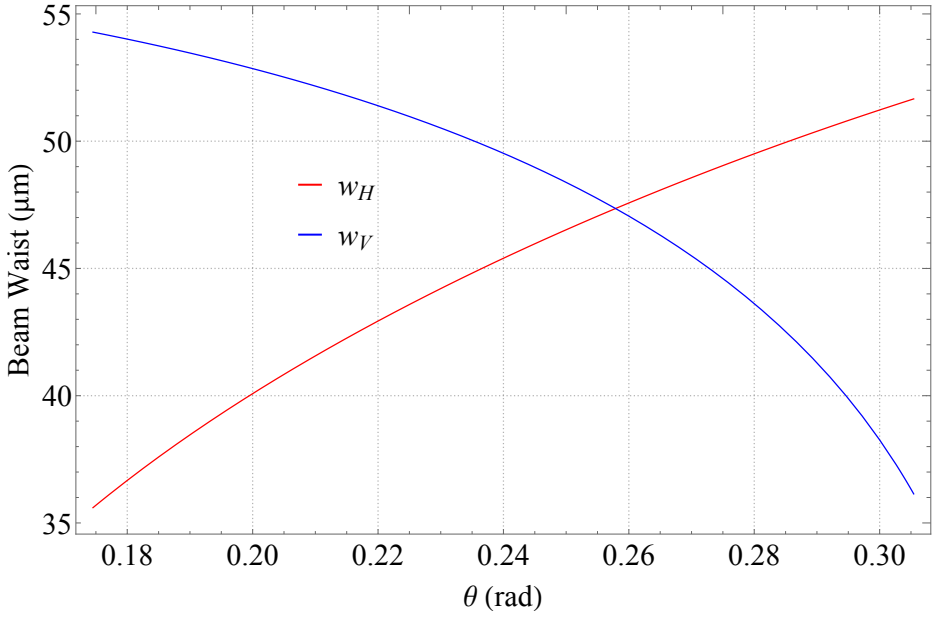

Figure 3.6: Folding angle versus horizontal and vertical focus in center of non-linear crystal. Using Eq. 3.33 for $d2 = 0.5$ m, $d1 = 0.165$ m, and $R = 0.15$ m, we see that $\theta \approx 0.26$ rad $= 14.9°$ minimizes astigmatism in the focus at the center of the non-linear crystal.

As seen in Fig. 3.6, using Eq. 3.33 we see that we can compensate for astigmatism in the focus at the center of the non-linear crystal by varying the folding angle of the bow tie cavity. While this angle reduces astigmatism in the center of the crystal, we see in Fig. 3.7 that a slightly smaller angle reduces astigmatism in the remainder of the cavity. Using a total ray matrix that repeats itself at a variable position between the dichroic curved mirror and the other curved mirror ($d2$), we can calculate the beam waist at all positions in the cavity excluding in between the curved mirrors. This analysis is useful for mode matching as it indicates the size of beam which should be coupled to the cavity.

With this, we now have the tools for designing a frequency doubling cavity, and from the previous sections the tools and knowledge on how to predict and optimize the performance of such a cavity. The next section proceeds with a description of our doubling cavities design and

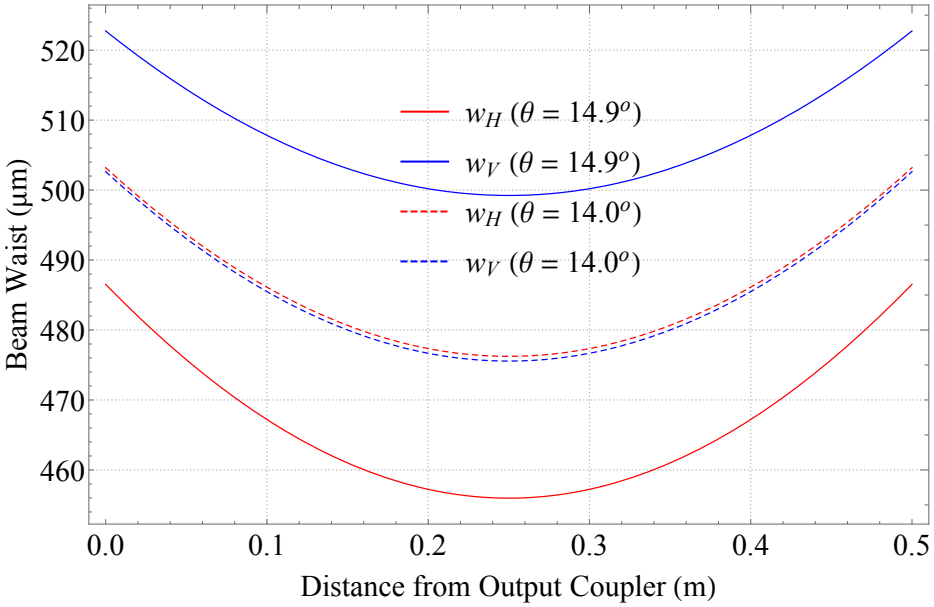

Figure 3.7: Beam waist at different positions in cavity for different folding angles. Using a total ray transfer matrix that repeats itself somewhere in between the longer separation between the curved mirrors for $d2 = 0.5$ m, $d1 = 0.165$ m, and $R = 0.15$ m, we see that $\theta \approx 0.245$ rad$= 14.0^\circ$ minimizes astigmatism in the long arm of the cavity.

performance, in which the analysis relies heavily on the theoretical framework developed in this section.

3.3 Frequency Doubling and Quadrupling Results

The 972.5 nm radiation generated by the Yb-fiber amplifier can be converted to 243.1 nm radiation through frequency quadrupling in two successive SHG enhancement cavities. As seen in Fig. 3.8, each of the cavities utilize Brewster crystals and the bow tie geometry modeled above.

Originally, when the Yb-fiber amplifier was operating at lower fundamental output power (see Section 2.4.4), the cavities were designed so that they would be robust for power scaling. This was done by increasing the size of the beam waist in each crystal to ≈ 2 times the optimal Boyd-Kleinman value, as well as choosing IC transmission values optimal for higher input powers. As will be seen, these decisions were well justified by the performance we saw when we power scaled the doubling stages using the higher IR output power (see Section 2.4.5).

As was done with the Yb-fiber performance, this section reviews the performance of these cavities with low power at 972.5 nm, followed by the power scaling performance and long term stability. Lastly, the precise frequency control of the 243.1 nm radiation is demonstrated by excitation of the 1S-2S transition in hydrogen.

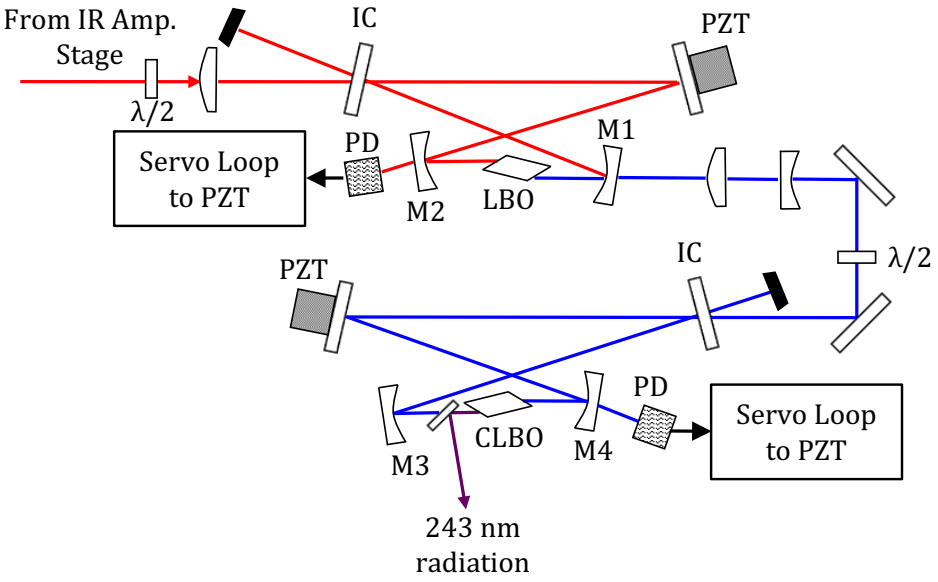

Figure 3.8: Frequency quadrupling through two successive SHG enhancement cavities. Each cavity uses a Brewster cut non-linear crystal (NLC) in a bow tie geometry. The first stage uses LBO as the NLC with curved mirrors M1 and M2 to generate the focus. Curved mirror M1 is dichroic and the 486.3 nm radiation is outcoupled through this mirror. The second stage uses CLBO as the NLC with mirrors M3 and M4 to generate the focus. A dichroic Brewster plate is used to outcouple the radiation. An EOM in the IR stage of the system generates sidebands for locking the cavities on resoance.

3.3.1 486.3 nm Generation

The first resonant doubling stage uses a 25 mm long LBO (lithium triborate LiB_3O_5) as the nonlinear crystal (Altechna or United Crystals). The indices of refraction for LBO have a strong sensitivity to temperature, which makes type-I non-critical phase matching, i.e., temperature phase-matching possible. This type of phase matching is advantageous as it eliminates spatial walk-off, enabling use of a longer crystal. Furthermore, this improves the output quality of the 486.3 nm radiation, which makes mode-matching into the following stage easier. However, at 972.5 nm, the

phase matching temperature in LBO is 283 °C [132]. This introduces technical challenges. The first is that performance of typical dual-wavelength anti-reflection coatings is not guaranteed at this temperature. Therefore, we must use a Brewster-cut crystal to minimize the reflection of the 972.5 nm radiation on the faces of the crystal. Unfortunately, this leads to an 18% loss of the 486.3 nm radiation as it exits the crystal due to Fresnel reflections. The second technical problem is building a crystal oven at the correct phase-matching temperature of 283 °C. At these high temperatures, metals like copper will oxidize and deposit a film on the face of crystal, severely degrading its performance. As well, the oven enclosure material could also bake off and deposit materials onto the crystal face. In the end, we use an aluminum crystal holder heated by a cartridge heater, with the crystal holder surrounded by calcium silicate as the insulator. The oven is mounted on a rotation stage to help align the crystal at Brewster's angle for the 972.5 nm radiation.

When first operating with the lower 972.5 nm power of $\approx$ 6 W, this doubling stage used 200 mm ROC mirrors that produced a $\approx$ 60 μm waist in the LBO crystal, and an IC with 3 % transmission. To keep the cavity on resonance, a fast piezo modulated one of the intracavity mirrors at $\approx$ 300 kHz. The modulated leakage light was detected by a photodiode (see Fig. 3.8), and was demodulated with a double-balanced mixer to generate an error signal. This signal was then sent to a loop filter followed by a fast ($\sim$ 50 kHz bandwidth) piezoelectric transducer and a slow ($\sim$ 100 Hz) transducer with greater range.

A plot of the generated SH power at 486.3 nm when this cavity was locked on resonance is shown in Fig. 3.9. With the maximum Yb-fiber output power of 6.3 W we could generate 2.4 W of radiation at 486.3 nm. The theoretical fit follows Eq. 3.22 with $T_o = 0.03$,$M = OC = 0.8$, $l = 0.006$, and $\gamma = 4.8 \times 10^{-5}$ W^{-1}. For these parameters, Eq. 3.23 predicts that $T_o^{opt} \approx 0.02$, and as seen by the black line in 3.9, this would yield a marginal improvement in output power. However, the IC transmission was chosen to be larger to reach impedance matching at higher input powers, and as seen in Fig. 3.10, the 3% IC impedance mismatched power is decreasing past 6 W.

This is indeed what we saw with the power scaled Yb-fiber system capable of generating > 10 W of power 972.5 nm. As seen in Fig. 3.11, with 10.8 W of power at 972.5 nm, we are able

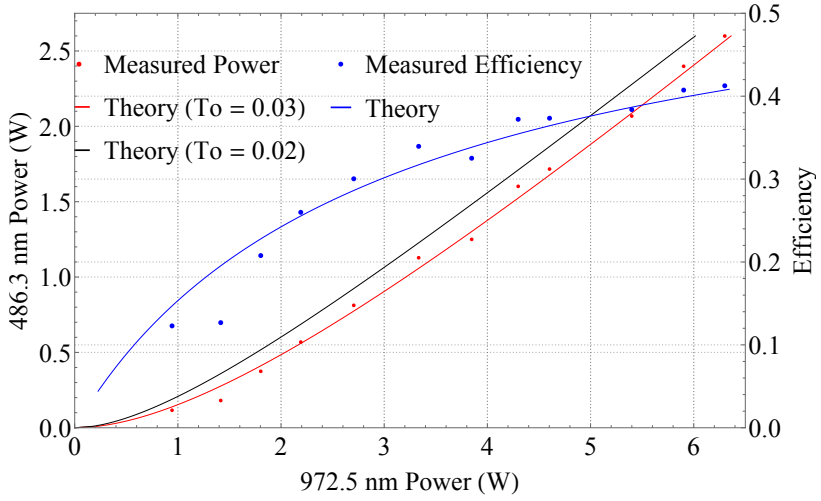

Figure 3.9: Frequency doubling Yb-fiber amplified 972.5 nm radiation to 486.3 nm radiation using LBO as the non-linear medium. The solid lines follow Eq. 3.22 for $M = OC = 0.8$, $l = 0.006$, and $\gamma = 4.8 \times 10^{-5}$ W^{-1}, where $T_o = 0.03$ is the experimentally used value of the IC and $T_o^{opt} = .02$ is the theoretical optimum.

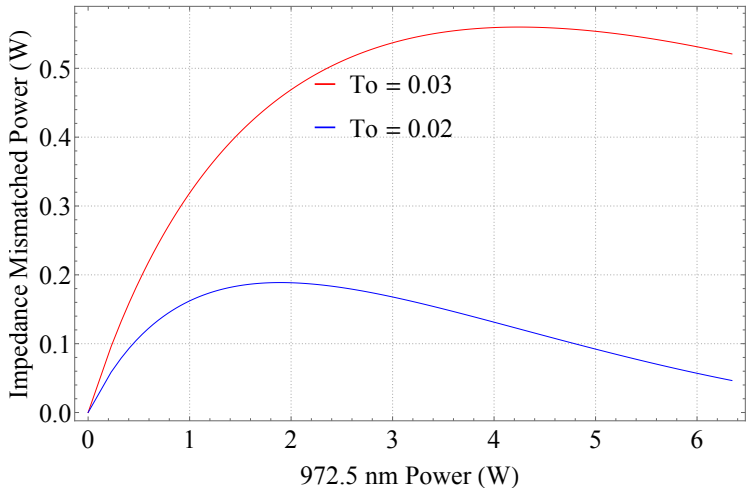

Figure 3.10: The impedance mismatching of Fig. 3.9 using Eq. 3.25b with $M = OC = 0.8$, $l = 0.006$, and $\gamma = 4.8 \times 10^{-5}$ W^{-1}, where $T_o = 0.03$ is the experimentally used value of the IC and $T_o^{opt} = .02$ is the theoretical optimum.

to obtain 4.2 W of 486.3 nm power. Again, the theoretical fits follows Eq. 3.22, and for this fit $M = OC = 0.7$, $l = 0.0.1$, $T_o = 0.03$, and $\gamma = 2.7 \times 10^{-4}$ W^{-1}. While $T_o^{opt} \approx 0.05$ for these parameters, we see that the difference in generated 486.3 nm power is negligible. However, as shown in Fig. 3.12, if the Yb-fiber is power scaled further, a 5% IC is preferable for impedance

matching as the impedance mismatching of the 3% IC is sharply increasing past 10 W of 972.5 nm power. From this knowledge of impedance mismatching, we can also extract information about the quality of the beam. The mode matching parameter for this fit is $M = 0.7$, which corresponds with the power we measured reflected off the input coupler, ≈ 30 % of the input power is reflected. From Fig. 3.12, we see that the reflected power from impedance mismatching is < 5% of the input power, so we can attribute the majority of this reflected power to imperfect mode matching. This imperfect mode matching could be from leftover ASE in the fiber amplifier, imperfect beam size or polarization. To figure this out, we measured the optical power and spectrum of ASE emitted from the Yb-fiber amplifier by looking at power reflected off a laser line filter at 972.5 nm. From this, we determined that less than 2 % of the power emitted directly from the Yb-fiber amplifier is ASE, which is attenuated further before frequency doubling from the laser line filter. Therefore, we can attribute the imperfect mode matching to improper beam size and polarization. Further investigations should try to differentiate between these two factors. Nonetheless, coupling 70 % of the power from a high-power fiber amplifier into a resonant cavity that supports only a single TEM00 mode when locked is indicative of a fairly high beam quality.

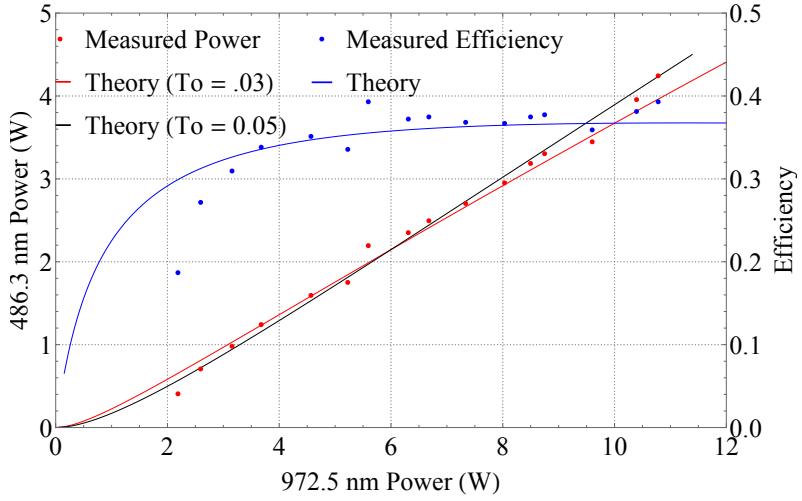

Figure 3.11: Frequency doubling Yb-fiber amplified 972.5 nm radiation to 486.3 nm radiation using LBO as the non-linear medium. The solid lines follow Eq. 3.22 for $M = OC = 0.7$, $l = 0.0.1$, $\gamma = 2.7 \times 10^{-4}$ W^{-1}, where $T_o = 0.03$ is the experimentally used value of the IC and $T_o^{opt} = 0.05$ is the theoretical optimum.

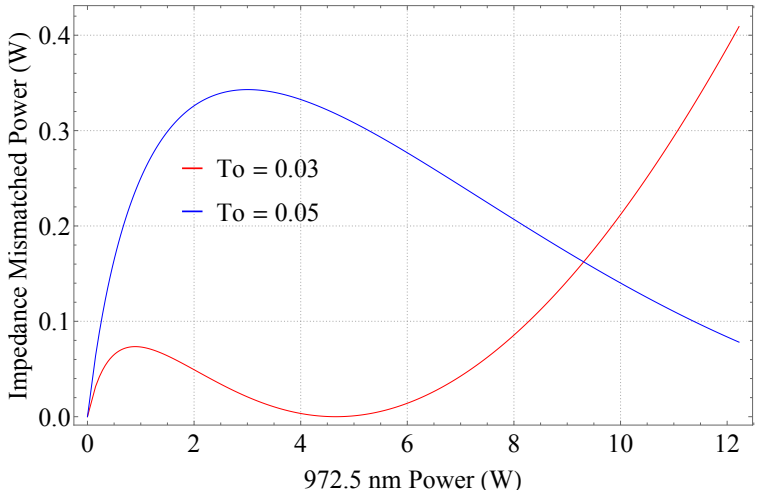

Figure 3.12: The impedance mismatching of Fig. 3.11 using Eq. 3.25b with $M = OC = 0.7$, $l = 0.0.1$, $\gamma = 2.7 \times 10^{-4}$ W^{-1}, where $T_o = 0.03$ is the experimentally used value of the IC and $T_o^{opt} = 0.05$ is the theoretical optimum.

There are a few notable differences between the LBO cavity design when operating with the pre and post power-scaled Yb-fiber amplifier. First, for the post power-scaled system, we modified the locking scheme such that both the LBO cavity and CLBO cavity would have the same modulation. This was done using an EOM in the IR stage of the laser, that generated sidebands at 3.8 MHz. As with the pre power-scaled system, this modulation was detected with a photodiode, demodulated to make an error signal and then sent to a servo loop and a slow and fast PZT in the cavity to maintain it on resonance. The other notable difference is in the model's determination of the single-pass conversion efficiency, γ. For the pre power-scaled system, $\gamma_{pre} = 4.8 \times 10^{-5}$ W^{-1}, whereas for the post power-scaled system, $\gamma_{post} = 2.7 \times 10^{-4}$ W^{-1}. The theoretical value, assuming no phase mismatch, for the beam waists used is $\approx 3 \times 10^{-4}$ W^{-1}, which matches the second cavity design. We believe this is explainable due to the fact that we used 150 mm ROC mirrors instead of 200 mm ROC mirrors in the later design, resulting in a tighter beam waist in the crystal of ≈ 50 μm beam waist versus 60 μm. However, the reasoning is not what one might initially expect. While decreasing the beam waist from 60 μm to 50 μm increases the single pass conversion efficiency, it only does so by ≈ 20 %, whereas the fits show a factor of five increase. We believe that the tighter

focus caused this increase by improving the temperature phase matching. Temperature gradients across the crystal degrade the phase matching condition, which γ is highly sensitive to. For a tighter focus, this condition will be less sensitive to temperature gradients.

While these high output powers are impressive, it is important that they are reliable and stable. To demonstrate this, we took long term measurements of the output of the 486.3 nm radiation, and could generate > 1 hour of continuous high power operation at 486.3 nm as shown in Fig. 3.13.

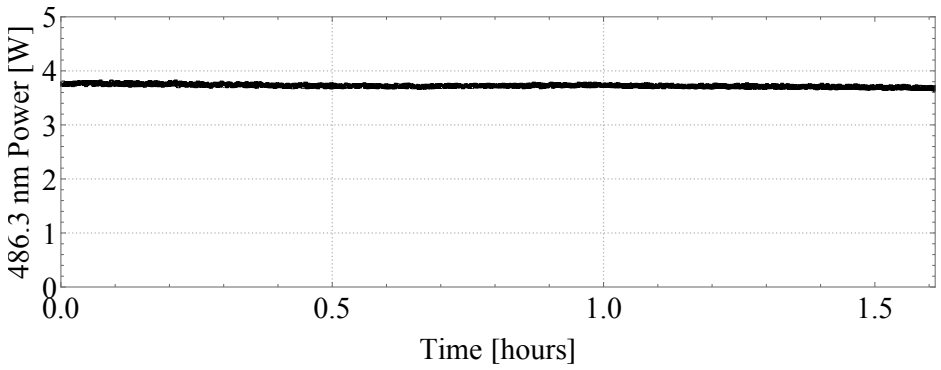

Figure 3.13: With the LBO doubling stage locked on resonance, ≈ 4 W of highly stable 486.3 nm radiation could be maintained continuously for greater than one hour.

Reaching this point of reliability and stability with the LBO cavity and crystal, as with the fiber polishing process, took significant trial and error. First, as mentioned in 2.4.5, operating at high IR powers required significant thermal management of the Yb-fiber output as coupling to the LBO cavity is highly sensitive to slight movement of the Yb-fiber tip. In regards to the crystal, most of the issues were a result of the oven. As mentioned, the oven was technically challenging to build as it needed to house the LBO crystal at 283° C. We originally used copper to heat the crystal, but the copper oxidized, depositing a film on the surface of the crystal. We then switched to aluminum, which did not oxidize. However, the crystal performance would still degrade over long time scales, and when examined, the crystal face still had a thin film on the face. We weren't sure what this film was from, but noticed the performance of the crystal was heavily dependent on the humidity in the lab. When the humidity was higher, the LBO cavity performed worse. Therefore, we invested in dehumidifiers for the lab. We also keep the crystal at an elevated temperature of 150° when the

laser is turned off, and purge the crystal continually with dry nitrogen. With these changes, the crystal reliability has been much more consistent.

3.3.2 243.1 nm Generation

The 486.3 nm radiation is coupled into the second resonant doubling stage to generate 243.1 nm radiation. This cavity uses a 10 mm long CLBO (cesium lithium borate $CsLiB_6O_{12}$ from Oxide) crystal as the non-linear crystal in a bow-tie configuration. While temperature phase matching is possible, the temperatures required are below 0 °C [133] and not practical for our application. We instead use type-I critical phase matching, i.e., angle phase matching. However, since CLBO is hygroscopic, the crystal is kept at 150 °C in an oven with a dry nitrogen purge. As with LBO, we use a Brewster-cut crystal at the fundamental wavelength of 486.3 nm as dual wavelength AR coatings are not available for the high power deep-UV radiation generated. This results in an 18 % Fresnel reflection loss of the 243.1 nm radiation as it exits the face of the crystal. A Brewster oriented dichroic plate that is highly transmissve at 486.3 nm and higly reflective at 243.1 nm is used to outcouple the 243.1 nm radiation (see Fig. 3.8). The locking mechanism for maintaining the cavity on resonance follows the same methods used in the pre and post power scaled LBO cavity. The radius of curvature of the mirrors is 200 mm, which generates a 50 μm waist in the crystal, ≈ 2 times the optimal size. The same ROC was used in both the pre and post power scaled CLBO cavity. While a tighter focus could lead to more output power, the results presented show evidence of self-heating of the crystal at high powers, which suggest perhaps a larger beam waist is more preferable.

Since CLBO is a relatively new non-linear crystal for UV generation, we originally also tested BBO (β-barium borate, β-BaB_2O_4), another commonly used crystal for UV generation. Although it has a higher effective non-linear coefficent, it also has a greater walkoff angle. Furthermore, CLBO has shown more resistance to UV degradation. As seen in Figs. 3.14 and 3.15, for the pre-power scaled performance, the CLBO crystal outperformed the BBO crystal. With the 2.4 W of 486.3 nm power, the BBO generated only 300 mW of 243.1 nm radiation compared to the CLBO's

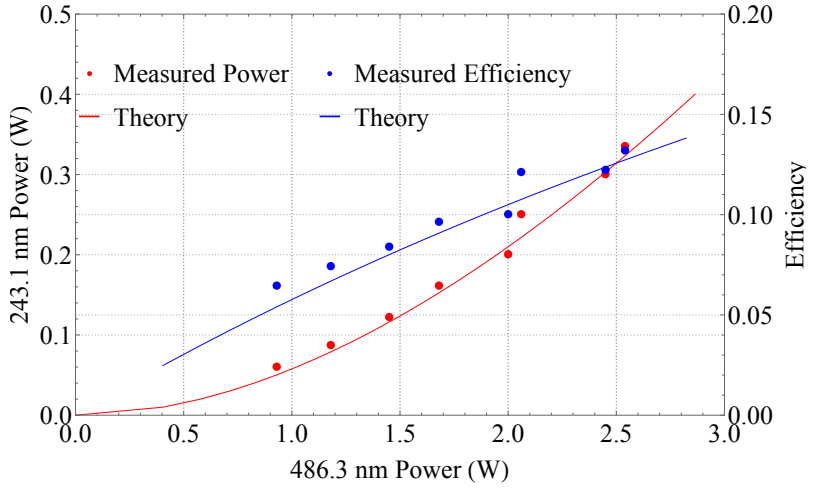

Figure 3.14: Frequency doubling 486.3 nm radiation to 243.1 nm radiation using BBO as the non-linear medium. The solid lines follow Eq. 3.22 for $M = OC = 0.8$, $l = 0.007$, $T_o = 0.05$, and $\gamma = 3.2 \times 10^{-5}$ W^{-1}.

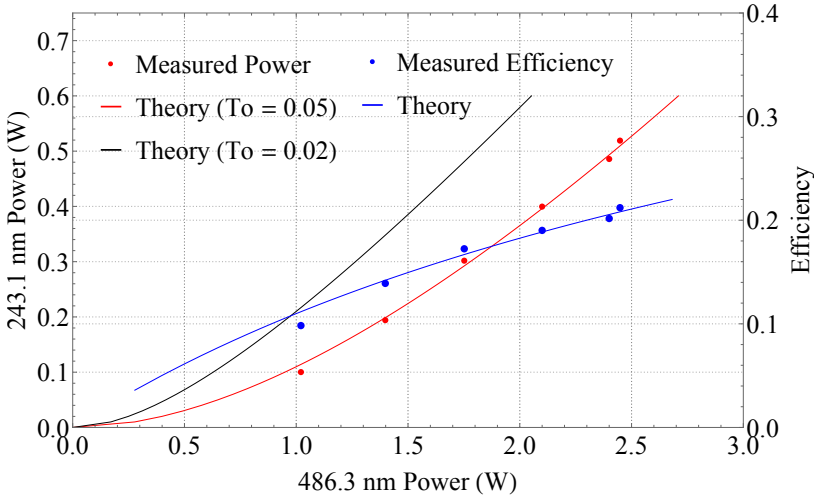

Figure 3.15: Frequency doubling 486.3 nm radiation to 243.1 nm radiation using CLBO as the non-linear medium. The solid lines follow Eq. 3.22 for $M = 0.8$, $OC = 0.74$, $l = 0.009$, and $\gamma = 8.6 \times 10^{-5}$ W^{-1}, where $T_o = 0.05$ is the experimentally used value of the IC and $T_o^{opt} = 0.02$ is the theoretical optimum.

530 mW. The fits again follow Eq. 3.22 for the following parameters. For BBO, $M = OC = 0.8$, $l = 0.007$, $T_o = 0.05$, and $\gamma = 3.2 \times 10^{-5}$ W^{-1}. For CLBO, $M = 0.8$, $OC = 0.74$, $l = 0.009$, $T_o = 0.05$, and $\gamma = 8.6 \times 10^{-5}$ W^{-1}. For these parameters, $T_o^{opt} = 0.02$, and as seen by the

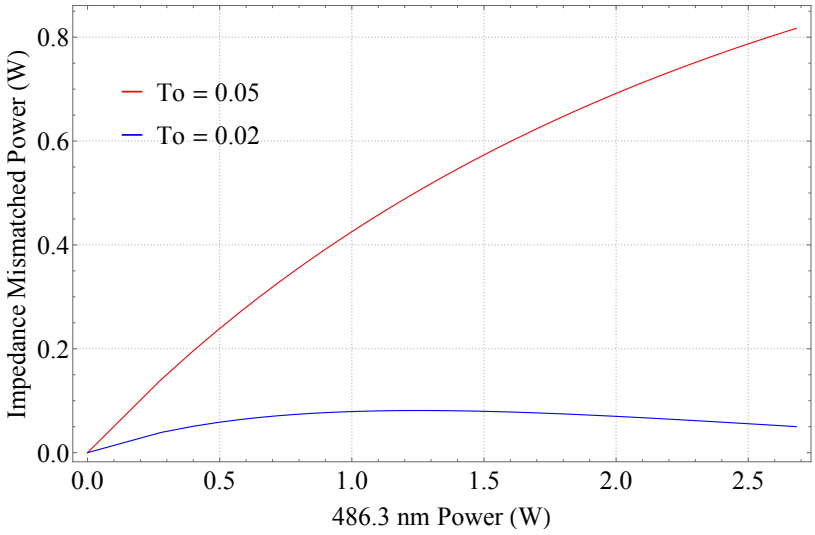

Figure 3.16: The impedance mismatching of Fig. 3.15 using Eq. 3.25b with $M = 0.8$, $OC = 0.74$, $l = 0.009$, and $\gamma = 8.6 \times 10^{-5}$ W^{-1}, where $T_o = 0.05$ is the experimentally used value of the IC and $T_o^{opt} = 0.02$ is the theoretical optimum.

black curve in Fig. 3.15 and the impedance mismatched power in Fig. 3.16, this would given significantly better performance as $T_o = 0.05$ is extremely overcoupled.

In the power scaled system, with > 4 W of 486.3 nm radiation we chose an IC with 2.5 % transmission and achieved much better impedance matching. As seen in Fig. 3.17, with 4.2 W of 486.3 nm radiation, we were able to generate up to 1.4 W of 243.1 nm power. The fit follows Eq. 3.22 for $M = 0.8$, $OC = 0.82$, $l = 0.015$, $T_o = 0.025$, and $\gamma = 1.6 \times 10^{-4}$ W^{-1}. For these parameters, $T_o^{opt} = 0.03$, and our generated power fits this theoretical optimal represented by the black curve very closely. This high quality of impedance matching is seen Fig. 3.18 with impedance mismatched powers of < 20 mW (< 0.5% of the fundamental power) for our chosen value of T_o. However, if more 486.3 nm power is available, a larger IC value would be preferable. Despite this high impedance matching, we measure 20% of the 486.3 nm power is reflected off the IC when the cavity is locked. Since the polarization from the LBO crystal is linear and well-defined, we attribute this to imperfect beam size, which should be investigated to improve mode matching into this cavity.

Due to the high UV power generated, UV-induced degradation of the CLBO crystal is a concern. While 5 W of 266 nm, 120 mW of 244 nm, and 140 mW of 198.5 nm CW radiation have

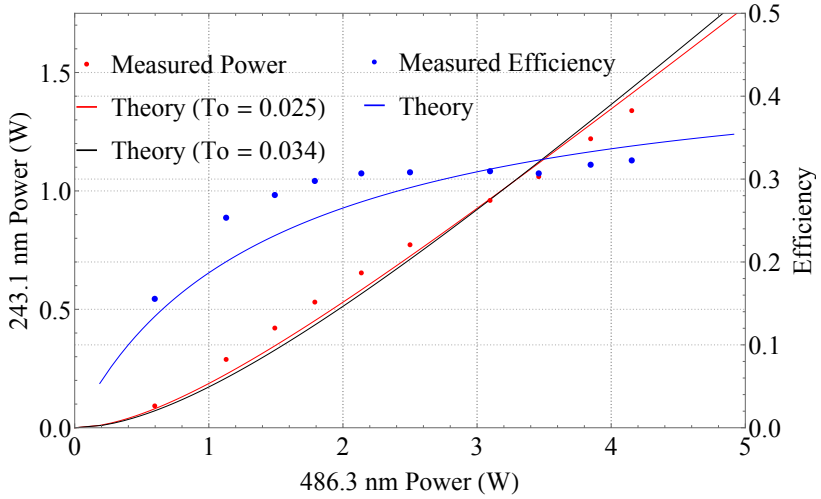

Figure 3.17: Frequency doubling 486.3 nm radiation to 243.1 nm radiation using CLBO as the non-linear medium. The solid lines follow Eq. 3.22 for $M = 0.8$, $OC = 0.82$, $l = 0.015$, and $\gamma = 1.6 \times 10^{-4}$ W^{-1}, where $T_o = 0.025$ is the experimentally used value of the IC and $T_o^{opt} = 0.03$ is the theoretical optimum.

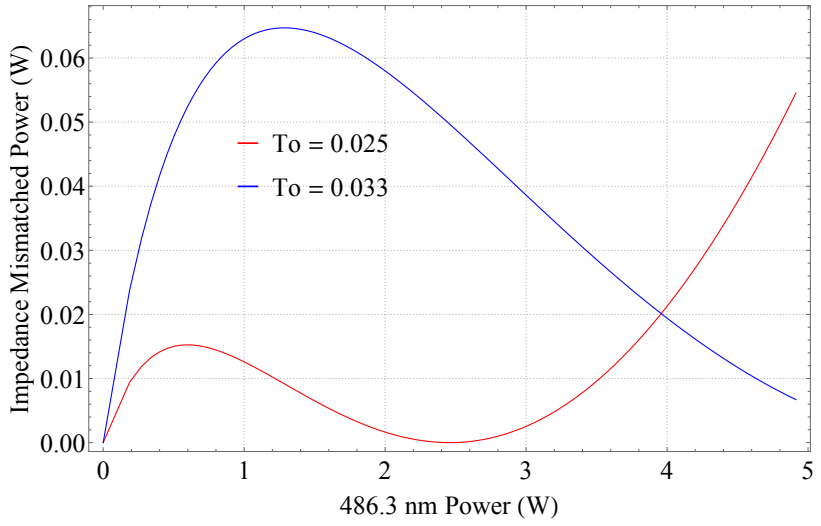

Figure 3.18: The impedance mismatching of Fig. 3.17 using Eq. 3.25b with $M = 0.8$, $OC = 0.82$, $l = 0.015$, and $\gamma = 1.6 \times 10^{-4}$ W^{-1}, where $T_o = 0.025$ is the experimentally used value of the IC and $T_o^{opt} = 0.03$ is the theoretical optimum.

been maintained for several hours using CLBO without evidence of degradation [134–136], studies observing degradation in CLBO on long time scales are limited and often restricted to pulsed laser systems. Using a 266 nm pulsed laser, it was shown that a UV-induced refractive index change can cause degradation in CLBO at peak power densities orders of magnitude lower than the bulk-induced damage threshold [137]. This degradation is evidenced by a decrease in UV transmittance

of the crystal over time, with a rate that increases with UV peak power density. Therefore, we use a beam waist ≈ 2 times larger than the optimal Boyd-Kleinman parameter in our CLBO crystal. With this, we have generated more than 1 W of 243.1 nm radiation for a combined duration of more than 20 hours on the same spot of the crystal without signs of UV-induced degradation. Although our peak intensity is significantly less than the pulsed system used in [137], our CW intensity is comparable to the average intensities for which they saw degradation on a sub-hour timescale. While we did not observe degradation of the CLBO crystal, we have seen evidence of UV absorption in the crystal resulting in self-heating and harmonic phase mismatch. This was observed in the output 243.1 nm mode structure and power which would oscillate around the optimal phase-matching condition over a few second period. As the phase-matching angle is temperature dependent, varying the exact oven temperature gives a sensitive method for phase matching in addition to our coarser method using a rotation stage. We were able to mitigate this harmonic phase mismatch from self-heating through slight adjustments of the oven temperature (< 1 °C). While the system was capable of producing 1.4 W of output power at 243.1 nm stably over tens of minutes, the thermal stability improved if the output was derated to ≈ 75 % of the maximum output power. As shown in Fig. 3.19, we observed that we could maintain more than 1 W of 243.1 nm for over 1 hour without observing this instability due to self-heating.

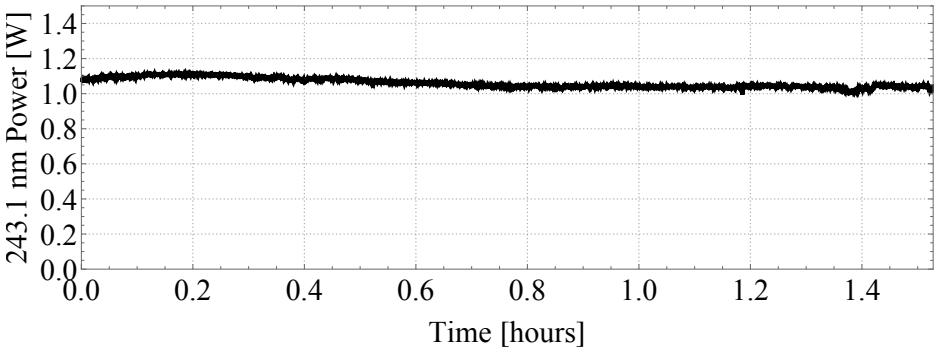

Figure 3.19: With the CLBO doubling stage locked on resonance, ≈ 1.5 W of highly stable 243.1 nm radiation could be maintained continuously for greater than one hour.

As a demonstration of the absolute frequency control and stability of the UV light, we excited the 1*S*–2*S* transition in hydrogen. We used only a portion of the available power ($\approx$ 200 mW) and a beam waist of 80 μm. As shown in Fig. 3.20, this radiation was overlapped with a 50 K atomic hydrogen beam at an angle of 6°, exciting some population into the metastable state. These metastable atoms were then quenched by an electric field, and the emitted Lyman-α photons were counted by a channel electron multiplier. The recovered 1*S*–2*S* lineshape is Gaussian, with a FWHM of 850 kHz, which is in excellent agreement with our estimate for transit-time broadening.

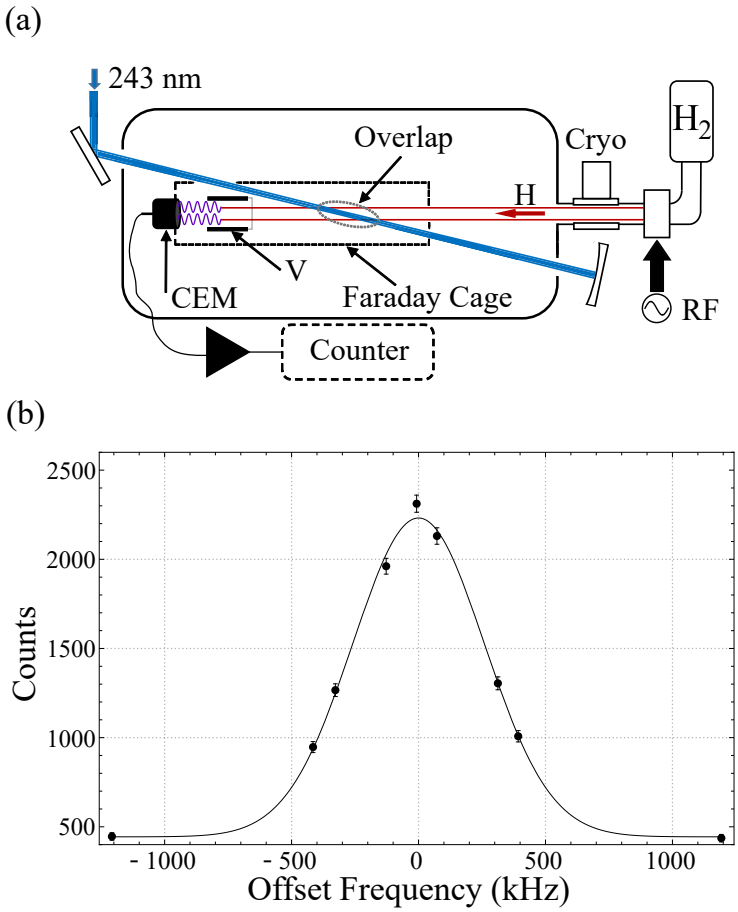

Figure 3.20: (a) Schematic of the hydrogen 1*S*–2*S* excitation. CEM: channel electron multiplier, V: quench electrodes, RF: microwave discharge, H_2: molecular hydrogen, Cryo: cryostat, Counter: frequency counter. The UV and atomic beam overlap in a Faraday cage to prevent quenching from stray fields. (b) Measured lineshape of the 1*S*–2*S* (F = 1 to F$'$ = 1) excitation.

This was a promising result for our group as the next two experiments planned, 2S-8D spectroscopy and two-photon laser cooling, rely on excitation of the 1S-2S transition.

3.4 Conclusion

In conclusion, we have demonstrated robust, high power frequency conversion from 972.5 nm to 486.3 nm, and subsequently, 486.3 nm to 243.1 nm with a frequency quadrupled Yb-fiber amplifier laser system. This system can generate > 4 W of 486.3 nm power and > 1 W 243.1 nm power in stable continuous operation for time periods greater than one hour. Lastly, we have demonstrated precise frequency control of the 243.1 nm radiation through excitation of the 1S-2S transition in hydrogen, critical for future experiments involving large populations of 2S metastable atoms and high 1S-2S scattering rates.

To the author's knowledge, this is the highest power, CW deep-UV laser below 266 nm, and builds onto significant, recent advances in frequency-quadrupled laser systems [138, 139]. While each doubling stage in our system utilizes common frequency doubling techniques, there are a few notable features of our design. The first is the conversion of a high-power Yb-fiber amplifier operating in the 3-level regime near the absorption/emission cross-section peak. While the development of high-power Yb-fiber amplifiers in this regime motivated by their subsequent use in efficient frequency conversion has attracted recent interest [46], to the author's knowledge, our system is the first to accomplish this. Another notable feature of our system is the use of CLBO for high-power, long-term deep-UV generation. While CLBO is gaining interest for deep-UV generation, its reliability at high powers and resistance to UV-induced degradation remains a question of interest. Hopefully our results can help shed light on some of these concerns.

For improving our frequency conversion, the first option would be generation of more IR power. The options for this were discussed in the conclusion of Chapter 2. Other methods to increase UV output power include increasing the efficiency of our doubling stages through improved mode matching and output coupling. For the LBO stage, the mode matching could be improved with more detailed studies of the mode quality and polarization of the Yb-fiber's amplified power. As

explained in section 3.3.1, these factors limit mode matching to the LBO cavity to ≈ 70 %. Furthermore, use of an AR coated LBO crystal that is angle phase matched instead of temperature phase matched would remove the 18 % Fresnel reflection loss. However, this would create walkoff, so calculations using the methods presented in section 3.2 should be done to determine the potential improvements with this method.

For the CLBO cavity, the mode matching is limited to 80 %, which is due to imperfect mode matching from improper input beam size. Careful ABCD matrix analysis should be done to determine better mode matching lenses for coupling into this cavity. While AR coatings aren't available to remove Fresnel reflections at the SH wavelength for CLBO, periodically poled crystals transparent in the UV, such as PP-LBGO, could remove walk-off. However, it is uncertain if periodically poled crystals can tolerate high-power operation.

Overall, the 243.1 nm power obtained in this system is impressive, but these powers have been achieved via cavity enhancement of less powerful 243.1 nm laser systems. Therefore, for this laser system to be useful in new ways for spectroscopy on hydrogen and hydrogen like atoms, as well as open doors to new regions of hydrogen experiments, the high powers obtained should enhanced further in a cavity. This is the focus of the next chapter: building a high-power, deep-UV enhancement cavity.

Chapter 4

Cavity-enhanced Deep-UV Laser

4.1 Introduction

In previous chapters, we have shown that frequency quadrupling of a high-power Yb-fiber amplifier at 972.5 nm can generate > 1 W of coherent, deep-UV radiation at 243.1 nm. For reference, the entire 243.1 nm laser system is shown in Fig. 4.1.

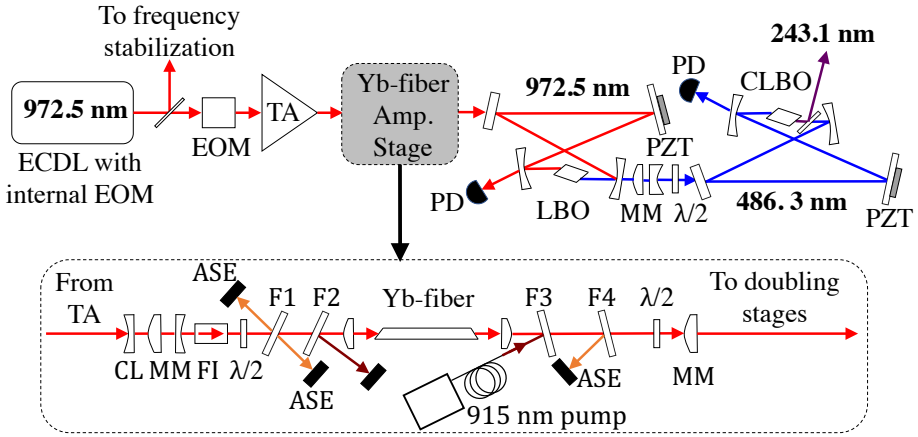

Figure 4.1: Design of the Yb-fiber amplifier and resonant doubling stages. The master oscillator at 972.5 nm is an extended cavity diode laser (ECDL). A small portion of the 972.5 nm light is used to actively stabilize the frequency of the oscillator. The light is then amplified through a tapered amplifier (TA) and Yb-doped fiber amplifier, followed by frequency quadrupling through successive resonant doubling stages. An electro-optic modulator (EOM) directly before the TA provides sidebands for cavity locking. PD: photodiode, PZT: piezo-electric transducer, MM: mode-matching lenses, $\lambda/2$: half-wave plate, CL: cylindrical lens, FI: Faraday isolator, ASE: amplified spontaneous emission, F1 & F4: laser-line filters at 972.5 nm, F2 & F3: longpass filters.

Before this laser system was developed, the only method to reach $\approx$ 1 W of 243.1 nm power was through cavity enhancement [17]. Cavity enhancement with $\approx$ 1 W of available input power therefore gives access to levels of 243.1 nm power that open new and exciting opportunities. These include significant statistical improvements in spectroscopy of exotic atoms where signals suffer

from low densities or numbers of excitable atoms. Besides increased statistics for spectroscopy, high intracavity 243.1 nm powers open up the possibility of two-photon laser cooling hydrogen.

While 243.1 nm cavities have operated at $\approx$ 1 W intracavity level, the intracavity powers possible through cavity enhancemet of 1 W of input power have not been demonstrated in the deep-UV. There are a number of difficulties associated with the operation of an enhancement cavity in this high power, deep-UV range. First, commercially available mirrors are only able to achieve $\approx$ 99.5 % reflectivity. Therefore, assuming perfect impedance matching and no losses, Eq. 3.17b indicates enhancement cannot be larger than 100. This is why such a high power 243.1 nm laser is needed to start with. Another difficulty is that short wavelength optics are known to degrade when exposed to high power radiation due to surface oxygen depletion [140] and hydrocarbon contamination [141]. While these effects can be mitigated in the UV and extreme UV by admitting O_2 onto the cavity mirrors, it introduces difficulties in maintaining the high vacuum needed for spectroscopy using the intracavity radiation.

In this chapter, a 243.1 nm enhancement cavity is presented. The chapter begins with a brief review of a two-level atom interacting with a laser. From this knowledge, the proposed two-photon cooling cycle and power necessary for laser cooling hydrogen can be understood. The chapter then discusses the required beam preparation for coupling our 243.1 nm laser system output into the enhancement cavity. Lastly, the 243.1 nm enhancement cavity is presented, which is capable of generating > 30 W of intracavity radiation at 243 nm with oxygen flushed mirrors. The results presented in this chapter have also been published in [142].

4.2 One and Two-photon Scattering of a Two-level Atom

The proposed two-photon cooling cycle for hydrogen is shown in Fig. 4.2 [23–26]. The hydrogen atoms are travelling in the + z direction with velocity v. In a linear UV enhancement cavity, which models our system, there will exist a co-propagating (+) and counter-propagating (-) 243.1 nm beam. An atom can absorb two photons from the (+) beam or (-) beam, as well as one from the (+) and (-) or vice versa, which will increase, decrease, or not change the velocity of the atoms

by $v_r = \hbar k_{l\alpha}/m = 3.3$ m/s, where v_r is referred to as the recoil velocity of the atom. Due to hydrogen's light mass, and energetic deep-UV wavelengths involved, hydrogen has a large recoil velocity that enables rapid cooling with modest scattering rates. By red-detuning the laser, the atoms will preferentially interact with the (-) beam, reducing their velocity in the z-direction since the recoils caused by spontaneous decays to the ground state are in random directions. A two-photon absorption will excite the hydrogen atom from the 1S to 2S state. Since the 2S state can only decay back to the 1S ground state through a two-photon decay, it is a metastable state, with a lifetime of $\tau_{2s} \approx 122$ ms. Therefore, the 2S state must be mixed with the much shorter lived 2P state with a $\tau_{2p} = 1.6$ ns lifetime, as it can spontaneously decay to the 1S ground state through numerous allowed single-photon transitions. This mixing of the 2S and 2P state is often called "quenching" the 2S state.

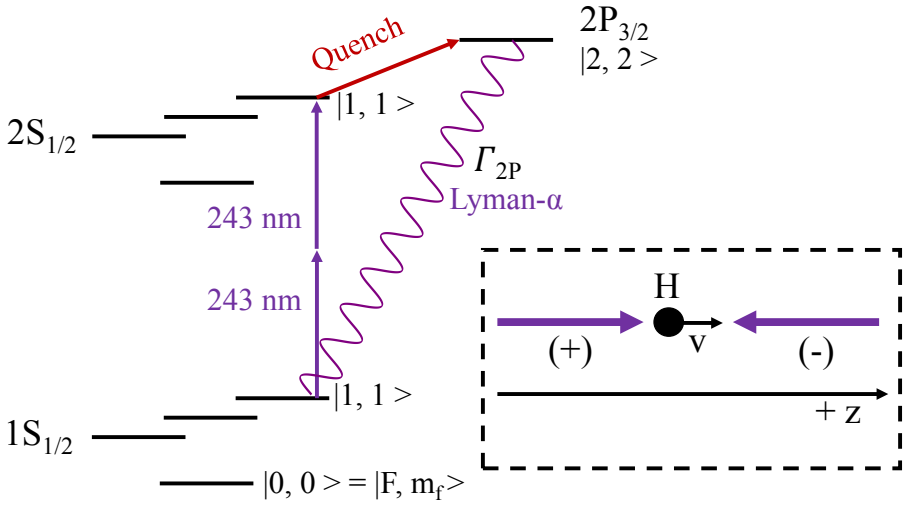

Figure 4.2: Two-photon cooling cycle for atomic hydrogen. Two-photon absorption of a 243.1 nm laser excites hydrogen from the 1S to 2S state. Due to the long lifetime of the 2S state, this state must be mixed with the 2P state so the atom can spontaneously decay back to the 1S state, completing the cooling cycle. Using the hyperfine stretched states in the 1S, 2S, and 2P levels of atomic hydrogen this cycle can be treated as a 3-level problem.

The presence of quenching can be accounted for by introducing an effective linewidth of the excited level [24], where $\Gamma_{2S} \ll \Gamma_{eff} < \Gamma_{2P}/2$, depending on the strength of the quenching field. The strong quenching limit effective linewidth of $\Gamma_{2P}/2$ makes sense as when maximally mixing

the 2S and 2P states, the atom will spend half the time in the 2P state. Effectively, we can think of this quenching as breaking the three levels involved in the two-photon cooling scheme into two, two-level processes. First, by understanding the mixing between the 2S and 2P state, we can determine an effective linewidth for the excited state. The requirement $\Gamma_{eff} \gg \Gamma_{2s}$ makes it valid to ignore the 1S state in this calculation. With this knowledge, we can then treat the two-photon cooling cycle as a simple two-level problem between the 1S state and effective excited state [24].

This section will begin by deriving the steady state scattering rate for a two-level atom with spontaneous decay from the excited state through the use of Optical Bloch equations. From this analytic form, the effective quenching can be calculated. Then, a brief overview of two-photon transitions will be given, and how the scattering rate equation can be modified to explain these processes. The goal is to determine the scattering rate between the 1S and effective excited state, Γ_{cool}, since the acceleration an atom experiences in a laser cooling beam is simply $a_{cool} = v_r \Gamma_{cooL}$.

We want to calculate the dynamics of a two-level atom interacting with a laser. We start with the time-dependent Schrödinger equation

$$\mathcal{H}(t)\Psi(\vec{r},t) = [\mathcal{H}_o + \mathcal{H}^{'}(t)]\Psi(\vec{r},t) = i\hbar\frac{d\Psi(\vec{r},t)}{dt}$$

where $\mathcal{H}_o$ is the field-free, time-independent Hamiltonian for the two-level atom, satisfying, $\mathcal{H}_o\phi_n(\vec{r}) = \hbar\omega_n\phi_n(\vec{r})$, and $\mathcal{H}^{'}(t)$ the Hamiltonian for the laser. For a two level atom with a ground state, g, and an excited state, e, we can write $\Psi(\vec{r},t)$ as

$$\Psi(\vec{r},t) = c_g(t)\phi_g(\vec{r})e^{-i\omega_g t} + c_e(t)\phi_e(\vec{r})e^{-i\omega_e t}$$

Using the orthonormality of ϕ_k, this gives:

$$i\hbar\frac{dc_g(t)}{dt} = c_e(t)\mathcal{H}'_{ge}(t)e^{-i\omega_a t} \tag{4.1}$$

$$i\hbar\frac{dc_e(t)}{dt} = c_g(t)\mathcal{H}'_{eg}(t)e^{i\omega_a t} \tag{4.2}$$

where $\mathcal{H}'_{jk}(t) = \langle\phi_j|\mathcal{H}'(t)|\phi_k\rangle$ is the time-dependent coupling between the two levels and $\omega_a = \omega_{eg} = (|E_e - E_g|)/\hbar$ is the resonance frequency of the atom. The laser's electric field interacts with the atoms, which gives $\mathcal{H}'(t) = -e\vec{\mathcal{E}}(\vec{r},t)\cdot\vec{r}$ where e is the elementary charge and for a plane wave traveling in the positive z-direction $\vec{\mathcal{E}}(\vec{r},t) = E_o\hat{\epsilon}\cos(kz - \omega_l t)$ where E_o is electric field amplitude of the laser field, $k = \omega_l/c$ where ω_l is the laser frequency, and $\hat{\epsilon}$ is the unit polarization vector. For a two-level atom, the dipole moment $e\vec{r}$ is parallel to $\hat{\epsilon}$; therefore, the laser coupling between the two levels becomes

$$\mathcal{H}'_{eg}(t) = \hbar\Omega cos(kz - \omega_l t)$$

where

$$\Omega = -\frac{E_o}{\hbar}\mu_{eg} \tag{4.3}$$

is the Rabi frequency and $\mu_{eg} = e\langle e|z|g\rangle$ for z-polarized radiation. Using the electric dipole approximation, we can neglect the spatial variation of the electric field as the wavelength of light (100's of nm) is much larger than the spatial extent of the wavefunction. This recasts the coupling element as

$$\mathcal{H}'_{eg}(t) = \frac{\hbar\Omega}{2}(e^{i\omega_l t} + e^{-i\omega_l t}) \tag{4.4}$$

Using Equation (4.1), and that $\mathcal{H}'_{eg}(t) = \mathcal{H}'_{ge}(t)$, since $\langle e|z|g\rangle = \langle g|z|e\rangle$ gives

$$i\hbar\dot{c_g} = \frac{\hbar\Omega}{2}c_e(e^{i\delta t} + e^{-i(\omega_l+\omega_a)t})$$

where $\delta = \omega_l - \omega_a$ is the detuning from the atomic resonance. We are generally interested in a system close to resonance, $(\omega_l + \omega_a) \gg \delta$. This let's us neglect fast oscillating terms like $(\omega_l + \omega_a)$. This is called the Rotating Wave Approximation (RWA). Therefore, we see that

$$\dot{c_g} = -\frac{i\Omega}{2}c_e e^{i\delta t} \tag{4.5}$$

$$\dot{c_e} = -\frac{i\Omega}{2}c_g e^{-i\delta t} \tag{4.6}$$

Physically, $|c_g|^2$ and $|c_e|^2$, represent the the percentage of the population in the ground and excited state, respectively, where $|c_g|^2 + |c_e|^2 = 1$. Therefore, the following change of variables doesn't physically change our system.

$$c_g^{'}(t) = c_g(t)$$

$$c_e^{'}(t) = c_e(t)e^{i\delta t}$$

However, this change of variables, which is algebraically equivalent to the rotating-frame transformation, removes time dependence from the solutions of Equations (4.5) and (4.6). Using these transformations, Equations (4.5) and (4.6) become

$$i\hbar\dot{c_g^{'}} = \frac{\hbar\Omega}{2}c_e^{'} \tag{4.7}$$

$$i\hbar\dot{c_e^{'}} = \frac{\hbar\Omega}{2}c_g^{'} - \hbar\delta c_e^{'} \tag{4.8}$$

In order to calculate the scattering rate at which the laser will interact with our two-level atom, we need to add spontaneous emission. This is commonly done by switching to density matrix formalism, with the density operator ρ described as:

$$\rho = |\Psi\rangle \langle\Psi|$$

We are close to deriving the Optical Bloch Equations. The good news is that we have already laid the framework with Equations (4.7) and (4.8). We can relate ρ to our c_i coefficients through

$$\rho_{ij} = \langle\phi_i|\rho|\phi_j\rangle = \langle\phi_i|\Psi\rangle \langle\Psi|\phi_j\rangle = c_i c_j^*$$

Therefore, for our two level atom in our "co-rotating" frame

$$\rho = \begin{pmatrix} \rho_{ee} & \rho_{eg} \\ \rho_{ge} & \rho_{gg} \end{pmatrix} = \begin{pmatrix} c_e^{'} c_e^{'*} & c_e^{'} c_g^{'*} \\ c_g^{'} c_e^{'*} & c_g^{'} c_g^{'*} \end{pmatrix}$$

where ρ_{gg} and ρ_{ee} are the populations in the ground and excited state, respectively, obeying $\rho_{gg} + \rho_{ee} = 1$. The other two terms ρ_{eg} and ρ_{ge} are the coherences between the excited and ground states. Through them, we can introduce the effects of spontaneous emission as an exponential decay of the coherences at a constant rate

$$\left(\frac{d\rho_{eg}}{dt}\right)_{spon} = -\frac{\Gamma}{2}\rho_{eg} \tag{4.9}$$

where Γ is the lifetime of the excited state. Using the chain rule

$$\frac{d\rho_{ij}}{dt} = \frac{dc_i^{'}}{dt}c_j^{'*} + c_i^{'}\frac{dc_j^{'*}}{dt} \tag{4.10}$$

and Equations (4.7,4.8) along with spontaneous emission through Equation (4.9) we can derive the Optical Bloch Equations:

$$\begin{aligned}
\dot{\rho}_{gg} &= \Gamma\rho_{ee} - \frac{i\Omega}{2}(\rho_{eg} - \rho_{ge}) \\
\dot{\rho}_{ee} &= -\Gamma\rho_{ee} + \frac{i\Omega}{2}(\rho_{eg} - \rho_{ge}) \\
\dot{\rho}_{eg} &= (i\delta - \frac{\Gamma}{2})\rho_{eg} + \frac{i\Omega}{2}(\rho_{ee} - \rho_{gg}) \\
\dot{\rho}_{ge} &= (-i\delta - \frac{\Gamma}{2})\rho_{ge} - \frac{i\Omega}{2}(\rho_{ee} - \rho_{gg})
\end{aligned}$$

Letting $w = \rho_{gg} - \rho_{ee} = 1 - 2\rho_{ee}$ define the population difference gives

$$\begin{aligned}
\frac{dw}{dt} = \frac{d\rho_{gg}}{dt} - \frac{d\rho_{ee}}{dt} &= 2\Gamma\rho_{ee} - i\Omega(\rho_{eg} - \rho_{ge}) \\
&= \Gamma(1 - w) - i\Omega(\rho_{eg} - \rho_{ge})
\end{aligned}$$

as well

$$\dot{\rho}_{eg} = (i\delta - \frac{\Gamma}{2})\rho_{eg} + \frac{iw\Omega}{2}$$

At steady-state, $\dot{w} = \dot{\rho}_{eg} = 0$. Using $\rho_{eg} = \rho_{ge}^*$ gives

$$\begin{aligned}
w &= \frac{1}{1+s} \\
\rho_{eg} &= \frac{i\Omega}{2(\Gamma/2 - i\delta)(1+s)}
\end{aligned}$$

where s is the saturation parameter defined as

$$s = \frac{|\Omega|^2}{2|\Gamma/2 - i\delta|^2} = \frac{\Omega^2/2}{\delta^2 + \Gamma^2/4} = \frac{s_o}{1 + (2\delta/\Gamma)^2}$$

where $s_o = 2|\Omega|^2/\Gamma^2$ is the on resonance saturation parameter. We see why s is called the saturation parameter. For large s, the population difference goes to zero, which physically means we have saturated the excited state. The scattering rate Γ_{scat} is simply the decay rate of the excited state times the population of the excited state; therefore,

$$\begin{aligned}
\Gamma_{scat} = \Gamma\rho_{ee} = \frac{1}{2}\Gamma(1 - w) &= \frac{\Gamma s}{2(1 + s)} \\
&= \left(\frac{s_o}{1 + s_o}\right)\left(\frac{\Gamma/2}{1 + (2\delta/\Gamma')^2}\right) \qquad (4.11) \\
&= \frac{\Gamma\Omega^2}{4\delta^2 + \Gamma^2 + 2\Omega^2} \qquad (4.12)
\end{aligned}$$

where $\Gamma' = \Gamma\sqrt{1 + s_0}$ is the power broadened linewidth of the transition. We see from Eq. 4.12, that when on resonance the scattering rate between two levels asymptotically approaches $\Gamma/2$ as Ω increases.

As explained earlier, we are interested in the effective quenching of the 2S and 2P, as this determines our effective linewidth of the excited state, i.e., Γ_{eff} is the scattering rate between the 2S and 2P states. By plotting Eq. 4.12 using $\Gamma = \Gamma_{2P} = 1/\tau_{2P}$, where $\tau_{2P} = 1.6$ ns, we can then determine the Rabi frequency necessary to maximally quench this transition. This plot is shown in Fig. 4.3, and we see that for $\Omega > 1.0 \times 10^9$ s^{-1}, the scattering rate is approaching $\Gamma_{2P}/2$. Using Eq. 4.3, this Rabi frequency corresponds to ~ 1 W/cm^2 of microwave power.

For one photon transitions, the Rabi-frequency is defined as $\Omega = -\frac{E_o}{\hbar}\mu_{eg}$, where for z-polarization $\mu_{eg} = e\langle e|z|g\rangle$ was the single-photon transition matrix element between the excited

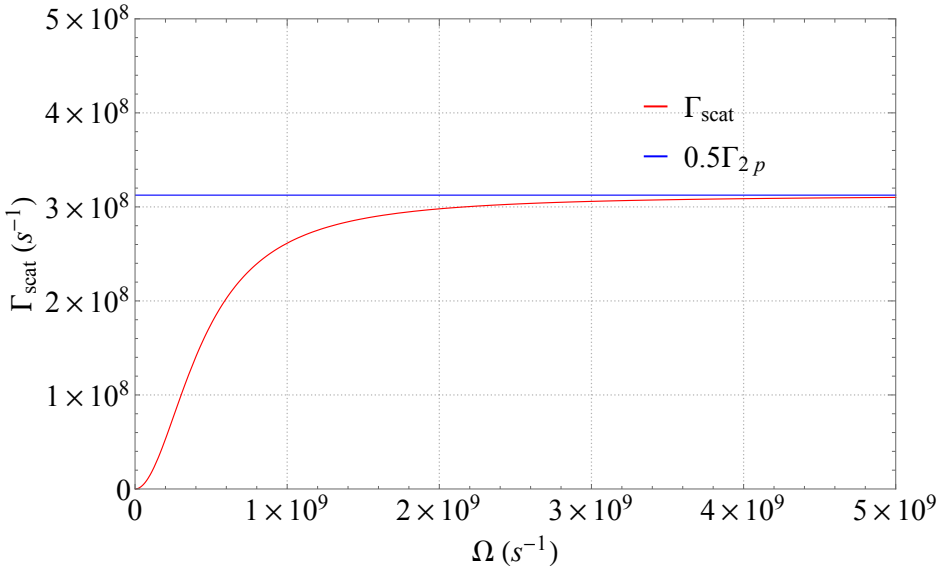

Figure 4.3: Quenching the 2S state via mixing with the 2P state. As the Rabi frequency of the quenching radiation increase, the scattering rate from the 2S to the 2P state reaches a maximum value of $\Gamma_{2P}/2$, which makes sense as the atom is equally like to be found in the 2S or 2P.

and ground state in hydrogen, whose wave functions are well known. For two-photon transitions, Ω is proportional to the intensity of the electric field and can be written as [27]

$$\Omega_{DF} = 4(2\pi\beta_{ge})\sqrt{I_{(+)}I_{(-)}} \tag{4.13}$$

$$\Omega_{NDF} = 2(2\pi\beta_{ge})I_{(+/-)}, \tag{4.14}$$

where DF and NDF stand for Doppler-Free and Non-Doppler-Free processes, and $I_{(+)}$, $I_{(-)}$, are the intensities of the co(+) or counter(-) propagating beam, and β_{ge} is the two-photon transition matrix element. As shown earlier in Fig. 4.2, for two-photon scattering processes, an atom can absorb two photons each from either the (+) or (-) beam, or one photon each from the (+) and (-) or vice versa. The first order Doppler shift is cancelled in this last process, and the DF Rabi frequency is a factor of 2 larger as there are two indistinguishable processes that could lead to a DF scatter. Determining the two-photon transition matrix element, β_{ge}, while more challenging than the single-photon transition matrix element required for the quenching process, can be reduced to

a series of single-photon transition matrix element calculations using second-order perturbation theory. Second-order perturbation is necessary since single-photon transitions from the 1S to the 2S are dipole-forbidden, and the only possible excitation paths are combinations of two or more dipole-allowed transitions that start in the 1S and end in the 2S state. For two photon processes, this can be written for z-polarized radiation as [27]:

$$\beta_{ge} = \frac{e^2}{2hc\epsilon_o} \sum_r \frac{\langle e|z|r\rangle \langle r|z|g\rangle}{(E_g + \hbar\omega_l) - E_r} \tag{4.15}$$

$$= -\frac{e^2}{2hc\epsilon_o} \langle e|z \frac{1}{H_o - (E_g + \omega_l)} z|g\rangle \,, \tag{4.16}$$

where ω_l is the angular frequency of the excitation laser, E_g is the energy of the ground state, E_r is the energy of the intermediate state, both of which follow $E_n = -\alpha^2 m_e c^2/2n^2$ with α being the fine structure constant. Lastly, $\sum_r |r\rangle \langle r| = 1$, as it is the complete set of discrete eigenstates of non-perturbed hydrogen with Hamilitonian H_o. At first glance, the first form in Eq. 4.15 appears straightforward to calculate since the unperturbed hydrogen eigenstates have well known analytic forms, along with easily calculable energies, E_n. Nonetheless, the summation over an infinite number of states poses challenges and there are numerous techniques to overcome this issue [143]. One method is to use a Green's function approach, which is the second form represented by Eq. 4.16. This method produces a more accurate answer as it is able to include the continuum states in the calculation, whereas Eq. 4.15 only sums over discrete states. Evaulation of Eq. 4.16 is done in [27]. Using this method they calculated β_{ge} for several two photon transitions from 1S-nS, 2S-nS, 1S-nD, and 2S-nD levels in hydrogen. In our case, we are interested in the 1S-2S, and the exact value using the Green's function approach is:

$$\beta_{ge}^{1S-2S} = 3.68 \times 10^{-5}\,\mathrm{Hz}(\mathrm{W/m^2})^{-1} \tag{4.17}$$

It is easy to check this value against the brute force method of summing up the overlap integrals in Eq. 4.15 since the normalized wavefunctions, $\psi_{nlm} = |nlm\rangle$, for hydrogen are well-known. Furthermore, for z-polarized light we only have to consider nP (l=1, m=0) states as these are the only dipole allowed transitions that can couple to S states (l=0, m=0) with z-polarization due to the one-photon transition selection rules, $\Delta l = 0, \pm 1$, $\Delta m = 0$. Therefore, for the 1S-2S two-photon transition, we can rewrite

$$\beta_{ge}^{1S-2S} = \frac{e^2}{2hc\epsilon_o} \sum_{n=1}^{\infty} \frac{\langle 200|z|n10\rangle \langle n10|z|100\rangle}{(E_g + \hbar\omega_l) - E_n}. \tag{4.18}$$

Using this method for n = 2 to n = 20 gives the result shown in Fig. 4.4. As seen, this method asympotically approaches a value for $\beta_{ge}^{1S-2S} \approx 4.2 \times 10^{-5}\,\mathrm{Hz(W/m^2)^{-1}}$, which is ≈ 14 % larger than the exact value using the fully analytical Green's function method. This difference is reasonable as similar sums without [144] and with [145] the continuum in hydrogen can yield results that differ by a factor of two.

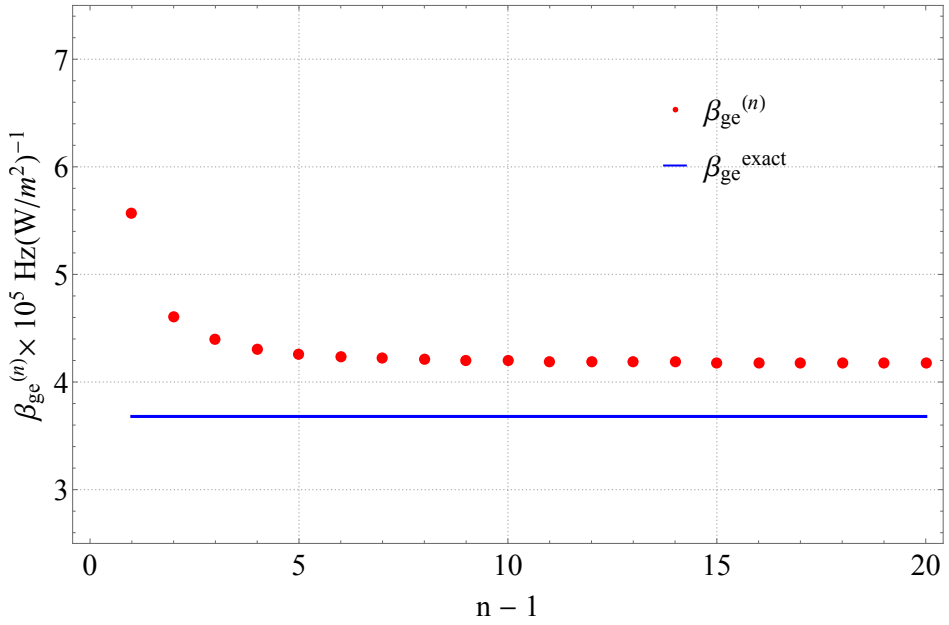

Figure 4.4: Quick estimation of 1S-2S two-photon transition element using Eq. 4.18. Each dot represents a higher order of P state included in the calculation. This method asymptotes at a value ≈ 14 % larger than the exact value.

With this value for the two-photon transition matrix element, we can now determine the two-photon Rabi frequencies for both Doppler-free and non-Doppler-free processes (see Eqs. 4.13 and 4.14). We can then modify the scattering rate equation given by Eq. 4.12 for two-photon excitation as

$$\Gamma_{DF} = \frac{\Gamma_{eff}\Omega_{DF}^2}{4\delta_{DF}^2 + \Gamma_{eff}^2 + 2\Omega_{DF}^2} \tag{4.19}$$

$$\Gamma_{NDF} = \frac{\Gamma_{eff}\Omega_{NDF}^2}{4\delta_{NDF}^2 + \Gamma_{eff}^2 + 2\Omega_{NDF}^2}, \tag{4.20}$$

where the detuning is written in terms of the atomic velocity as $\delta_{NDF} = (\omega_l/c)(v \pm v_{cool})$, where v_{cool} is the velocity of atoms the laser is detuned to for cooling and ω_l is the laser frequency. The $\pm$ represents the scattering from the forward and backward propagating beams. For the Doppler-free case, $\delta_{DF} = (\omega_a/c)(v)$. For a 60 W cooling laser with a 180 μm beam radius, detuned to cool 100 m/s atoms, with maximum quenching, $\Gamma_{eff} = 0.5 \cdot \Gamma_{2p}$, the scattering rates for each process are shown in Figure (4.5).

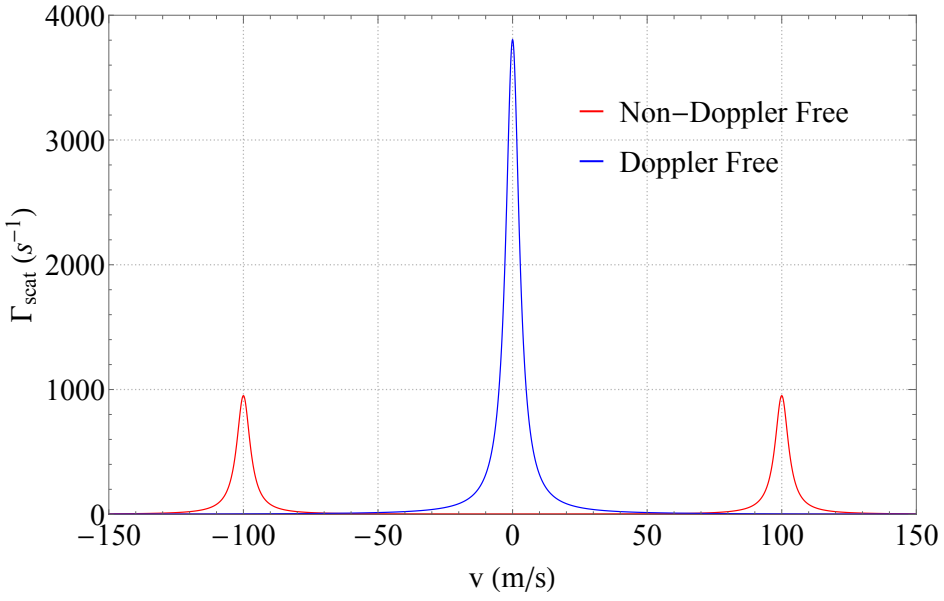

Figure 4.5: Scattering Rates for two-photon cooling laser at 60 W with 180μm beam waist.The DF scattering process is 4 times greater than the corresponding NDF processes.

A simplified estimate of the acceleration experienced by a specific velocity class of hydrogen atoms can be made by treating the atoms always on resonance with the cooling laser, which could be implemented via chirp-cooling. In this case, the acceleration experienced by an atom in this beam would be

$$a_{cool} = v_r \Gamma_{NDF}, \tag{4.21}$$

where $v_r = \hbar k_{l\alpha}/m = 3.3$ m/s. From basic kinematics, with $\Gamma_{NDF} = 1000$ s^{-1} this gives a stopping distance and time for $v_o = 100$ m/s atoms of

$$d_{stop} = \frac{v_o^2}{2a_{cool}} = \frac{m\lambda_{ly\alpha} v_o^2}{4\pi\hbar\Gamma_{NDF}} = 1.53\,\text{m} \tag{4.22}$$

$$t_{stop} = v_o/a_{cool} = 30\,\text{ms} \tag{4.23}$$

which would require that the frequency of the 972.5 nm MOPA is increased by $\sim$ 100 MHz as the atoms slow down. If successful, this cooling scheme would result in the arrival of bunched hydrogen at the end of the decelerator. This setup is physically realizable using a cryogenic beam overlapped with the 243.1 nm power. For instance, cryogenic beams of hydrogen at 6 K have been robustly demonstrated [5, 146]. Therefore, the slow velocity tail of such a distribution ($\sim$ 100 m/s) could be cooled to the recoil velocity in 30 ms over a distance of 1.5 meters.

It is worth noting that on resonance, with maximal quenching ($\Gamma_{eff} = \Gamma_{2P}/2$) the equations above can be approximated as

$$\Gamma_{DF} = \frac{\Omega_{DF}^2}{\Gamma_{eff}} = 2.7 \times 10^{-7} I^2 \text{s}^{-1} \frac{\text{cm}^4}{\text{W}^2} \tag{4.24}$$

$$\Gamma_{NDF} = \frac{\Omega_{NDF}^2}{\Gamma_{eff}} = 6.8 \times 10^{-8} I^2 \text{s}^{-1} \frac{\text{cm}^4}{\text{W}^2}, \tag{4.25}$$

This approximation uses the fact that $\Omega_{DF/NDF} << \Gamma_{eff}$. This is reasonable as $\Omega_{DF/NDF} = \Gamma_{eff}$ would require 243.1 nm intensities > 3×10^7 W/cm^2. As $I = 2P/(\pi w_o^2)$, for the ~ 200 μm beam we are proposing for cooling this would require 243.1 nm powers on the order of 20 kW, several orders of magnitude higher than our goal. Therefore, Eqs. 4.24 and 4.25 give quick and valid calculations of the two-photon scattering rate on resonance for realizable 243.1 nm powers. For example, the plots in Fig. 4.5 used the full form of the scattering rate in Eqs. 4.19 and 4.20 with $P = 60$ W and $w_o = 180\mu$m. This corresponds to an intensity of 1.2×10^5 W/cm^2. Using Eqs. 4.24 and 4.25 gives $\Gamma_{DF} = 3941$ s^{-1} and $\Gamma_{NDF} = 985$ s^{-1}, which matches the values in Fig. 4.5 on resonance. The factor of 4 difference between Eqs. 4.24 and 4.25 is important. One of the proposals for laser cooling hydrogen [25] used the Doppler-free scattering rate. For a while, we mistakenly referenced this value and we believed that 30 W of 243.1 nm power with a 180 μm beam waist could stop 100 m/s atoms in 1.5 meters. However, the scattering rate would be four times lower, meaning a stopping distance of 6 m would be required. Since $\Gamma_{NDF} \propto I^2$, we realized that we would need 60 W of power instead. This realization came after demonstrating 30 W of 243.1 nm power in an enhancement cavity, which somewhat diminished the results that are presented next. Nonetheless, 30 W of 243.1 nm intracavity power was an accomplishment, and was achieved before we power scaled our 243.1 nm laser system and optimized our use of UV optics. Therefore, this 60 W benchmark should be achievable with our power scaled laser system and knowledge we learned from building the deep-UV enhancement cavity. This knowledge is presented in the following section.

4.3 UV Enhancement Cavity

As we saw in the previous section, 1000 s^{-1} scattering rates for practical two-photon cooling of hydrogen would require 60 W of 243.1 nm power, greater than the output power of our 243.1 nm laser. Therefore, a CW enhancement cavity is needed since, as discussed in 3.2.2, the intracavity power within an enhancement cavity can reach values orders of magnitudes larger than the input power. Here we present the results on cavity enhancement of deep-UV radiation. The results

presented here are published in [142] and occurred in between the pre and post-power scaled laser system [114, 115], when we could generate on average 600-800 mW of 243.1 nm radiation. This section starts with a description of the beam preparation of our 243.1 nm laser output for cavity coupling, followed by a detailed description of the cavity design and performance.

4.3.1 243.1 nm Laser Output and Mode-Matching

The deep-UV enhancement cavity setup is shown in Fig. 4.6. Before we developed this system, we thought building up power in a linear cavity would be relatively simple. We already had the experience of building two bowtie enhancement cavities for intracavity frequency doubling. However, as we developed this linear enhancement cavity, there were numerous technical challenges that we did not face when building the doubling cavities, primarily due to the deep-UV wavelengths and high deep-UV powers with which we were working.

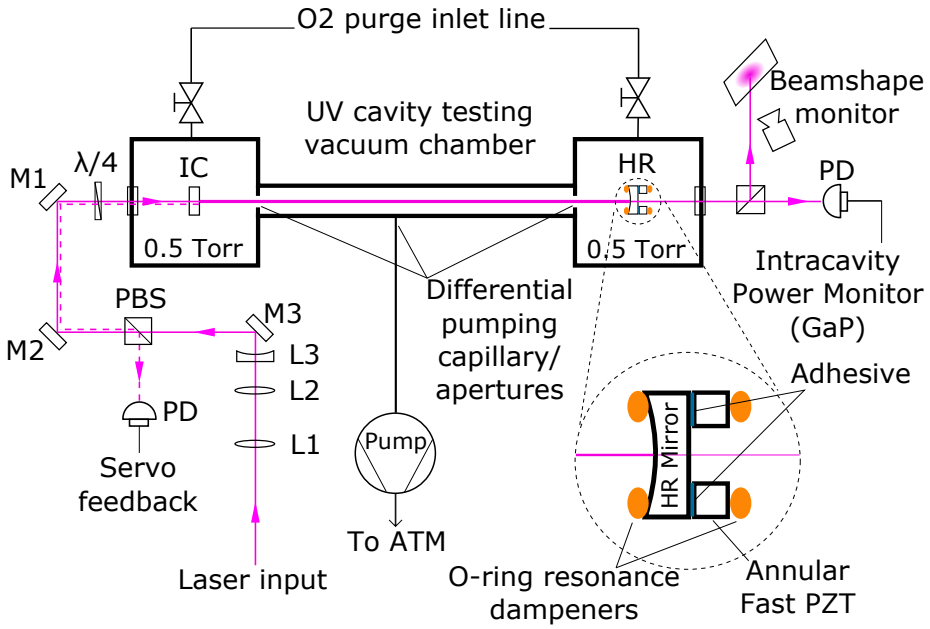

Figure 4.6: Diagram of enhancement cavity. The input UV beam is mode matched to the cavity using one spherical lens (L1) and two cylindrical lenses (L2 and L3). The reflection from the input coupler (IC) is optically isolated from the laser with a polarizing beam splitter (PBS) and quarter waveplate ($\lambda/4$). The transmission of the high reflector (HR) is monitored with a photodiode (PD) to determine the intracavity power.

The first technical challenge involved loss on the optics before the enhancement cavity (L1-L3, the polarizing beam splitter (PBS), and quarter-waveplate in Fig. 4.6). The lenses, L1-L3, were necessary for mode matching the 243.1 nm power to the cavity, whereas the PBS and quarter-waveplate isolated backreflections off the IC from the CLBO doubling cavity.

The lenses were a spherical lens (L1) followed by two cylindrical lens (L2-L3). The cylindrical lenses compensated for the walk-off angle of the CLBO, which gave the 243.1 nm radiation an elliptical output. The spherical lens collimated the 243.1 nm output. This was necessary as the linear cavity was formed by a high reflector with a ROC of $R = 4$ m and a flat IC, spaced apart by 0.75 m. Using the ABCD analysis from 3.2.4, this gives a focus at the IC with a beam waist of $w_o = 350\mu$m. The Rayleigh range of the 243.1 nm radiation with this focus is $z_r = \pi w_o^2/\lambda = 1.58$ m. The spot size at the curved mirror is then $w(z = 0.75\text{m}) = \sqrt{1 + (z/z_r)^2} = 390\,\mu$m, indicating the cavity would prefer a collimated input beam. Collimating the high power 243.1 nm radiation was challenging to do by eye as we had to rely on the flourescence of the UV light, which varied from one material to the next and appeared distorted at high power. We found Macor, a machineable glass ceramic as reliable imaging material, due to its minimal flourescence. We could then examine the image of the beam on the Macor with a CCD camera close to the 243.1 nm output and further away to determine the degree of collimation and ellipticity. Figure 4.7 shows the beam profile in two different locations separated by 1.14 m after reshaping. As can be seen, we can shape the 243.1 nm output beam to a nearly symmetric, Gaussian intensity profile.

As shown in Fig. 4.6 the lenses are followed by a PBS and λ/4 waveplate, which was our improvised method to isolate the cavity from the second doubling stage. The isolation is necessary as the enhancement cavity is linear, thus any power reflected off the input coupler is retroreflected back into the CLBO doubling stage. We have seen that without any attenuation of this retroreflected power, the output of the CLBO cavity is severely lessened. We believe this could be due to formation of a standing wave of UV radiation within the crystal that causes self-heating and phase mismatch. Generally, the most common method for isolation is use of a Faraday isolator. Unfortunately, most commercial optics have not been tested at these high, CW deep-UV powers.

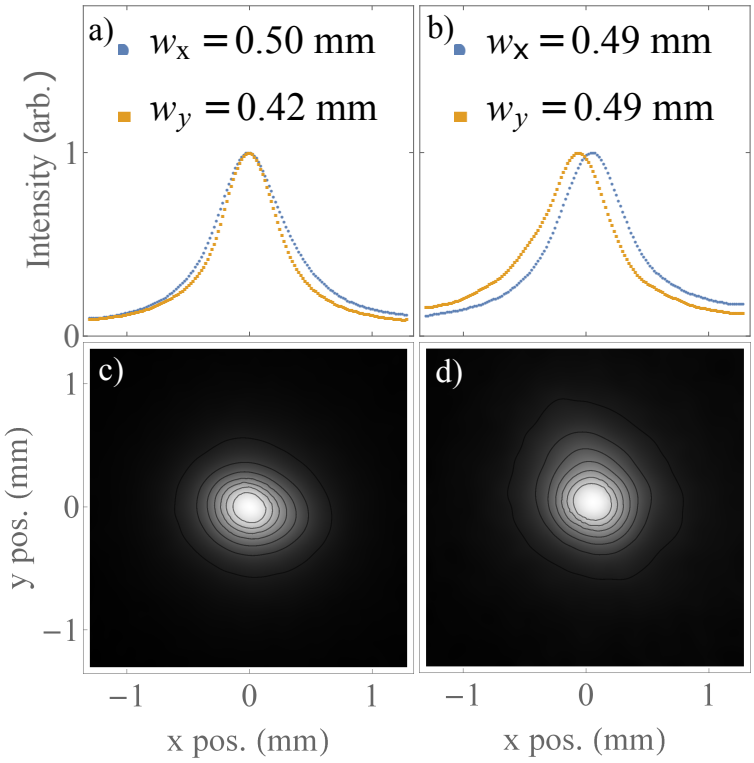

Figure 4.7: a) Profile of the laser output directly after the telescoping lenses, b) profiles of the laser output 114 cm after the beam shaping lenses. c) Image corresponding to the profiles in a). d) Image corresponding to the profiles in b). The beam images are taken at a power of 386 mW and w_x and w_y are respectively the x and y $1/e^2$ waists from fits to the intensity data.

While we were able to get a custom commercial Faraday isolator at these wavelengths, we found its transmission decreased to less than 50 % after a few days of high-power, deep-UV operation. Therefore, we used this improvised isolator consisting of a quarter wave plate and PBS. The PBS is made of UV fused silica, Corning 7980 0F grade, and has reliably provided > 98 % transmission over long-term, high-power, deep-UV operation.

However, we have found that not all UV fused silica optics are equal. The optics we have used for mode matching and beam isolation have had losses ranging from 1% to 10%. Due to these losses, even though we had ≈ 700-800 mW of 243 nm power directly from the CLBO doubling stage, we were able to achieve a maximum stable power at the deep-UV enhancement cavity input of 420 mW. Since this work was done, we have investigated whether the substrate or

AR coating are culprits for these losses. We have evidence to believe it is the substrate. Based on the reliability of the PBS (Lambda Optics HPB-25.4U-248), which we owe to its grade of UV fused silica, Corning 7980 0F grade, versus the significant losses on our original lenses that had a different substrate, we have since ordered AR coated cylindrical and spherical lenses from Lambda Optics made of the Corning 7980 grade UV fused silica to replace L1-L3. We have also developed our own Faraday rotators to replacte the quarter-wave plate that has high loss ~ 10 %. These rotators rotate the light polarization 45 $^\circ$ in the same direction regardless of the direction of propagation. Therefore, the back reflected light from the IC will have an orthogonal polarization to the incoming light, and can be separated from the incoming light with the PBS. To build these, we ordered UV fused silica (Corning 7980) light pipe homogenizing rods from Edmund Optics, and had them AR coated by Lambda optics. We then place these within commercially purchased cylindrical neodynium magnets to achieve the desired 45 $^\circ$ Faraday rotation. We measure a total loss of $\approx 10\%$ after transmission through all these new optics, a big improvement over the 30-50% seen with the original UV optics. However, we just started testing these optics at high power and time will tell whether they maintain this performance.

4.3.2 Cavity Performance

After the mode matching and beam preparation stage, the 243.1 nm laser output is coupled into the linear UV enhancement cavity. Despite the losses on the UV optics, we were able to couple efficiently into the cavity. We determine this by observing the cavity modes as the cavity length is scanned. This is done by moving the IC with a slow PZT and monitoring the transmission from the high reflector using a GaP photodiode, as seen in Fig. 4.6. With good mode matching, as can be seen in Fig. 4.8(a), we see minimal excitation of higher-order cavity modes. As the power of the laser is increased, we observed that the vertical waist of the beam at the output of the final doubling stage increases slightly, which in turn increased excitation of the higher-order cavity modes. We attribute this to a thermal variation in the CLBO crystal, which supports the self-heating behavior

we have seen in the crystal at its highest output powers. To compensate for this, we need to readjust the cylindrical lenses used to mode-match to the cavity as the laser power is varied.

Obtaining these cavity modes introduced a technical challenge that was not present with the doubling cavities. While for laser cooling and spectroscopy it is clear the intracavity 243.1 nm power should exist in a high-vacuum environment (hence the differential pumping components in Fig. 4.6), it is not obvious that vacuum is required purely for cavity enhancement of 243.1 nm power. However, 243.1 nm power is weakly absorbed in air. This leads to a phenomena called self-locking. This behavior can occur when laser power is converted into heat by a weakly absorbing medium, in our case air, within a high finesse cavity [147]. Therefore, we had to pump the atmosphere out of the cavity as seen in Fig. 4.6. This would shift the enhancement cavity, misaligning the cavity modes. Unfortunately, the cavity mirrors (IC and HR) were under vacuum and could not be readjusted to compensate for this misalignment as the enhancement cavity was one rigid component. While we were able to get around this problem by applying pressure to right spots on the structure of the enhancement cavity, this method wasn't ideal. Our new enhancement cavity design has the IC and HR mounted within externally movable housing that is non-rigidly connected to the rest of the enhancement cavity housing.

With these cavity modes, we can determine the amount of 243.1 nm power built up within the cavity as we scan over resonance. First, we have to remove the input coupler and carefully calibrate the transmission of the high reflector as a function of 243.1 nm laser using the GaP photodiode as shown in Fig. 4.6. We can then put the input coupler back in place, realign the cavity to achieve modes, and measure the new voltage on the photodiode while scanning the cavity length. Comparing this with the extrapolated calibrated curve, we can then determine the intracavity power. Using this method when scanning over the resonance, we saw a maximum intracavity power of 38 W with an input power of 420 mW. This corresponds to a buildup of ≈ 92. We used a 1.5 % IC, which using Eq. 3.18 indicates a loss of ≈ 1 % in the cavity from other sources. This matches the 1% estimate from the mirror manufacturer.

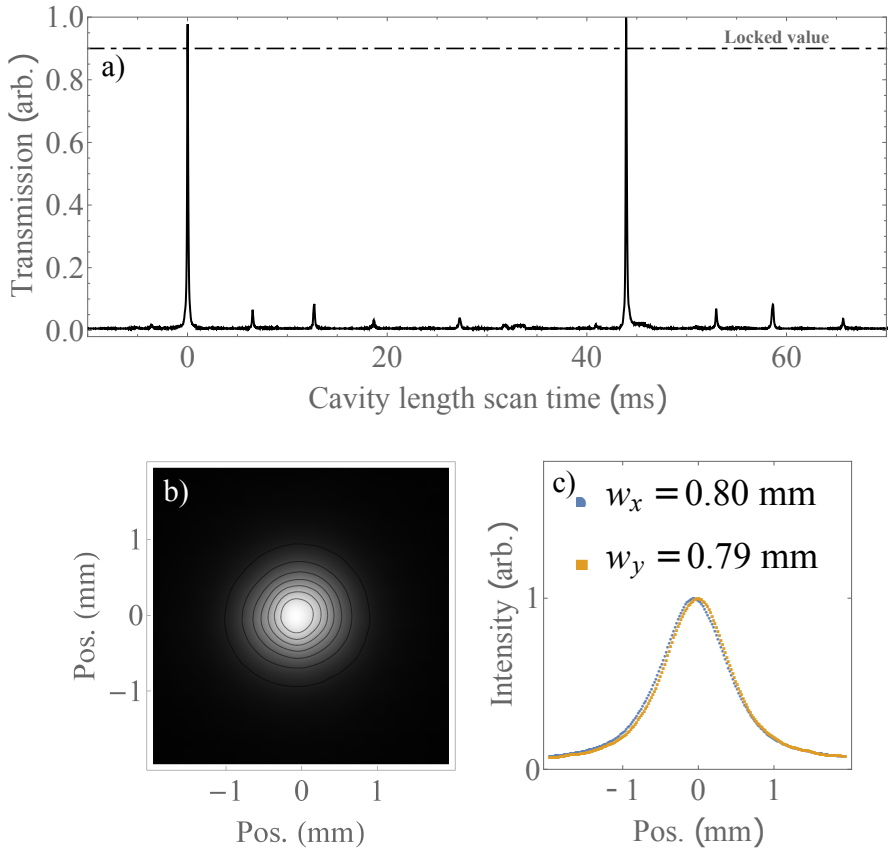

Figure 4.8: a) Cavity transmission as a function of frequency. The resonance width allows us to estimate the finesse to be ≈ 300 with > 80 % of the power in the TEM_{00} mode. b) Image of cavity transmission with 31 W of intracavity power. The image was taken 65.5 cm after the output coupler with a build up of 75. c) Cavity transmission profile.

The enhancement cavity is kept on resonance using a Pound-Drever-Hall (PDH) locking scheme [148]. We generate sidebands on the fundamental radiation at 972.5 nm using an electro-optic modulator (EOM). The sidebands are also imprinted on the quadrupled radiation which are used to generate a PDH error signal for the DUV enhancement cavity. As with the doubling cavities we use a fast and slow piezo-electric transducer (PZT) to keep the cavity locked. In the doubling cavities, the PZT actuator followed the design in [149] which consisted of a mirror glued to a square PZT fixed on a massive mounting structure designed to damp resonances, which is crucial to maintain a stable lock. Light cannot transmit through this PZT actuator design. This design worked with the bowtie geometry as there were mirrors that did not need to transmit light. In a linear cavity, light

must be transmitted through both mirrors which required an annular fast PZT and an alternative mirror mounting procedure to damp low frequency resonances. We used the method presented in [150]. This required a fair amount of technical development on our part, but in the end it worked well and we were able to maintain a stable lock.

When locked, we could measure a peak intracavity power of 33.7 W circulating with a buildup factor of 80.4 and an input of 420 mW. The linear dependence of the intracavity power as a function of input power is shown in Fig. 4.9.

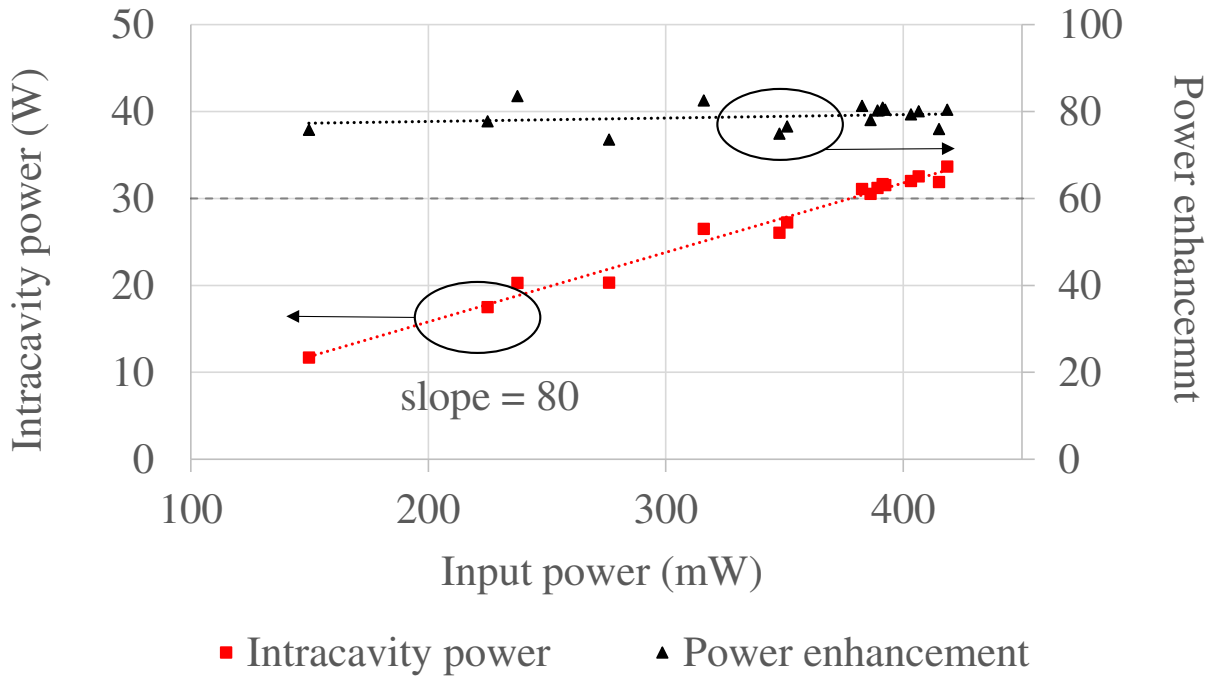

Figure 4.9: Deep-UV enhancement and intracavity power as function of 243.1 nm input power. We see a linear increase with intracavity power as a function of 243.1 nm input power, and no signs that the enhancement decreases as input power increases.

As indicated in Fig. 4.8a), this locked intracavity power is consistently 10 % lower than the intracavity power measured while the cavity is scanned over resonance. By triggering an oscilloscope to the voltage measured on the GaP photodiode when the cavity is locked, we measured that it takes ≈ 40 ms for the locked power to decay from the expected scanned power to this lower, steady state locked value. This time scale is indicative of a thermal affect; therefore, we attribute this behavior

to heating of the cavity mirror coatings. We were concerned that this unwanted thermal effect degraded the quality of the intracavity mode. However, we monitored the transmitted beam profile simultaneously as the cavity was locked (as shown in Fig. 4.8b–c), and observed that the beam shape was nearly Gaussian with a profile that did not change noticeably with power.

As mentioned in the introduction to this chapter, short wavelength optics are known to degrade when exposed to high power radiation due to surface oxygen depletion [140] and hydrocarbon contamination [141]. The mirrors we used were dielectric mirrors designed for high power and reflectivity using electron beam evaporation with a SiO_2 top surface layer (LaserOptik GmbH). According to [140], this helps reduce oxygen depletion. Nonetheless, we designed our enhancement cavity to allow a continuous purge of ultra high purity oxgyen gas onto the IC and HR (see Fig. 4.6). As we quickly learned, the oxygen was necessary. Without oxygen in the chamber the intracavity power would quickly degrade when the lock was engaged before the vacuum could even reach single-digit torr pressures. With a continuous flow of oxygen on the optics, this degradation would happen at lower pressures, $\approx$ 500 mtorr. Below this pressure of fresh oxygen, the mirrors would degrade over the course of several minutes. When we examined the mirrors after degradation, we noticed a thin film that could be cleaned off with organic solvents. We also noticed that the degradation rate decreased when we thoroughly cleaned the vacuum chambers housing the cavity mirrors. Therefore, we believe the degradation is caused by hydrocarbon contamination instead of oxygen depletion. This occurs from the high power UV radiation cracking residual hydrocarbons in the vacuum that then become deposited on the mirror surfaces. This supports the findings in [141]. Furthermore, the findings in [140] showed that mirrors with a SiO_2 top surface (like the mirrors used here) help reduce oxygen depletion, also supporting our conclusion. With a thoroughly cleaned vacuum chamber and 500 mtorr of continuous flowing oxygen, we could keep the cavity continuously locked at $>$ 30 W intracavity 243.1 nm power for an hour of operation.

4.4 Conclusion

We have demonstrated that a high-power 243.1 nm laser can be cavity enhanced by a factor of 80. With $\approx$ 400 mW of available input power at the cavity, this led to intracavity powers of > 30 W. While this is half the power we need for practical laser cooling setups, we saw no evidence that the enhancement drops as power increases. With the post power scaled system, > 1 W of 243.1 nm output power is available. With the correct grade of UV fused silica, < 10% total loss on all the optics leading to the enhancement cavity should be possible, suggesting input powers on the order of 1 W are possible. This would lead to intracavity powers of 80 W, which exceed the required power for two-photon cooling as well as the proposed upgrades for increased precision on the muonium 1S-2S transition [32].

Unfortunately, operation of this cavity required 1/2 Torr of O_2 on the mirrors. This is a technical challenge as spectroscopy and laser cooling experiments require high vacuum. This could be achieved through differential pumping, but a more attractive option are mirror coatings that don't require oxygen. It is possible certain fluoride coatings could be a solution and we are investigating these options with laser coating manufacturers. As these manufacturers don't have access to these levels of 243.1 nm power, our system is a testing ground for high-power, deep-UV optics. With the correct optics, a robust, 100 W intracavity power deep-UV cavity at 243.1 nm seems possible.

Chapter 5

Single Optical Scatter Capture of Hydrogen in a Magic Wavelength Dipole Trap

5.1 Introduction

The AC Stark shift of a laser red-detuned for a specific atomic transition can form an attractive potential for the ground state of the atom. This led to the first demonstration of optically trapped atoms in 1986 [151]. Since this demonstration, optically trapped atoms have proved invaluable for precision spectroscopy. Using magic wavelength optical traps [152, 153], in which the AC Stark shift is equivalent for both the ground and excited state of the spectroscopic transition, optical lattice clocks of neutral atoms have demonstrated frequency uncertainties at the 10^{-18} level [15]. While laser cooling would improve precision spectroscopy of hydrogen by reducing velocity effects, the ultimate precision could be achieved in the tight confinement of a magic wavelength optical lattice. Capturing hydrogen in a magic wavelength dipole trap would be the first step to realizing this goal. While the magic wavelength for the 1S-2S transition in hydrogen was recently calculated [144, 145], the general method for capturing atoms in optical traps requires robust laser cooling of the atomic sample beforehand. With the 243.1 nm powers we have demonstrated, we explored through simulations the feasibility of capturing hydrogen in a dipole trap using two-photon cooling.

In this chapter, we present a novel technique for capturing hydrogen in a magic wavelength dipole trap unique to hydrogen with its light mass and large recoil velocity. We demonstrate through Monte Carlo wave function simulations that hydrogen atoms can be captured in experimentally viable optical traps through a single two-photon cooling cycle, which we will refer to as a single scatter. The chapter begins with a brief review of the AC Stark shift and determination of the magic wavelength. Then, the proposed single scatter capture method for loading hydrogen

in a dipole trap is justified and presented. This method is then analyzed using Monte Carlo wave function simulations for atomic trajectories, determining the atomic flux necessary for reasonable capture rates. The chapter concludes with a discussion of extending these results to capture in optical lattices.

5.2 AC Stark Shift and Magic Wavelength

For the two-level atom interacting with laser radiation presented in 4.2, we saw that we could write the interaction Hamiltonian $\mathcal{H}'$ as

$$\frac{\hbar}{2}\begin{pmatrix} 0 & \Omega \\ \Omega & -2\delta \end{pmatrix}\begin{pmatrix} c_g' \\ c_e' \end{pmatrix} = \mathcal{H}'\begin{pmatrix} c_g' \\ c_e' \end{pmatrix} = i\hbar\frac{d}{dt}\begin{pmatrix} c_g' \\ c_e' \end{pmatrix}, \tag{5.1}$$

where $\Omega = E_o\mu_{eg}/\hbar$ is the Rabi-frequency with E_o the electric field amplitude of the laser, $\mu_{eg} = e\langle e|z|g\rangle$ the transition matrix element between the ground and excited state for z-polarized radiation, and $\delta = \hbar(\omega_l - \omega_{eg})$ the detuning of the laser frequency from the natural frequency of the transition. The eigenvalues for this interaction Hamiltonian give the shifted energies caused by the laser interaction, and they are

$$E_{1,2} = \frac{\hbar}{2}(-\delta \pm \sqrt{\delta^2 + \Omega^2}). \tag{5.2}$$

For $\Omega = 0$, Eq. 5.2 returns $E_1 = 0$ and $E_2 = -\hbar\delta$ which are the energies we expect when the levels are not perturbed by the laser interaction, which makes sense in the interaction picture as the levels are δ apart due to the detuning of the laser. As the laser intensity becomes non-zero, so does Ω and we see a shift from the detuning that is a light shift from the electric field of the laser. This is referred to as an AC Stark shift, and treating the electric field as a perturbation, we can rewrite Eq. 5.2 as

$$E_{1,2} = \frac{\hbar}{2}(-\delta \pm \delta\sqrt{1+\frac{\Omega^2}{\delta^2}}) \tag{5.3}$$

$$= \frac{\hbar}{2}(-\delta \pm \delta(1+\frac{\Omega^2}{2\delta^2} + \mathcal{O}(\Omega^4)) \tag{5.4}$$

$$= \frac{\hbar}{2}(-\delta \pm \delta(1+\frac{E_o^2\mu_{eg}^2}{2\hbar^2\delta^2} + \mathcal{O}(E_o^4)) \tag{5.5}$$

From Eq. 5.5 we see that the energy shift for the two states is opposite in sign but equivalent in amplitude, given by,

$$\Delta E_{1,2} = \pm\frac{E_o^2\mu_{eg}^2}{4\hbar\delta} \tag{5.6}$$

$$= \mp\frac{1}{4}\frac{e^2}{\hbar}\frac{|\langle e|z|g\rangle|^2}{\omega_{eg}-\omega_l}E_o^2 \tag{5.7}$$

$$= \mp\frac{1}{4}\alpha(z,\omega)E_o^2 \tag{5.8}$$

where

$$\alpha(z,\omega_l) = \frac{e^2}{\hbar}\frac{|\langle e|z|g\rangle|^2}{\omega_{eg}-\omega_l} \tag{5.9}$$

is referred to as the electric dipole polarizability of an atom, which depends on the polarization (z in this case), and frequency (ω_l) of the interacting laser radiation. From the denominator of Eq. 5.7 we see that the electric field of a laser can shift the energy levels up or down depending on the detuning. We see that for blue-detuning ($\omega_l > \omega_{eg}$) the ground state in this two level system has its energy shifted up, while the excited state is shifted down. For red-detuning ($\omega_l < \omega_{eg}$), the ground state has its energy shifted down, while the excited state is shifted up. This is the physical mechanism behind optical traps. With an intense laser that is red-detuned, the ground state's downward shift in energy forms an attractive potential that is large enough to capture atoms!

The AC stark shift determined by α in Eq. 5.9 was determined for a two-level system. As was the case with two-photon transitions, all the possible states in atom must be considered for an accurate determination of the AC Stark shift. This recasts the electric dipole polarizability for z-polarized light for the state $|n\rangle$ in the form [144]

$$\alpha(z,\omega_l) = \frac{2e^2}{\hbar}\sum_k \frac{\omega_{kn}|\langle k|z|n\rangle|^2}{\omega_{kn}^2-\omega_l^2}, \tag{5.10}$$

where the sum over $\langle k|$ includes all the discrete virtual states of the system. The form shown here matches the form derived for the two-level atom in Eq. 5.9 since $\omega_{kn}/(\omega_{kn}^2-\omega_l^2) = \omega_{kn}/[(\omega_{kn}-\omega_l)(\omega_{kn}+\omega_l)] \approx \omega_{kn}[2\omega_{kn}(\omega_{kn}-\omega_l)] = 1/2(\omega_{kn}-\omega_l)$ using the rotating wave approximation, which was used in deriving the form of α for the 2-level atom.

From Eq. 5.10, it is clear that different states $|n\rangle$ will in general have different polarizabilities. However, due to α's dependence on ω_l it is possible to find a value, called $\lambda_{magic} = 2\pi c/\omega_{lm}$ such that two states $|n_1\rangle$ and $|n_2\rangle$ have equal polarizabilities. This magic laser frequency (ω_{lm}), called the magic wavelength, as explained in the introduction to the chapter is very important for spectroscopy of trapped atoms. Spectroscopists interested in studying a specific transition in an atom can trap the atom in a magic wavlength trap. Due to the equivalent polarizabilities of each state, both the levels of the transition experience the same AC Stark shift, allowing scientists to recover the natural transition frequency unperturbed by the strong trapping laser field.

This magic wavelength was recently calculated for the 1S-2S transition in hydrogen [144, 145]. They found in [145] $\lambda_{magic} = 514.6$ nm with $\Delta E_{1S,2S} = -221.6$ Hz/(kW/cm^2). As with the two-photon transition matrix calculation, the sum over an infinite number of states is challenging, and a common technique is to instead use Green's functions that can be summed in close analytic form [145]. This formalism also enables consideration of the effect the continuous part of the spectrum has on α, and provided a more accurate value than the first calculation done [144] that didn't employ the Green's function formalism.

5.3 Single Scatter Capture Feasibility and Procedure

The magic wavelength AC Stark shift of the 1S–2S transition in hydrogen, $\Delta E_{1S,2S} = -221.6$ Hz/(kW/cm^2), is small compared to typical atomic clock candidates, while the recoil energy of hydrogen at the magic wavelength, $T_{rm} = 72\,\mu$K, is large in comparison. Therefore, deep traps would be needed to capture hydrogen effectively. Fortunately, developments in Yb-fiber amplifiers and progress in high power SHG with LBO promises large powers, > 20 W at λ_{magic} [154, 155]. An enhancement cavity with a buildup of 1000 would give 20 kW. This intracavity power in a near concentric cavity with 50 mm ROC and 20 μm focus would give an intensity of ≈ 3 GW/cm^2. The intensity on the mirrors would be ≈ 8 MW/cm^2, which is well below the limits of the ≈ 100 MW/cm^2 damage threshold tested in the IR [156]. In the visible, the threshold should be half that of the IR, which is still well above 8 MW/cm^2. Such buildup in a cavity suggests trap depths up to the $1000E_{rm} = 1000k_bT_{rm}/2 \approx 5 \times 10^{-25}$ J could be attainable, which is capable of trapping atoms with equivalent kinetic energy, ≈ 25 m/s for hydrogen atoms.

Although large trap depths at the hydrogen magic wavelength are possible, loading such a trap without laser cooling proves ineffective. This is illustrated by a quick estimate of the loading rate using the standard procedure of capturing atoms in an optical trap by turning the trap field on as the atoms pass through it. Modeling after the current 1S-2S setup, a 6K hydrogen beam with flux of a 10^{15} atoms/sec would be a distance $d \approx 30$ cm from the trapping laser focus of $w_{om} = 20\mu$m. Treating the flux from the hydrogen beam as an effusive isotropic hemi-sphere of area $2\pi d^2$, the geometric overlap between this and the trapping region would be $g_l = 2w_{om}^2/(2\pi d^2) \sim 3 \times 10^{-9}$. Furthermore, only 0-25 m/s of atoms are trappable. Assuming a Maxwell-Boltzmann distribution for 6 K atomic beam, this leads to another loss of $m_l \approx 2 \times 10^{-5}$. Therefore, of the 10^{15} atoms/sec, only 60 atoms/sec that are trappable would pass through the trapping region. With a finesse of 1000 to build up to the 20 kW necessary for the trapping depth, the trap would build up in at most 0.3μs, meaning there is $\sim 2 \times 10^{-5}$ chance of trapping an atom in one trap ramp up time.

While this standard method for trapping hydrogen in a dipole trap seems improbable for hydrogen atoms without hydrogen already confined in a MOT, the large recoil energy of hydrogen offers

a unique method for loading a dipole trap—through rapid removal of excess kinetic energy by a UV cooling laser as the atom traverses the attractive trap potential (see Fig. 5.1). While similar ideas have been proposed and implemented for heavier atoms, these previous methods relied on optical pumping [157, 158] and Sisyphus cooling [159] techniques that required $N \gg 1$ photon scatters to remove the excess kinetic energy. For hydrogen, we will show that the energy removed from N = 1 photon scatters on the 1S-2S(2P) transition is enough to trap the atom the in 1S ground state of an existing dipole trap.

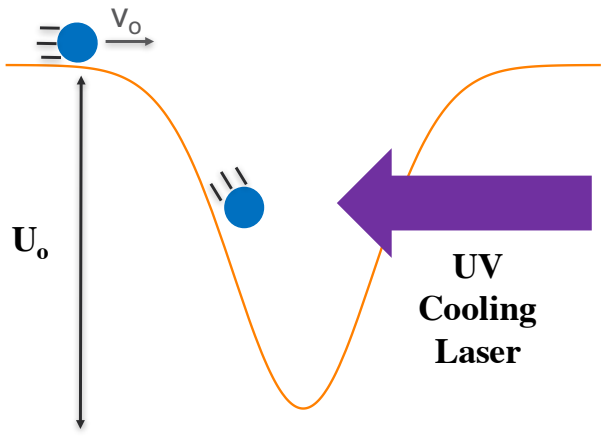

Figure 5.1: A hydrogen atom with initial velocity v_o falling down a conservative, attractive dipole potential will increase in speed. A counter propagating UV cooling laser red-detuned to address atom velocities only possible near the bottom of the well can remove excess kinetic energy, trapping the atom in the conservative potential.

Using a simple 1D model for the conservative nature of an optical dipole trap potential, the velocity of an atom traveling through the potential is $v = \sqrt{2 * d * U_o/m + v_o^2}$, where d is the depth ($d = 0$ outside the trap and $d = 1$ at bottom), U_o is the depth of the trap, m is the mass of a hydrogen atom, and v_o is the velocity of the atom entering the trap. For the case $v_o = 0$, this equation gives the minimum velocity, $v_{min} = \sqrt{2 * d * U_o/m}$ an atom must have to escape the potential as a function of trap depth. Therefore, $v_e = v - v_{min}$ indicates the excess velocity of the atom that must be removed to trap an atom. The recoil velocity of hydrogen for the 1S-2S/2P transition is, $v_{rc} = 3.3$ m/s. FIG. 5.2 shows the number of recoils on this transition needed to trap

a hydrogen atom in a simple 1D potential for different starting velocities and trap depths in terms of the recoil energy at λ_m of $E_{rm} = k_b * T_{rm}/2 = 5 * 10^{-28}$ J.

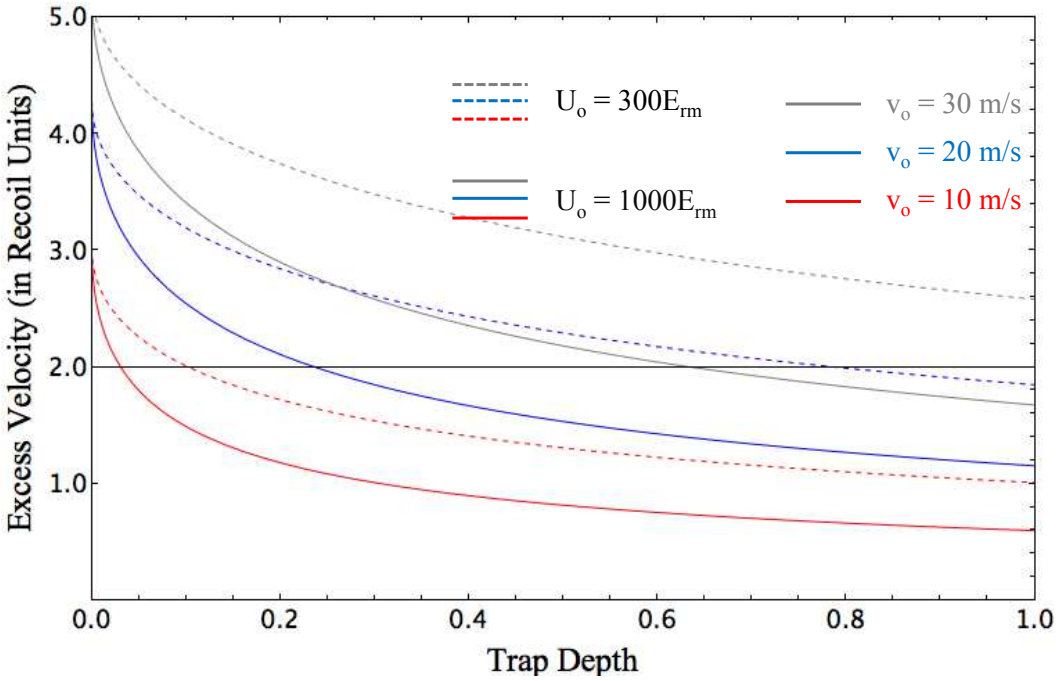

Figure 5.2: Excess velocity of an atom moving through a 1D potential as a function of potential depth. The excess velocity, v_e is in units of the hydrogen recoil velocity for scattering on the 1S-2S transition, $v_{rc} = 3.3$ m/s, where the trap depth d, is in units of U_o.

For a single scattering event on the 1S-2S/2P transition, the atoms forward velocity will experience a change of $-v_{rec}$ during absorption, but anywhere from $-v_{rec}$ to $+v_{rec}$ during the random emission. Therefore, an atom's forward velocity has the potential to be reduced by 0 to $2v_{rec}$ during a single scattering event. From FIG. 5.2, we see that for $v_o = 10$ or 20 m/s and $U_o = 1000E_{rm}$, as well as $v_o = 10$ m/s and $U_o = 300E_{rm}$, the atom is potentially trappable from a single scattering event in a significant portion of the potential.

Extending this simple 1D picture to a realizable experimental setup, a proposed capture method is shown in Fig. 5.3. A traveling Gaussian wave magic wavelength dipole trap with potential

$$U_m(x,y,z) = U_o \frac{w_{om}^2}{w_m^2(z)} \exp\Big[\frac{-2(x^2+y^2)}{w_m^2(z)}\Big], \tag{5.11}$$

where w_{om} is the beam waist at the focus of the magic wavelength radiation. The beam waist depends on z, $w_m^2(z) = w_{om}^2[1 + (z/z_{rm})^2]$ where $z_{rm} = \pi w_{om}^2/\lambda_m$ is the Rayleigh length. The peak trap depth is defined by the calculated AC Stark shift, and is $U_o = \Delta E_{1S,2S} I_{om}$, where $I_{om} = 2P_{om}/(\pi w_{om}^2)$ is the intensity of the magic wavelength laser with power P_{om}. This dipole trap potential will intersect orthogonally with a travelling Gaussian wave cooling laser beam, with intensity given by

$$I_c(x,y,z) = I_{oc} \frac{w_{oc}^2}{w_c^2(x)} \exp\Big[\frac{-2(y^2+z^2)}{w_c^2(z)}\Big]. \tag{5.12}$$

A cryogenic beam aligned nearly anti-parallel to the cooling laser is placed a given distance from the intersection of these two beams, which we will call the trapping region, with area $A = 2w_{om} \times 2w_{oc}$. As the atom passes through the trapping region, its speed in the x-direction will increase, coming in resonance with the red-detuned cooling laser.

The two possible scattering cycles that start and end in the 1S state are the same as the cooling cycles proposed for single-photon and two-photon cooling hydrogen. For the single-photon cooling cycle, Lyman-α radiation would excite from the 1S-2P and decay rapidly back to the 1S due to the short lifetime of the 2P state. There are two challenges with this single-photon absorption approach. The first is the limited interaction time of the atom with the Lyman-α radiation. Scattering rates on the order of 10^6 s^{-1} are necessary to insure the radition interacts with the atom since a 20 m/s atom will cross a 20 μm standing wave beam waist in $\sim$ 1 μs. For Lyman-α light, the 1S-2P transition can be excited with a scattering rate on resonance of $4.4 * 10^3 I$ $s^{-1}(W/m^2)^{-1}$. Currently, the best CW Lyman-α sources can output $\sim$ 1 nW of power [160, 161]. Focused to 20μm, this would give scattering rates of $< 0.01 \times 10^6$ s^{-1}. Furthermore, while the 1S and 2S levels experience the same, red-detuned AC stark shift in the magic wavelength trap, the 2P AC stark shift is

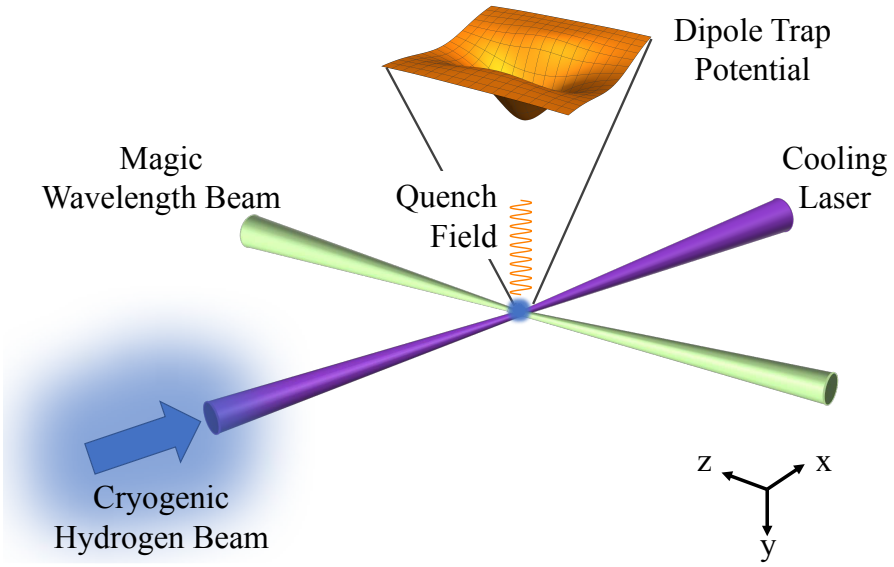

Figure 5.3: The proposed experimental setup for capturing hydrogen in a dipole trap. A cryogenic hydrogen beam will emit in the +x direction, some distance from the trapping region. As the atoms pass through the trapping region, the 243 nm radiation can remove excess kinetic energy of the atoms capturing them. A quenching field overlaps with this region in order to mix the 2S and 2P states. For the simulations done here, $w_{om} = 30\mu$m, and $w_{oc} = 20\mu$m.

approximately an order of magnitude larger and blue-detuned, $\Delta E_{2P} = 3011$ Hz/(kW/cm^2) [162]. Therefore, as seen in Fig. 5.4, relative to the 1S and 2S energy levels, the 2P energy level will vary as the atom passes through the trap, preventing Lyman-α radiation from staying on resonance and decreasing the already limited scattering rate further.

As the 1S and 2S have the same Stark shift in the magic wavelength trap, the 243.1 nm radiation frequency doesn't face the changing energy level problem that a 1S-2P transition would. Furthermore, the large 243.1 nm power demonstrated by our laser system promise scattering rates > 10^6 s^{-1}, increasing the likelihood an atom passing through the trap interacts with laser. However, the quenching from the 2S to 2P is complicated as the energy separation between these states depends on the position of the atom in the trap. This, in turn, introduces a position dependent AC stark shift of the 2S state as a result of the microwave field. Therefore, in the end, the correct laser frequency to address the 1S-2S transition depends on the Doppler shift of the atoms and microwave AC stark shift of the 2S state, while the correct microwave frequency to address 2S-2P transition depends on

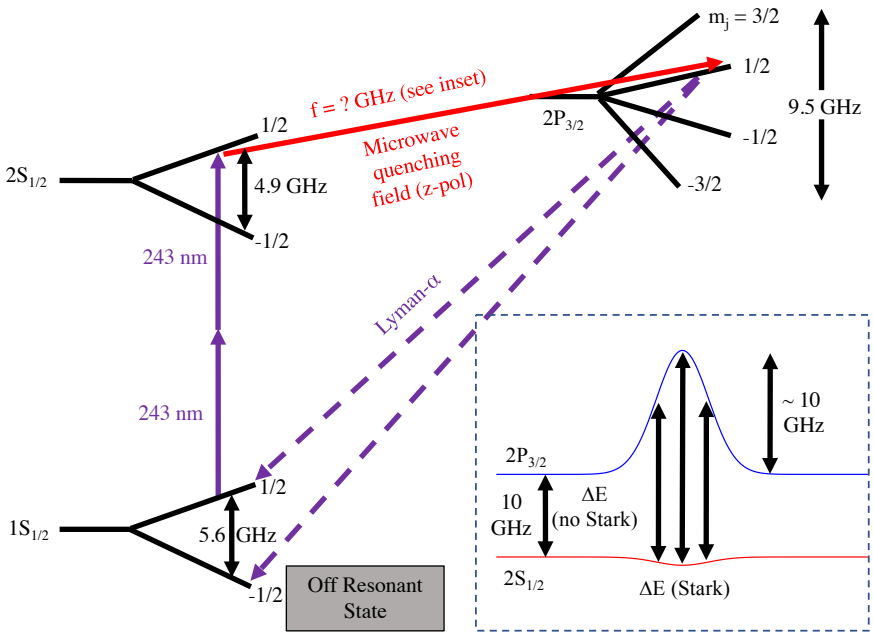

Figure 5.4: Energy levels of interest for single scatter cooling capture. The 243.1 nm radiation excites atoms from the 1S m_j = 1/2 to 2S m_j = 1/2, upon which a z-polarized microwave field mixes this 2S state with the $2P_{3/2}$ m_j = 1/2 state, enabling decay back to the 1S m_j = 1/2 or m_j = -1/2 state. Due to large hyperfine splitting of the 1S state, the 1S m_j = -1/2 state is off-resonant with the two-photon excitation. The transition frequency between the 2S and 2P states depend on the position of the atom in the trap, as the 2S and 2P states have different AC Stark shifts. The atoms are placed in a static magnetic field of 0.17 T, which separates the levels and enables the system to be modeled as a 3-level system through distinct separation of different m_j states.

the dipole trap and microwave AC stark shift of the 2S and 2P levels, all of these shifts dependent on the position of the atom in the trap.

Ultimately, we are interested in the probability an atom passing through the dipole trap will scatter. However, the variety of field shifts that are position dependent make it challenging to quantify the linewidth of the mixed 2S/2P state as well as the detuning from resonance for both the 1S-2S and 2S-2P transitions; therefore, a standard steady state scattering rate equation like the one used in 4.2 to analyze two-photon cooling cannot be used. Instead, we have chosen to keep track of the atomic trajectory as well as its population in each of the three levels using a Monte Carlo wave function approach.

5.4 Simulation Procedure

The Schrodinger equation for our 3-level system can be written as

$$\hbar \begin{pmatrix} -\omega_1 & \Omega_1 \cos\left[(k_l v_x + \omega_l)t\right] & 0 \\ \Omega_1 \cos\left[(k_l v_x + \omega_l)t\right] & 0 & \Omega_2 \cos\omega_q t \\ 0 & \Omega_2 \cos\omega_q t & \omega_2(x,y,z) - i\Gamma_{2P}/2 \end{pmatrix} \begin{pmatrix} a \\ b \\ c \end{pmatrix} = i\hbar \begin{pmatrix} \dot{a} \\ \dot{b} \\ \dot{c} \end{pmatrix} \tag{5.13}$$

where a, b, c correspond to the 1S, 2S, and 2P states of interest. The laser frequency is ω_l, which is double the frequency of the 243.1 nm radiation, ω_1 is the natural separation between the 1S-2S, and v_x the speed of the atoms. The Rabi frequencies between the 1S and 2S and 2S and 2P are respectively, Ω_1 and Ω_2. The Rabi frequency of the 243 nm laser is defined as $2[2\pi\beta_{1S2S} I_c(x,y,z)]$ where $\beta_{1S2S} = 3.68 \times 10^{-5}$ Hz/(W/m^2)$^{-1}$ and $I_c(x,y,z)$ is defined in Eq. 5.12. For the simulations run here, $w_{oc} = 20\mu$m, while P_{oc} is varied between 1-30 W. The Rabi frequency of the microwave quenching field does not have position dependence over the trapping region as the beam must have a waist of ~ 1 cm or larger. The frequency of the microwave quenching radiation is ω_q. The trap dependent energy separation between the 2S and 2P levels is $\omega_2(x,y,z) = \omega_2 + 2\pi h[U_{2P}(x,y,z) - U_{2S}(x,y,z)]$, where ω_2 is the natural energy separation between the 2S and 2P states and U is the energy shift of the 2S and 2P states in the trap which can be found using Eq. 5.11. Using the rotating wave approximation for the 1S and 2S levels, this can be written as

$$\begin{pmatrix} \delta_1 & \Omega_1/2 & 0 \\ \Omega_1/2 & 0 & \Omega_2 \cos\omega_m t \\ 0 & \Omega_2 \cos\omega_m t & \omega_2(x,y,z) - i\Gamma_{2P}/2 \end{pmatrix} \begin{pmatrix} a \\ b \\ c \end{pmatrix} = i \begin{pmatrix} \dot{a} \\ \dot{b} \\ \dot{c} \end{pmatrix} \tag{5.14}$$

where $\delta_1 = \omega_l - \omega_1 + (\omega_l/c)v_x$ is the Doppler accounted detuning between the 1S and 2S.

Using $\vec{F} = -\vec{\nabla}U_m$, where U_m is defined in Eq. 5.11, we use a symplectic integrator to solve for the trajectory of the atom as it moves through the trapping region. For the simulations here, $w_{om} = 30\mu$m and $P_{om} = 20$ kW, giving $U_{om} \approx 5 \times 10^{-25}$ J. At each step in the symplectic integrator, we use 4th order Runge-Kutta to solve the three differential equations in Eq. 5.14, which lets us keep track of the population in each of the three levels. Following the Monte Carlo wave function approach [163], after each step, the probability of a cooling scatter is simply $P = \Gamma_{2P} dt |c|^2$, where dt is the integration time step, versus the probability of photoionization $P_{photo} = 2\pi\beta_{ion,2S} dt |b|^2$ where $\beta_{ion,2S} = 1.2 \times 10^{-4}$ Hz (W/m^2)$^{-1}$ [27]. Due to the short lifetime of the 2P state, decay from this state is dominant over photoionization. We have found no difference in our results when including photoionization from the 2P state into the photoionization probabilty. The scatter probability is compared to a number chosen randomly over a uniform distribution from 0 to 1, ϵ. If $\epsilon > P$, a scatter does not occur, the levels are renormalized to account for the non-Hermitian behavior of the Hamiltonian [163], and the numerical integration continues. If $\epsilon < P$, then a scatter does occur. In this case, the atom experiences a reduction in it's x-velocity of 3.3 m/s, followed by a random spontaneous emission that we treat as isotropically in space (this is an approximation as it would actually follow a dipole radiation pattern). The atom's kinetic energy K is then recalculated. If $K + U > 0$ the scatter did not successfully trap an atom and the trajectory is considered lost. If $K + U < 0$, the atom is trapped. This trapped value $\mathcal{T}$ is defined between 0 and 1, depending on the probability the trapped atom may have photoionized before becoming trapped. If $P_{photo} > 1$, then $\mathcal{T} = 0$. For a single trajectory through the well, this process is run a large number of times to simulate the stochastic nature of the scattering process, summing $\mathcal{T}$ for each run.

5.5 Simulation Results

5.5.1 Single Trajectory

Due to the varying number of position dependent energy shifts of both the 2S and 2P levels, which depend sensitively on the quenching amplitude, it is challenging to predict the optimal frequency of ω_l and ω_q. To determine this, we fix the quenching amplitude Ω_2 at a value that

would maximally couple the 2S and 2P states for their natural fixed energy separation of ≈ 10 GHz, $\Omega_2 = 5 \times 10^9$ s^{-1}. We then determine the probability of capturing an atom, $\mathcal{C}$, passing at a 10 degree angle with $v_{o,x} = 13$ m/s through the trapping region for different values of ω_l and ω_m. The 10 degree angle insures that the atom only passes through the 243 nm beam as it approaches the trapping region, preventing photoionization or scattering before this region. The results are shown in Fig. 5.5 for $\Omega_2 = 5.0 \times 10^9$ rad/s and $P_{o,243} = 12.5W$. We can understand the results as follows. Near the bottom of the trap, where an atom is most likely to be capture if scattered, the speed is ≈ 25 m/s for $v_{o,x} = 13$ m/s, which corresponds to a first order Doppler shift of ≈ 0.2 GHz. As well, near the bottom of the trap, due to the AC stark shift of the trap on the 2S and 2P, their separation is ≈ 20 GHz. From these values, we see that for $\omega_m < 20$ GHz, the quenching field is red-detuned and the AC stark shift of the quenching field shifts the 2S level down. Therefore, the frequency of ω_l needs to be further red-detuned to address the 1S-2S transition. For $\omega_q > 20$ GHz, the quenching field is blue-detuned and the AC stark shift of the quenching field shifts the 2S state higher in energy. Therefore, the frequency of ω_l needs to be blue-detuned to address the 1S-2S transition. As this AC stark shift of the quenching field increases in amplitude as ω_q approaches the natural energy separation of ≈ 20 GHz, we see that the detuning of ω_l increases when approaching this condition.

From Fig. 5.5 we can fix the detuning of the quenching field and cooling laser at judicious values and explore how the amplitude of both these fields affect the loading rate, with results shown in Fig. 5.6. We can understand the results as follows. As Ω_2 was fixed at 5×10^9 rad/s for exploring the detuning, we see this quenching amplitude is the most favorable for capturing. At higher amplitudes, the 2S level is shifted too high relative to the fixed 243 nm laser detuning, and only high 243 nm powers are able to overcome this decreased scattering rate from the 1S-2S. However, for lower quenching amplitudes, this problem is lessened. The reason at these amplitudes the capture rate doesn't increase with intensity is that the photoionization rate that affects the capture rate increases with larger intensity.

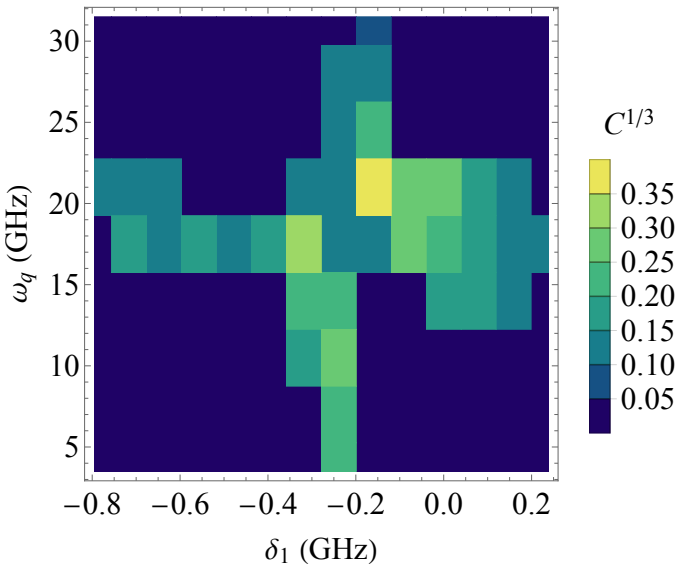

Figure 5.5: Capture probability as a function of 243.1 nm detuning and quenching detuning. For this simulation, $\Omega_2 = 5.0 \times 10^9$ s^{-1}, and $P_{oc} = 12.5$ W.

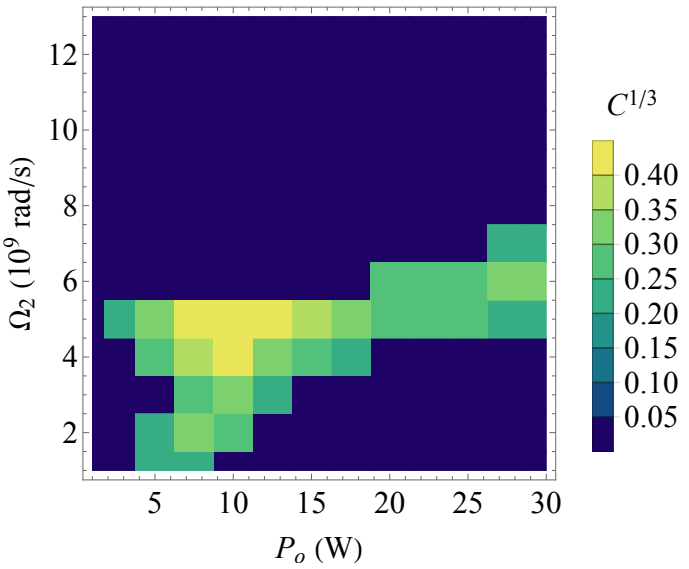

Figure 5.6: Capture probability as a function of 243.1 nm radiation and microwave quenching power. For this simulation, $\delta_1 = -1.0 \times 10^9$ s^{-1}, and $\omega_2 = 21$ GHz.

Due to the large intensities of the 243.1 nm laser, atoms captured that remain within the 243.1 nm laser have a significant chance of photoionizing. Therefore, the total loading rate into the trap can be approximated as

$$\frac{\mathrm{d}N}{\mathrm{d}t} = \Phi\mathcal{C} - \mathcal{L}N \tag{5.15}$$

where N is the number of atoms loaded, Φ is the atomic flux through the trapping region, $\mathcal{C}$ is the capture probability and $\mathcal{L}$ is the loss rate. This differential equation asymptotes at

$$N_{max} = \Phi\frac{\mathcal{C}}{\mathcal{L}}, \tag{5.16}$$

Minimizing the loss is possible by restricting captured atoms as those that decay to the m_j = -1/2 level of the 1S state. Due to the large hyperfine splitting of the 1S state in hydrogen, this state is off resonant with the 243.1 nm radiation by $\approx$ 0.70 GHz in the chose chosen magnetic field of 1700 Gauss (see Fig. 5.4). To calculate $\mathcal{L}$ we consider the worst case scenario for a captured atom, in which $x = 0$ and $v_z = v_y = 0$, which keeps the atom contained in most intense region of the 243.1 nm radiation. While this scenario isn't true for a dipole trap, as the spontaneous decay will give non-zero y and z velocities, it does approximate loading into a lattice where tight confinement of the standing wave wells would keep the atom trapped in the 243.1 nm interaction region. We consider any scatter or photoionization from the off resonant state a loss. Averaging the scattering probability and photoionization probability using Eq. 5.14 with $\omega_{offres} = \omega_1 + 2\pi \times 0.72 \times 10^9$ Hz, for several oscillations in the trap, we can determine the loss rate $\mathcal{L}$. This loss rate is shown in Fig. 5.7 for different laser and quenching intensities. As expected, the loss rate decreases as these two intensities decrease.

From Figs. 5.6 and 5.7, we can determine $\mathcal{C}/\mathcal{L}$, which from Eq. 5.16, tells us the number of trapped atoms we could expect for a specific atomic flux. This is shown in Fig. 5.8. As seen, with $P_{oc} < 10$ W and $\Omega_2 < 5 \times 10^9$ rad/s, is an optimal region of $\mathcal{C}/\mathcal{L} \approx 0.001$. Therefore, with atomic fluxes of $\sim 10^6$ atom/s, it would be possible to load $\sim$ 1000 atoms into the dipole trap.

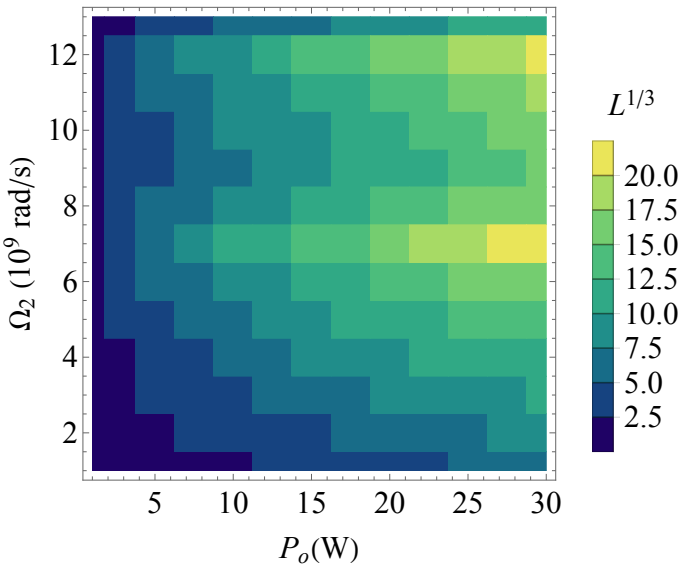

Figure 5.7: Loss rate as a function of 243.1 nm radiation and microwave quenching power. For this simulation, $\delta_1 = -1.0 \times 10^9$ s^{-1}, and $\omega_q = 21$ GHz.

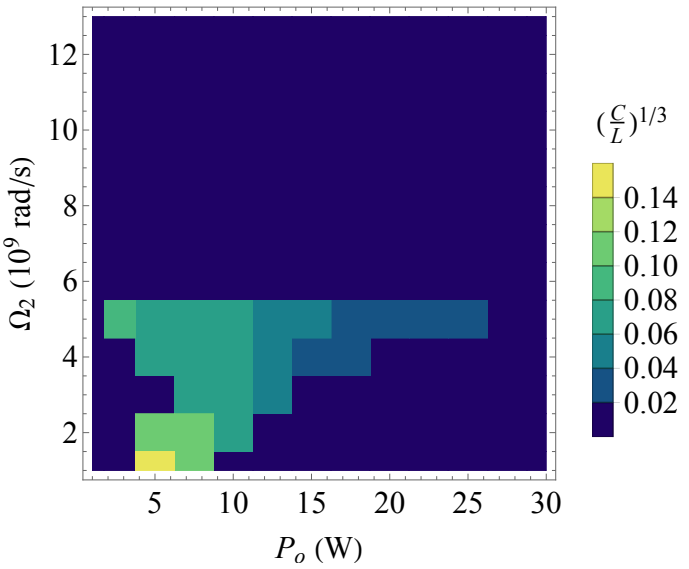

Figure 5.8: Capture to loss ratio as a function of 243.1 nm radiation and microwave quenching power. For this simulation, $\delta_1 = -1.0 \times 10^9$ s^{-1}, and $\omega_q = 21$ GHz.

5.5.2 Multiple Trajectories

The previous result was for a single trajectory passing through the center of the trapping region, so it isn't appropriate to speak about flux. Using the optimal parameters for this single trajectory; though, we can determine the capture probability over the entire trapping region by analyzing trajectories entering the trap at various values of y and z. The results are shown in Fig. 5.9

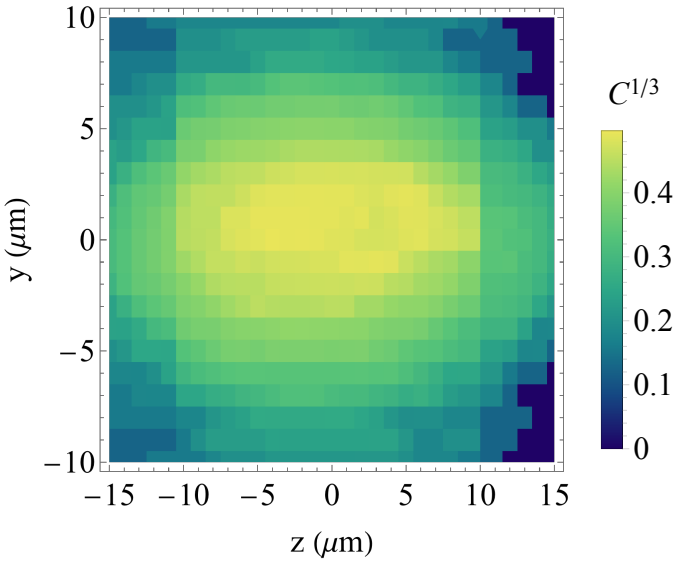

Figure 5.9: Capture rate as a function of position in the trapping region. For this simulation, $\delta_1 = -1.0\times10^9$ s^{-1}, $\omega_q = 21$ GHz, $\Omega_2 = 5.0 \times 10^9$ s^{-1}, and $P_{oc} = 10$ W.

Averaging over the trajectories in Fig. 5.9, the average capture value is $\bar{\mathcal{C}} = .04$, whereas the loss rate for the parameters here is $\mathcal{L} = 320$ s^{-1}. Therefore $\bar{\mathcal{C}}/\mathcal{L} = 0.00012$ s, requiring atom flux through the region on the order of 10^4 atoms/s in order to load more than 1 atom. This type of flux could be possible with a dilution refrigerator placed close to the trapping region. Hydrogen dilution refrigerators can have fluxes from 10^{12}-10^{15} atoms/sec at temperature of $\sim$ 0.5 K [164]. As seen in Fig. 5.10, the capture rate has a $\approx$ 2 m/s range. Using the Maxwell-Boltzmann distribution at 0.5 K, approximately 1 % of the atoms would exist between 12-14 m/s. If the dilution refrigerator was placed 1 cm away from the trapping region, the geometric overlap between a 1 cm hemisphere and trapping region of 30x20 μm is 3×10^{-6}. Taking into account that only 35 % of captured atoms decay to the off-resonant state, this would give an atom flux of $\Phi_{trap} = \Phi_{total} \times m_l \times g_l \times b_l \approx 10^4 - 10^7$ capturable atoms/sec passing through the trapping region, where Φ_{total} is the total atom flux from the dilution refrigerator, m_l is the amount of atoms in the correct velocity range, g_l is the geometric overlap, and b_l is the branching ratio to the off resonant state. This value means 1-1000 atoms could be loaded into the trap. This is the worst case scenario of the atom remaining in the 243 nm beam, which would be true for a lattice. However, in a dipole trap a captured atom will gain on average 1 m/s of velocity in the z-direction. The

Rayleigh range of the magic wavelength trap is 5 mm, and the atoms would have to travel twice this distance before it re-enters the 243 nm beam. Therefore, the ratio of time spent in the 243 nm beam versus outside would be ~ 0.005. This would therefore increase the estimates given by the worse case scenario by ~ 500, meaning 500-500,000 atoms could be trapped in the dipole trap in the best case scenario.

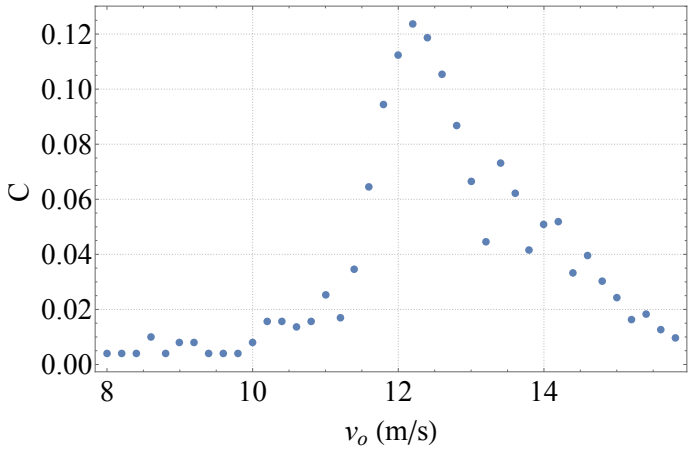

Figure 5.10: Capture rate as a function of initial velocity into the trapping region. For these simulations $\delta_1 = -1.0 \times 10^9$ s^{-1}, $\omega_q = 21$ GHz, $\Omega_2 = 5.0 \times 10^9$ s^{-1}, and $P_{oc} = 10$ W.

Another option for loading atoms into the dipole trap is modeled off of ease of implementation into the current 1S-2S setup [5]. In the current design, a 6 K atomic beam of hydrogen is approximately 30 cm from the 1S-2S spectroscopy region. In this configuration, $m_l = 5.5 \times 10^{-7}$ and $g_l = 3.3 \times 10^{-9}$. Therefore, even though atomic fluxes from the atomic beam of 10^{15}-10^{18} atoms/sec are possible, only 0-10 capturable atom/sec would pass through the trapping region. One way to increase this flux is through use of Helmholtz coils as shown in Fig. 5.11, which can slow down and focus atoms into the trapping region.

The magnitude and gradient of the magnetic field generated by these Helmholtz coils are shown in Fig. 5.12. As seen the magnitude has a maxium as the atoms approach the trapping region. Furthermore, the gradient of the field is linear in r, which means $F_r \approx -\alpha(z)\mu B_m r$, where B_m is the max magnetic field, and $\alpha(z)$ is a coefficient of the field gradient. Following [165], this behavior models that of a lens and there is an effective focal length of the coils that depends

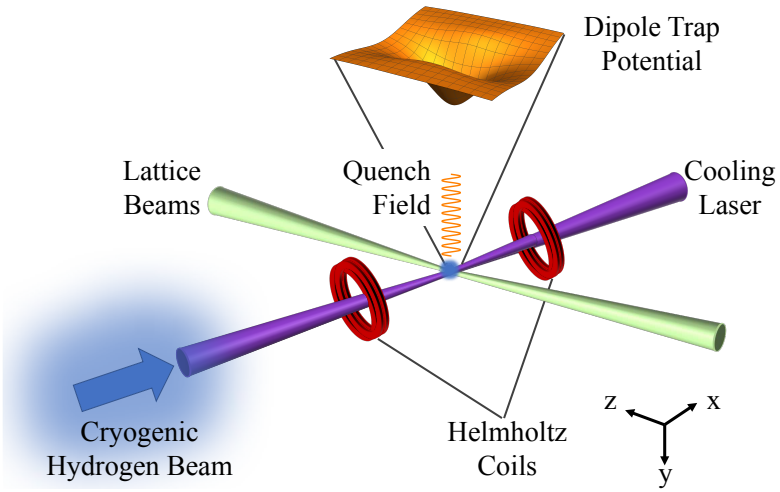

Figure 5.11: A proposed experimental setup modeled on the current 1S-2S spectroscopy set up. A cryogenic hydrogen beam will emit in the +x direction, 30 cm from the trapping region. On the way to this region, the atoms are decelerated and focused using Helmholtz coils. The focus of the desired atom velocity class atom is placed at the intersection of the foci of the dipole trap and 243 nm radiation. Here, the 243 nm radiation can remove excess kinetic energy of the atoms as they pass through the lattice wells, capturing them. A quenching field overlaps with this region in order to control the 243 nm interaction.

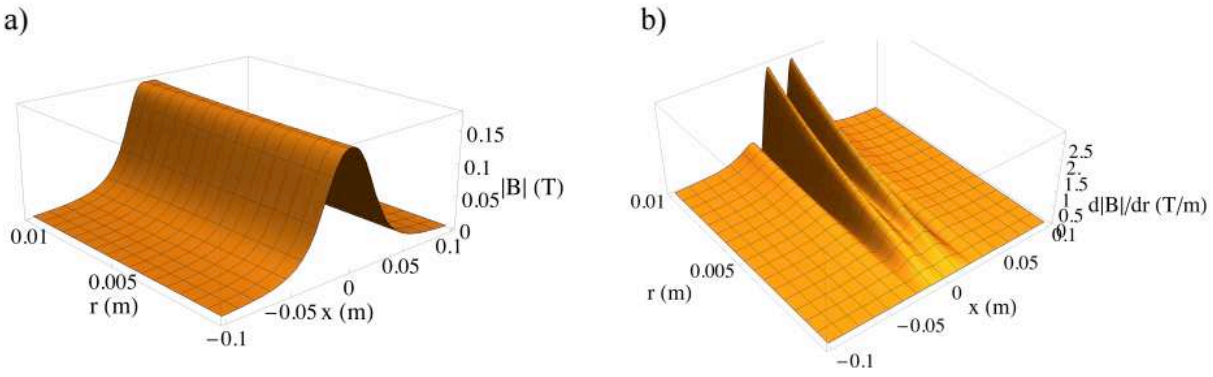

Figure 5.12: a) Magnetic field magnitude b) Magnetic field gradient

on the kinetic energy of the atoms. For these simulations we model the Helmholtz coils using a grid of magnetic field values calculated using superposition of current carrying loops with the analytic form found in [166]. The potential energy of this field can be calculated and added to the potential created by the dipole trap, thus affecting the atomic trajectory. For a radius of R = 2 cm, a length of L = 1 cm, 4 layers, a gap of R/2, and 2.5 mm diameter copper wires, 210 A of current applied to each coil creates a 0.17 T max B-field. Each current would generate 370 W of heat that

would need dissipation, which is manageable in vacuum. The coil configuration here slows atoms between 45.5-46 m/s atoms to 13-14 m/s, and focuses them 2.5 mm after the center of the coils. This configuration is arbitrary, and many other velocity classes and focal positions can be made by adjusting the coil parameters.

In Fig. 5.13(a), we see the distribution of atoms without a magnetic field that have propagated 30 cm from the discharge nozzle. The angular spread is limited to atoms contained within a 7 mm radius at this distance from the nozzle. In Fig. 5.13(b), we see the focusing effects of the Helmholtz coils, which tightly focuses the atoms from a 7 mm radius distribution to an ≈ 100 μm distribution. From this we can determine the increase in flux of atoms passing through trapping region as the ratio of these two areas as $\approx 5 \times 10^3$. In this case the flux through the trapping region is $\Phi_{trap} = \Phi_{total} \times m_l \times g_l \times b_l \times f_l$. Here, Φ_{total} is $10^{15} - 10^{18}$ atoms/s, $m_l = 9.5 \times 10^{-6}$, $g_l = 2.7 \times 10^{-4}$, and $f_l = 0.20$ is the fraction of focused atoms that pass through the trapping region. Overall, this gives 10^5-10^8 capturable atoms/sec passing through the trapping region, meaning in the worst case scenario, $\sim$ 10-10^4 atoms could be loaded, and $\sim$ $5{\times}10^3$-$5{\times}10^6$ in the best case scenario.

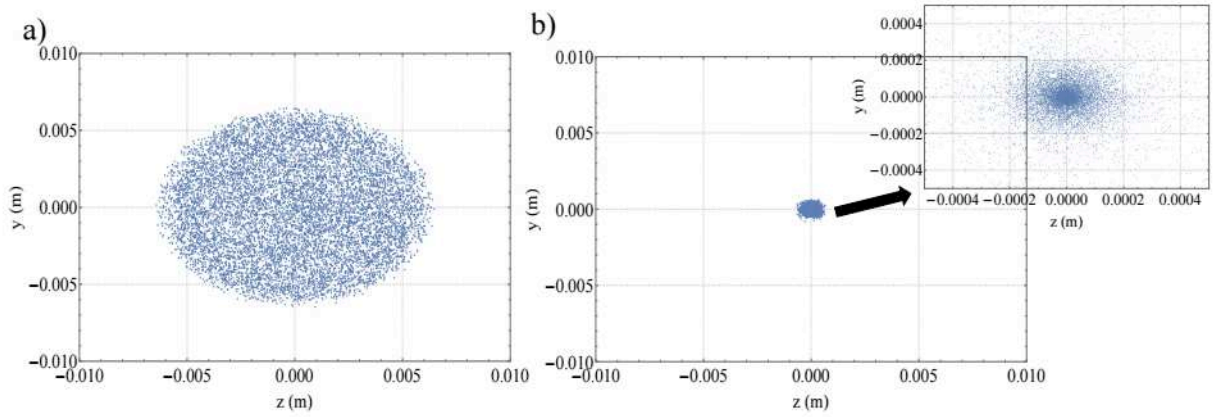

Figure 5.13: a) atomic trajectory distribution without magnetic field focusing at x = 0 m b) atomic trajectory distribution with magnetic field focusing at x = 0 m

5.6 Conclusion

We have shown through simulations that with the 243.1 nm power readily available from our laser system, hydrogen could be captured in a 1S–2S magic wavelength dipole trap with a single two-photon cooling cycle. This technique is novel to hydrogen and its large recoil velocity, and complements recent ideas and interest in capturing hydrogen and anti-hydrogen in magic wavelength optical traps [144, 167].

Accounting for loss of captured atoms from photoionization and scattering with the intense 243.1 nm cooling beam, we estimate that $\sim 10^3 - 10^6$ atoms could be loaded into a magic wavelength dipole trap with realizable cryogenic atomic sources. If we model trapped atoms as if they were tightly confined in the standing wave wells of an optical lattice, this estimate drops to $\sim 1 - 10^3$ atoms. However, to appropriately treat this method with an optical lattice would require treating the motion of hydrogen atoms quantum mechanically. This is because the de Broglie wavelength for the hydrogen atoms we treated here ($v \approx 10$ m/s) is ≈ 50 nm, which would be on the same order as the spacing between wells in a magic wavelength optical lattice of $\lambda_{magic}/2 \approx 250$ nm. An alternative to direct loading into an optical lattice would be to first capture them in a dipole trap using the methods presented here, and then retroreflect the laser creating the trap back onto itself, forming a standing wave lattice potential. While all these methods would be technically challenging to implement, these ideas should be pursued further as optical trapping of hydrogen could open the door to a new era of high precision studies of hydrogen.

Chapter 6

Summary

The hydrogen 1S–2S two-photon transition was first observed by Hänsch et al. [168]. Over the following four decades, the continued improvement in the spectroscopy of this transition has led to increasingly precise determinations of the Rydberg constant and proton charge radius—ultimately providing a stringent test of quantum electrodynamics [7]. The importance of the 1S–2S transition stems in part from the simplicity of hydrogen, which makes it amenable to theoretical study, and also from its narrow natural linewidth of only 1.3 Hz.

When reviewing the well-known measurements of the 1S–2S transition, one can also observe a continual refinement of the spectroscopy lasers used—first, by a transition from pulsed to continuous-wave (cw) lasers [28, 169] and then by an increase in power, coherence and robustness [29, 30, 42, 170, 171]. The most recent result was reported by the Hänsch group in 2011, in which they determined the transition to a fractional frequency uncertainty of 4.2×10^{15} [5]. By that time, the UV laser source had evolved to an all solid state system that produced 13 mW of 243 nm cw radiation. This radiation was then cavity enhanced to 368 mW within the hydrogen spectrometer. In addition to the impressive intracavity power, this radiation source possessed an extremely narrow linewidth of ≈ 1 Hz which is commensurate with the hydrogen 1S–2S transition width itself. More recently, in 2013, Beyer et al. [17] reported on a 243.1 nm laser which was capable of producing 75 mW before cavity enhancement and up to ≈ 1 W intracavity power through cavity enhancement.

Motivated by this long line of work, and building off these past accomplishments, we developed the high-power coherent cw 243.1 nm laser system presented in this dissertation. A notable distinction from our system versus previous systems is the use of a Yb-fiber amplifier to generate > 10 W of narrow linewidth power at 972.5 nm. Through frequency conversion, these new levels of IR power enable our system to generate > 1 W of 243.1 nm output powers. With this amount of 243.1 nm radiation, we have pushed deep-UV cavity enhancement to > 30 W of intracavity

power, and with improvements to our system, these powers should reach > 60 W. With this power, two-photon cooling a cryogenic hydrogen beam is realizable. This goal is the primary motivation behind this laser system, as a laser that could robustly cool hydrogen would serve as an invaluable tool for the high precision hydrogen spectroscopy community. As discussed extensively in Chapter 1, besides laser cooling, a frequency converted, coherent high-power laser tunable from 243–244 nm is useful in several other ways. For instance, with high power 243.1 nm radiation, the 1S–2S transition could be excited with laser beams of large transverse dimensions, which could decrease transit-time broadening and increase the proportion of atoms in the atomic beam that are excited. With the recent trapping of anti-hydrogen in its ground state, a larger beam would also prove beneficial in mitigating the difficulties created by the low number of trapped anti-hydrogen atoms available. In regards to other exotic atoms, spectroscopy of positronium and muonium would benefit from high-power 486.3 nm and 244 nm radiation, respectively, as these measurements face low detection rates and would benefit from increased laser power. Lastly, as shown in Chapter 5, a high power 243.1 nm laser offers a unique and novel method for capturing hydrogen in a magic wavelength dipole trap through a single two-photon cooling cycle.

A coherent, high-power 243.1 nm laser can also efficiently populate the metastable 2S state. Nearly all the spectroscopic transitions contributing to the proton radius puzzle are 2S–nS/P/D transitions, and would benefit from a greater flux of metastable atoms. For instance, the 2S–8S/D measurements strongly impact the determination of the proton radius due to their relatively narrow linewidth. The past measurements used a thermal hydrogen beam and electron impact to populate the 2S state. Using a cryogenic hydrogen beam and the 243.1 nm power demonstrated in this dissertation to populate the 2S state would increase statistics and reduce a large number of systematics present in the previous measurements. This is the thrust of current work in our lab, and the experimental overview is shown in Fig. 6.1. As seen in Fig. 6.1, we will use cavity enhanced 243.1 nm radiation to efficiently populate the 2S state. Therefore, the design we are implementing for these planned measurements builds heavily on what we learned in building the deep-UV enhancement cavity presented in Chapter 4.

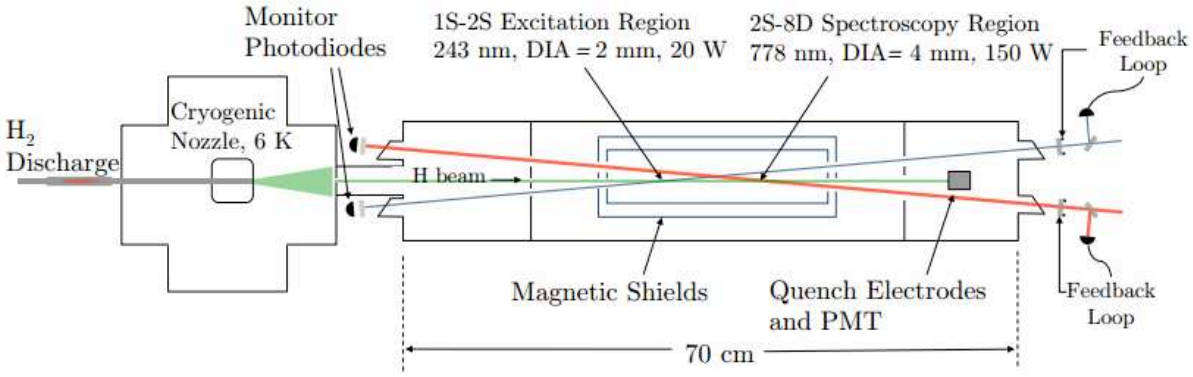

Figure 6.1: Experimental apparatus. A cryogenic atomic hydrogen beam is formed with a cold nozzle and then collimated with a series of apertures. In an evacuated region with electromagnetic field control, the atomic beam will first pass a 243.1 nm laser beam (to drive the 1S–2S transition) followed by 778 nm beam (for spectroscopy of the 2S–8S/D transitions). Both optical beams will be within power enhancement cavities. The atoms will then proceed to a detection region where the remaining 2S population is detected.

Following these 2S–8S/D measurements, the two-photon cooling setup will be developed. This will require increasing the deep-UV intracavity power from 30 to 60 W, and a non-trivial amount of work in overlapping the cryogenic hydrogen beam with the intracavity radiation. As shown in Fig. 6.2, we will use a transverse magnetic guide to overlap the cryogenic beam with the cavity enhanced 243.1 nm power. Also in this region will exist a microwave wave guide to provide the necessary mixing of the 2S and 2P states. To keep the atoms magnetically trapped, the microwave field must only mix the $2S_{1/2}$ $m_j = 1/2$ state to the $2P_{3/2}$ $m_j = 3/2$ state so that population will only decay to the $1S_{1/2}$ $m_j = 1/2$ state. This state selection is possible with the use of an axial magnetic field. Chirping the 243.1 nm frequency will keep the atoms on resonance with the radiation as they are slowed down, and the laser-cooled hydrogen can be magnetically guided out of the enhancement cavity for further tests with laser cooled hydrogen. For instance, this system could generate a high flux hydrogen beam with average velocities of $\sim$ 10 m/s, which could then be used to load a dipole trap using the method presented in Chapter 5.

While a laser cooled hydrogen beam would help mitigate the motional effects that limit spectroscopy of hydrogen, ultimately, tight spatial confinement in a magic wavelength optical trap would be the ideal solution. Capturing hydrogen in a magic wavelength dipole trap was simulated

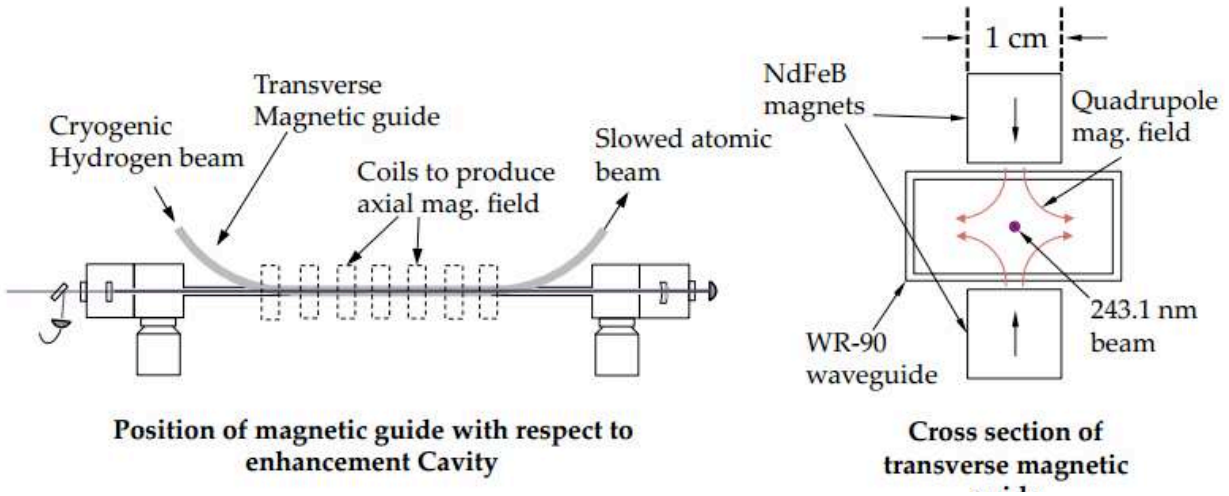

Figure 6.2: Depiction of the planned adaptation of our enhancement cavity to slow an atomic hydrogen beam within a transverse magnetic trap. The rightmost figure shows a cross section of the magnetic guide. Directly outside the waveguide we will place NdFeB magnets to produce a quadrupole transverse magnetic field which will guide the atoms and keep them overlapped with the 243.1 nm radiation. A $\sim$ 9.9 GHz microwave field will be launched in the waveguide to couple the $2S_{1/2}$ $m_j = 1/2$ and $2P_{3/2}$ $m_j = 3/2$ states and an axial magnetic field will be used to provide state selection.

in Chapter 5, and the simulation parameters were modeled on physically realizable, albeit technically challenging, experimental parameters. The experimentally feasibility of this design should be explored further, as well as its translation to trapping anti-hydrogen in the current anti-hydrogen magnetic traps. If realizable, such a result would have great scientific worth and should be pursued intensely. Confinement in an optical trap opens up the possibility of a (anti)hydrogen optical lattice clock, which could revolutionize high precision spectroscopy of (anti)hydrogen, enable a definition of time purely linked to fundamental constants, and shed light on the perplexing asymmetry between matter and anti-matter in our universe. It is clear that the future of (anti)hydrogen spectroscopy is still rich with opportunities.

Richard Feynman, one of the founders of QED, once commented: "There's a reason physicists are so successful with what they do, and that is because they study the hydrogen atom and the helium ion and then they stop [172]." While this statement is clearly a quip as scientists have achieved incredible success outside of studies of hydrogen, hydrogen has had an illustrious history. Hydrogen was pivotal in our development of quantum mechanics and QED, and through its continued tests of QED, probing of fundamental constants, and future tests of CPT symmetry, hydrogen

spectroscopy continues to fuel scientific progression. We hope the laser system and simulations presented in this dissertation aids in this progression, and we are excited to see the work done here adapted by groups interested in pushing the frontiers of precision spectroscopy on hydrogen and hydrogen-like systems.

Bibliography

[1] A. Antognini, F. Nez, K. Schuhmann, F. D. Amaro, F. Biraben, J. M. Cardoso, D. S. Covita, A. Dax, S. Dhawan, M. Diepold, *et al.*, "Proton structure from the measurement of 2S–2P transition frequencies of muonic hydrogen," *Science*, vol. 339, no. 6118, pp. 417–420, 2013.

[2] P. J. Mohr, D. B. Newell, and B. N. Taylor, "Codata recommended values of the fundamental physical constants: 2014," *Journal of Physical and Chemical Reference Data*, vol. 45, no. 4, p. 043102, 2016.

[3] F. Biraben, "Spectroscopy of atomic hydrogen," *The European Physical Journal Special Topics*, vol. 172, no. 1, pp. 109–119, 2009.

[4] C. Schwob, L. Jozefowski, B. De Beauvoir, L. Hilico, F. Nez, L. Julien, F. Biraben, O. Acef, J.-J. Zondy, and A. Clairon, "Optical frequency measurement of the 2S–12D transitions in hydrogen and deuterium: Rydberg constant and Lamb shift determinations," *Physical Review Letters*, vol. 82, no. 25, p. 4960, 1999.

[5] C. G. Parthey, A. Matveev, J. Alnis, B. Bernhardt, A. Beyer, R. Holzwarth, A. Maistrou, R. Pohl, K. Predehl, T. Udem, T. Wilken, N. Kolachevsky, M. Abgrall, D. Rovera, C. Salomon, P. Laurent, and T. W. Hänsch, "Improved measurement of the hydrogen 1S–2S transition frequency," *Physical Review Letters*, vol. 107, no. 20, p. 203001, 2011.

[6] A. Huber, T. Udem, B. Gross, J. Reichert, M. Kourogi, K. Pachucki, M. Weitz, and T. Hänsch, "Hydrogen-deuterium 1S–2S isotope shift and the structure of the deuteron," *Physical review letters*, vol. 80, no. 3, p. 468, 1998.

[7] P. J. Mohr, B. N. Taylor, and D. B. Newell, "CODATA recommended values of the fundamental physical constants: 2010," *Journal of Physical and Chemical Reference Data*, vol. 84, no. 4, p. 1527, 2012.

[8] R. Bluhm, V. A. Kostelecký, and N. Russell, "CPT and Lorentz tests in hydrogen and antihydrogen," *Physical Review Letters*, vol. 82, no. 11, p. 2254, 1999.

[9] G. Gabrielse, P. Larochelle, D. Le Sage, B. Levitt, W. Kolthammer, R. McConnell, P. Richerme, J. Wrubel, A. Speck, M. George, *et al.*, "Antihydrogen production within a Penning-Ioffe trap," *Physical review letters*, vol. 100, no. 11, p. 113001, 2008.

[10] G. Gabrielse, R. Kalra, W. Kolthammer, R. McConnell, P. Richerme, D. Grzonka, W. Oelert, T. Sefzick, M. Zielinski, D. Fitzakerley, *et al.*, "Trapped antihydrogen in its ground state," *Physical Review Letters*, vol. 108, no. 11, p. 113002, 2012.

[11] G. B. Andersen, M. Ashkezari, M. Baquero-Ruiz, W. Bertsche, P. D. Bowe, E. Butler, C. Cesar, M. Charlton, A. Deller, S. Eriksson, *et al.*, "Confinement of antihydrogen for 1,000 seconds," *Nature Physics*, vol. 7, no. 7, p. 558, 2011.

[12] M. Ahmadi, B. X. R. Alves, C. Baker, W. Bertsche, E. Butler, A. Capra, C. Carruth, C. Cesar, M. Charlton, S. Cohen, *et al.*, "Observation of the 1S–2S transition in trapped antihydrogen," *Nature*, vol. 541, no. 7638, p. 506, 2017.

[13] W. D. Phillips, "Nobel lecture: Laser cooling and trapping of neutral atoms," *Reviews of Modern Physics*, vol. 70, no. 3, p. 721, 1998.

[14] A. D. Ludlow, M. M. Boyd, J. Ye, E. Peik, and P. O. Schmidt, "Optical atomic clocks," *Reviews of Modern Physics*, vol. 87, no. 2, p. 637, 2015.

[15] B. Bloom, T. Nicholson, J. Williams, S. Campbell, M. Bishof, X. Zhang, W. Zhang, S. Bromley, and J. Ye, "An optical lattice clock with accuracy and stability at the 10^{-18} level," *Nature*, vol. 506, no. 7486, p. 71, 2014.

[16] D. Berkeland, E. Hinds, and M. Boshier, "Precise optical measurement of Lamb shifts in atomic hydrogen," *Physical review letters*, vol. 75, no. 13, p. 2470, 1995.

[17] A. Beyer, J. Alnis, K. Khabarova, A. Matveev, C. G. Parthey, D. C. Yost, R. Pohl, T. Udem, T. W. Hänsch, and N. Kolachevsky, "Precision spectroscopy of the 2S–4P transition in atomic hydrogen on a cryogenic beam of optically excited 2S atoms," *Annalen der Physik*, vol. 525, no. 8-9, pp. 671–679.

[18] J. Flowers, H. Klein, and H. Margolis, "Hydrogenic systems, frequency standards and fundamental constants," *Contemporary Physics*, vol. 45, no. 2, pp. 123–145, 2004.

[19] J. Flowers, "The route to atomic and quantum standards," *Science*, vol. 306, no. 5700, pp. 1324–1330, 2004.

[20] R. Hilbig and R. Wallenstein, "Enhanced production of tunable VUV radiation by phase-matched frequency tripling in krypton and xenon," *IEEE Journal of Quantum Electronics*, vol. 17, no. 8, pp. 1566–1573, 1981.

[21] K. S. Eikema, J. Walz, and T. Hänsch, "Continuous coherent Lyman-α excitation of atomic hydrogen," *Physical Review Letters*, vol. 86, no. 25, p. 5679, 2001.

[22] I. D. Setija, H. G. C. Werij, O. J. Luiten, M. W. Reynolds, T. W. Hijmans, and J. T. M. Walraven, "Optical cooling of atomic hydrogen in a magnetic trap," *Phys. Rev. Lett.*, vol. 70, no. 15, pp. 2257–2260, 1993.

[23] M. Allegrini and E. Arimondo, "Pulsed laser cooling of hydrogen atoms," *Physics Letters A*, vol. 172, no. 4, pp. 271–276, 1993.

[24] V. Zehnlé and J. C. Garreau, "Continuous-wave Doppler cooling of hydrogen atoms with two-photon transitions," *Physical Review A*, vol. 63, no. 2, p. 021402, 2001.

[25] D. Kielpinski, "Laser cooling of atoms and molecules with ultrafast pulses," *Physical Review A*, vol. 73, no. 6, p. 063407, 2006.

[26] S. Wu, R. C. Brown, W. D. Phillips, and J. Porto, "Pulsed Sisyphus scheme for laser cooling of atomic (anti) hydrogen," *Physical review letters*, vol. 106, no. 21, p. 213001, 2011.

[27] M. Haas, U. D. Jentschura, C. H. Keitel, N. Kolachevsky, M. Herrmann, P. Fendel, M. Fischer, T. Udem, R. Holzwarth, T. Hänsch, *et al.*, "Two-photon excitation dynamics in bound two-body Coulomb systems including AC Stark shift and ionization," *Physical Review A*, vol. 73, no. 5, p. 052501, 2006.

[28] B. Couillaud, T. Hänsch, and S. MacLean, "High power CW sum-frequency generation near 243 nm using two intersecting enhancement cavities," *Optics communications*, vol. 50, no. 2, pp. 127–129, 1984.

[29] C. Zimmermann, V. Vuletic, A. Hemmerich, and T. Hänsch, "All solid state laser source for tunable blue and ultraviolet radiation," *Applied physics letters*, vol. 66, no. 18, pp. 2318–2320, 1995.

[30] N. Kolachevsky, J. Alnis, S. D. Bergeson, and T. Hänsch, "Compact solid-state laser source for 1S–2S spectroscopy in atomic hydrogen," *Physical Review A*, vol. 73, no. 2, p. 021801, 2006.

[31] S. G. Karshenboim, "Precision physics of simple atoms: QED tests, nuclear structure and fundamental constants," *Physics Reports*, vol. 422, no. 1-2, pp. 1–63, 2005.

[32] P. Crivelli, "The Mu-MASS (muonium laser spectroscopy) experiment," *Hyperfine Interactions*, vol. 239, p. 49, Nov 2018.

[33] R. Pohl, A. Antognini, F. Nez, F. D. Amaro, F. Biraben, J. M. Cardoso, D. S. Covita, A. Dax, S. Dhawan, L. M. Fernandes, *et al.*, "The size of the proton," *Nature*, vol. 466, no. 7303, p. 213, 2010.

[34] B. De Beauvoir, F. Nez, L. Julien, B. Cagnac, F. Biraben, D. Touahri, L. Hilico, O. Acef, A. Clairon, and J. Zondy, "Absolute frequency measurement of the 2S–8S/D transitions in hydrogen and deuterium: New determination of the Rydberg constant," *Physical Review Letters*, vol. 78, no. 3, p. 440, 1997.

[35] F. Nez, M. Plimmer, S. Bourzeix, L. Julien, F. Biraben, R. Felder, Y. Millerioux, and P. De Natale, "First pure frequency measurement of an optical transition in atomic hydrogen: Better determination of the Rydberg constant," *EPL (Europhysics Letters)*, vol. 24, no. 8, p. 635, 1993.

[36] F. Biraben, J. Garreau, L. Julien, and M. Allegrini, "A metastable hydrogen atomic beam: Construction and characteristics," *Review of scientific instruments*, vol. 61, no. 5, pp. 1468–1473, 1990.

[37] L. Nagli, M. Gaft, Y. Fleger, and M. Rosenbluh, "Absolute Raman cross-sections of some explosives: Trend to UV," *Optical Materials*, vol. 30, no. 11, pp. 1747–1754, 2008.

[38] J. Sakuma, Y. Asakawa, and M. Obara, "Generation of 5-W deep-UV continuous-wave radiation at 266 nm by an external cavity with a $CsLiB_6O_{10}$ crystal," *Optics Letters*, vol. 29, no. 1, pp. 92–94, 2004.

[39] S. A. Asher, R. W. Bormett, X. G. Chen, D. H. Lemmon, N. Cho, P. Peterson, M. Arrigoni, L. Spinelli, and J. Cannon, "UV resonance Raman spectroscopy using a new CW laser source: convenience and experimental simplicity," *Applied Spectroscopy*, vol. 47, no. 5, pp. 628–633, 1993.

[40] J. H. Seo, J. H. Park, S. Kim, B. Park, Z. Ma, J. Choi, and B. K. Ju, "Nanopatterning by laser interference lithography: applications to optical devices," *Journal of Nanoscience and Nanotechnology*, vol. 14, no. 2, pp. 1521–1532, 2014.

[41] C. Lu and R. Lipson, "Interference lithography: A powerful tool for fabricating periodic structures," *Laser & Photonics Reviews*, vol. 4, no. 4, pp. 568–580, 2010.

[42] N. Kolachevsky, J. Alnis, C. G. Parthey, A. Matveev, R. Landig, and T. Hänsch, "Low phase noise diode laser oscillator for 1S–2S spectroscopy in atomic hydrogen," *Optics letters*, vol. 36, no. 21, pp. 4299–4301, 2011.

[43] F. Roeser, C. Jauregui, J. Limpert, and A. Tunnermann, "94 W 980 nm high brightness Yb-doped fiber laser," *Optics Express*, vol. 16, no. 22, pp. 17310–17318, 2008.

[44] J. Boullet, Y. Zaouter, R. Desmarchelier, M. Cazaux, F. Salin, J. Saby, R. Bello-Doua, and E. Cormier, "High power ytterbium-doped rod-type three-level photonic crystal fiber laser," *Optics Express*, vol. 16, no. 22, pp. 17891–17902, 2008.

[45] X. Zhu, W. Shi, J. Zong, D. Nguyen, R. A. Norwood, A. Chavez-Pirson, and N. Peyghambarian, "976 nm single-frequency distributed Bragg reflector fiber laser," *Optics letters*, vol. 37, no. 20, pp. 4167–4169, 2012.

[46] J. Wu, X. Zhu, H. Wei, K. Wiersma, M. Li, J. Zong, A. Chavez-Pirson, V. Temyanko, L. LaComb, R. Norwood, *et al.*, "Power scalable 10 W 976 nm single-frequency linearly polarized laser source," *Optics letters*, vol. 43, no. 4, pp. 951–954, 2018.

[47] J. Yi, Y. Fan, and S. Huang, "Study of short-wavelength Yb-fiber laser," *IEEE Photonics Journal*, vol. 4, no. 6, pp. 2278–2284, 2012.

[48] A. Schawlow and C. Townes, "Infrared and optical masers," *Physical Review*, vol. 112, no. 6, p. 1940, 1958.

[49] T. Maiman, "Stimulated optical radiation in ruby," *Nature*, vol. 187, pp. 493–494, 1960.

[50] E. Snitzer, "Proposed fiber cavities for optical masers," *Journal of Applied Physics*, vol. 32, no. 1, pp. 36–39, 1961.

[51] E. Snitzer, "Optical maser action of Nd^{+3} in a barium crown glass," *Physical Review Letters*, vol. 7, no. 12, p. 444, 1961.

[52] B. Judd, "Optical absorption intensities of rare-earth ions," *Physical review*, vol. 127, no. 3, p. 750, 1962.

[53] G. Ofelt, "Intensities of crystal spectra of rare-earth ions," *The Journal of Chemical Physics*, vol. 37, no. 3, pp. 511–520, 1962.

[54] G. H. Dieke and H. Crosswhite, "The spectra of the doubly and triply ionized rare-earths," *Applied optics*, vol. 2, no. 7, pp. 675–686, 1963.

[55] L. Johnson, "Optical maser characteristics of rare-earth ions in crystals," *Journal of Applied Physics*, vol. 34, no. 4, pp. 897–909, 1963.

[56] H. Etzel, H. Gandy, and R. Ginther, "Stimulated emission of infrared radiation from ytterbium activated silicate glass," *Applied Optics*, vol. 1, no. 4, pp. 534–536, 1962.

[57] C. J. Koester and E. Snitzer, "Amplification in a fiber laser," *Applied optics*, vol. 3, no. 10, pp. 1182–1186, 1964.

[58] J. Stone and C. Burrus, "Neodymium-doped silica lasers in end-pumped fiber geometry," *Applied Physics Letters*, vol. 23, no. 7, pp. 388–389, 1973.

[59] J. Stone and C. Burrus, "Neodymium-doped fiber lasers: room temperature cw operation with an injection laser pump," *Applied optics*, vol. 13, no. 6, pp. 1256–1258, 1974.

[60] R. Mears, L. Reekie, S. Poole, and D. Payne, "Neodymium-doped silica single-mode fibre lasers," *Electronics letters*, vol. 21, no. 17, pp. 738–740, 1985.

[61] S. Poole, D. N. Payne, and M. Fermann, "Fabrication of low-loss optical fibres containing rare-earth ions," *Electronics Letters*, vol. 21, no. 17, pp. 737–738, 1985.

[62] J. Townsend, S. Poole, and D. Payne, "Solution-doping technique for fabrication of rare-earth-doped optical fibres," *Electronics letters*, vol. 23, no. 7, pp. 329–331, 1987.

[63] R. J. Mears, L. Reekie, I. Jauncey, and D. N. Payne, "Low-noise erbium-doped fibre amplifier operating at 1.54 μm," *Electronics Letters*, vol. 23, no. 19, pp. 1026–1028, 1987.

[64] E. Desurvire, J. R. Simpson, and P. Becker, "High-gain erbium-doped traveling-wave fiber amplifier," *Optics Letters*, vol. 12, no. 11, pp. 888–890, 1987.

[65] R. Mears, L. Reekie, S. Poole, and D. Payne, "Low-threshold tunable CW and Q-switched fibre laser operating at 1.55 μm," *Electronics Letters*, vol. 22, no. 3, pp. 159–160, 1986.

[66] E. Snitzer, "Rare earth fiber lasers," *Journal of the Less Common Metals*, vol. 148, no. 1-2, pp. 45–58, 1989.

[67] D. Hanna, R. Percival, I. Perry, R. Smart, P. Suni, J. Townsend, and A. Tropper, "Continuous-wave oscillation of a monomode ytterbium-doped fibre laser," *Electronics Letters*, vol. 24, no. 17, pp. 1111–1113, 1988.

[68] D. Hanna, R. Percival, I. Perry, R. Smart, P. Suni, and A. Tropper, "An ytterbium-doped monomode fibre laser: Broadly tunable operation from 1.010 μm to 1.162 μm and three-level operation at 974 nm," *Journal of modern Optics*, vol. 37, no. 4, pp. 517–525, 1990.

[69] S. Magne, M. Druetta, J.-P. Goure, J. C. Thevenin, P. Ferdinand, and G. Monnom, "An ytterbium-doped monomode fiber laser: amplified spontaneous emission, modeling of the gain and tunability in an external cavity," *Journal of Luminescence*, vol. 60, pp. 647–650, 1994.

[70] C. Mackechnie, W. Barnes, D. Hanna, and J. Townsend, "High power ytterbium Yb^{+3}-doped fibre laser operating in the 1-1.2 μm region," *Electronics Letters*, vol. 29, no. 1, pp. 52–53, 1993.

[71] J. Allain, M. Monerie, H. Poignant, and T. Georges, "High-efficiency ytterbium-doped fluoride fibre laser," *Journal of Non-Crystalline Solids*, vol. 161, pp. 270–273, 1993.

[72] H. Pask, R. J. Carman, D. C. Hanna, A. C. Tropper, C. J. Mackechnie, P. R. Barber, and J. M. Dawes, "Ytterbium-doped silica fiber lasers: versatile sources for the 1-1.2 μm region," *IEEE Journal of Selected Topics in Quantum Electronics*, vol. 1, no. 1, pp. 2–13, 1995.

[73] R. Paschotta, J. Nilsson, A. C. Tropper, and D. C. Hanna, "Ytterbium-doped fiber amplifiers," *IEEE Journal of quantum electronics*, vol. 33, no. 7, pp. 1049–1056, 1997.

[74] J. G. Endriz, M. Vakili, G. S. Browder, M. Devito, J. M. Haden, G. L. Harnagel, W. Plano, M. Sakamoto, D. F. Welch, S. Willing, *et al.*, "High power diode laser arrays," *IEEE Journal of quantum electronics*, vol. 28, no. 4, pp. 952–965, 1992.

[75] R. Maurer, "Optical waveguide light source. US Patent 3,808,549," 1974.

[76] E. Snitzer, H. Po, F. Hakimi, R. Tumminelli, and B. McCollum, "Double clad, offset core Nd fiber laser," in *Optical fiber sensors*, p. PD5, Optical Society of America, 1988.

[77] S. Bedö, W. Lüthy, and H. Weber, "The effective absorption coefficient in double-clad fibres," *Optics communications*, vol. 99, no. 5-6, pp. 331–335, 1993.

[78] A. Liu and K. Ueda, "The absorption characteristics of circular, offset, and rectangular double-clad fibers," *Optics Communications*, vol. 132, no. 5-6, pp. 511–518, 1996.

[79] V. Doya, O. Legrand, and F. Mortessagne, "Optimized absorption in a chaotic double-clad fiber amplifier," *Optics letters*, vol. 26, no. 12, pp. 872–874, 2001.

[80] D. Kouznetsov, J. V. Moloney, and E. M. Wright, "Efficiency of pump absorption in double-clad fiber amplifiers. I. Fiber with circular symmetry," *JOSA B*, vol. 18, no. 6, pp. 743–749, 2001.

[81] D. Kouznetsov and J. V. Moloney, "Efficiency of pump absorption in double-clad fiber amplifiers. II. Broken circular symmetry," *JOSA B*, vol. 19, no. 6, pp. 1259–1263, 2002.

[82] H. Pask, J. Archambault, D. Hanna, L. Reekie, P. S. J. Russell, J. Townsend, and A. Tropper, "Operation of cladding-pumped Yb^{3+}-doped silica fibre lasers in 1 μm region," *Electronics letters*, vol. 30, no. 11, pp. 863–865, 1994.

[83] V. Dominic, S. MacCormack, R. Waarts, S. Sanders, S. Bicknese, R. Dohle, E. Wolak, P. Yeh, and E. Zucker, "110 W fibre laser," *Electronics Letters*, vol. 35, no. 14, pp. 1158–1160, 1999.

[84] Y. e. Jeong, J. Sahu, D. Payne, and J. Nilsson, "Ytterbium-doped large-core fiber laser with 1.36 kW continuous-wave output power," *Optics express*, vol. 12, no. 25, pp. 6088–6092, 2004.

[85] V. Gapontsev, V. Fomin, A. Ferin, and M. Abramov, "Diffraction limited ultra-high-power fiber lasers," in *Advanced Solid-State Photonics*, p. AWA1, Optical Society of America, 2010.

[86] F. Roser, J. Rothhard, B. Ortac, A. Liem, O. Schmidt, T. Schreiber, J. Limpert, and A. Tunnermann, "131 W 220 fs fiber laser system," *Optics Letters*, vol. 30, no. 20, pp. 2754–2756, 2005.

[87] T. Eidam, S. Hanf, E. Seise, T. V. Andersen, T. Gabler, C. Wirth, T. Schreiber, J. Limpert, and A. Tünnermann, "Femtosecond fiber CPA system emitting 830 W average output power," *Optics letters*, vol. 35, no. 2, pp. 94–96, 2010.

[88] D. Richardson, J. Nilsson, and W. Clarkson, "High power fiber lasers: current status and future perspectives," *JOSA B*, vol. 27, no. 11, pp. B63–B92, 2010.

[89] C. Jauregui, J. Limpert, and A. Tünnermann, "High-power fibre lasers," *Nature photonics*, vol. 7, no. 11, p. 861, 2013.

[90] M. N. Zervas and C. A. Codemard, "High power fiber lasers: a review," *IEEE Journal of selected topics in Quantum Electronics*, vol. 20, no. 5, pp. 219–241, 2014.

[91] J. J. Koponen, M. J. Söderlund, H. J. Hoffman, and S. K. Tammela, "Measuring photodarkening from single-mode ytterbium doped silica fibers," *Optics Express*, vol. 14, no. 24, pp. 11539–11544, 2006.

[92] J. Koponen, M. Söderlund, H. J. Hoffman, D. Kliner, and J. Koplow, "Photodarkening measurements in large mode area fibers," in *Fiber Lasers IV: Technology, Systems, and Applications*, vol. 6453, p. 64531E, International Society for Optics and Photonics, 2007.

[93] R. Paschotta, J. Nilsson, P. Barber, J. Caplen, A. C. Tropper, and D. C. Hanna, "Lifetime quenching in Yb-doped fibres," *Optics Communications*, vol. 136, no. 5-6, pp. 375–378, 1997.

[94] M. Engholm, L. Norin, and D. Åberg, "Strong UV absorption and visible luminescence in ytterbium-doped aluminosilicate glass under UV excitation," *Optics letters*, vol. 32, no. 22, pp. 3352–3354, 2007.

[95] M. Engholm and L. Norin, "Preventing photodarkening in ytterbium-doped high power fiber lasers; correlation to the UV-transparency of the core glass," *Optics express*, vol. 16, no. 2, pp. 1260–1268, 2008.

[96] S. Yoo, C. Basu, A. Boyland, C. Sones, J. Nilsson, J. Sahu, and D. Payne, "Photodarkening in Yb-doped aluminosilicate fibers induced by 488 nm irradiation," *Optics letters*, vol. 32, no. 12, pp. 1626–1628, 2007.

[97] P. D. Dragic, C. G. Carlson, and A. Croteau, "Characterization of defect luminescence in Yb doped silica fibers: part I NBOHC," *Optics express*, vol. 16, no. 7, pp. 4688–4697, 2008.

[98] Y.-S. Liu, T. Galvin, T. Hawkins, J. Ballato, L. Dong, P. Foy, P. Dragic, and J. Eden, "Linkage of oxygen deficiency defects and rare earth concentrations in silica glass optical fiber probed by ultraviolet absorption and laser excitation spectroscopy," *Optics express*, vol. 20, no. 13, pp. 14494–14507, 2012.

[99] M. Engholm and L. Norin, "Reduction of photodarkening in Yb/Al-doped fiber lasers," in *Fiber Lasers V: Technology, Systems, and Applications*, vol. 6873, p. 68731E, International Society for Optics and Photonics, 2008.

[100] M. Engholm, P. Jelger, F. Laurell, and L. Norin, "Improved photodarkening resistivity in ytterbium-doped fiber lasers by cerium codoping," *Optics letters*, vol. 34, no. 8, pp. 1285–1287, 2009.

[101] S. Rydberg and M. Engholm, "Experimental evidence for the formation of divalent ytterbium in the photodarkening process of Yb-doped fiber lasers," *Optics express*, vol. 21, no. 6, pp. 6681–6688, 2013.

[102] S. Jetschke, S. Unger, A. Schwuchow, M. Leich, and J. Kirchhof, "Efficient Yb laser fibers with low photodarkening by optimization of the core composition," *Optics Express*, vol. 16, no. 20, pp. 15540–15545, 2008.

[103] R. Royon, J. Lhermite, L. Sarger, and E. Cormier, "High power, continuous-wave ytterbium-doped fiber laser tunable from 976 to 1120 nm," *Optics Express*, vol. 21, no. 11, pp. 13818–13823, 2013.

[104] R. Selvas, J. Sahu, L. Fu, J. Jang, J. Nilsson, A. Grudinin, K. Ylä-Jarkko, S. Alam, P. Turner, and J. Moore, "High-power, low-noise, Yb-doped, cladding-pumped, three-level fiber sources at 980 nm," *Optics Letters*, vol. 28, no. 13, pp. 1093–1095, 2003.

[105] L. Zenteno, J. Minelly, A. Liu, A. Ellison, S. Crigler, D. Walton, D. Kuksenkov, and M. Dejneka, "1 W single-transverse-mode Yb-doped double-clad fibre laser at 978 nm," *Electronics Letters*, vol. 37, no. 13, pp. 819–820, 2001.

[106] L. Fu, M. Ibsen, D. Richardson, and D. Payne, "977 nm all-fiber DFB laser," *IEEE photonics technology letters*, vol. 16, no. 11, pp. 2442–2444, 2004.

[107] Z. Huang, H. Deng, C. Yang, Q. Zhao, Y. Zhang, Y. Zhang, Z. Feng, Z. Yang, M. Peng, and S. Xu, "Self-injection locked and semiconductor amplified ultrashort cavity single-frequency Yb^{3+}-doped phosphate fiber laser at 978 nm," *Optics Express*, vol. 25, no. 2, pp. 1535–1541, 2017.

[108] V. Pureur, L. Bigot, G. Bouwmans, Y. Quiquempois, M. Douay, and Y. Jaouen, "Ytterbium-doped solid core photonic bandgap fiber for laser operation around 980 nm," *Applied Physics Letters*, vol. 92, no. 6, p. 061113, 2008.

[109] R. E. Ryan, L. A. Westling, R. Blümel, and H. J. Metcalf, "Two-photon spectroscopy: A technique for characterizing diode-laser noise," *Physical Review A*, vol. 52, no. 4, p. 3157, 1995.

[110] J. Alnis, A. Matveev, N. Kolachevsky, T. Udem, and T. Hänsch, "Subhertz linewidth diode lasers by stabilization to vibrationally and thermally compensated ultralow-expansion glass Fabry-Pérot cavities," *Physical Review A*, vol. 77, no. 5, p. 053809, 2008.

[111] A. Brandt, S. Cooper, Z. Burkley, and D. Yost, "Reduced phase noise in an erbium frequency comb via intensity noise suppression," *Optics express*, vol. 25, no. 15, pp. 18175–18181, 2017.

[112] J. Hall and M. Zhu, "An introduction to phase-stable optical sources," in *Laser Manipulation of Atoms and Ions* (E. Arimondo, W. D. Phillips, and F. Strumia, eds.), pp. 671–701, 1992.

[113] E. D. Black, "An introduction to Pound–Drever–Hall laser frequency stabilization," *American journal of physics*, vol. 69, no. 1, pp. 79–87, 2001.

[114] Z. Burkley, C. Rasor, S. Cooper, A. Brandt, and D. Yost, "Yb fiber amplifier at 972.5 nm with frequency quadrupling to 243.1 nm," *Applied Physics B*, vol. 123, no. 1, p. 5, 2017.

[115] Z. Burkley, A. D. Brandt, C. Rasor, S. F. Cooper, and D. C. Yost, "Highly coherent, watt-level deep-UV radiation via a frequency-quadrupled Yb-fiber laser system," *Appl. Opt.*, vol. 58, pp. 1657–1661, Mar 2019.

[116] M. Lukowski, C. Hessenius, and M. Fallahi, "Widely tunable high-power two-color VECSELs for new wavelength generation," *IEEE Journal of Selected Topics in Quantum Electronics*, vol. 21, no. 1, pp. 432–439, 2015.

[117] D. A. Cooke, P. Crivelli, J. Alnis, A. Antognini, B. Brown, S. Friedreich, A. Gabard, T. W. Hänsch, K. Kirch, A. Rubbia, and V. Vrankovic, "Observation of positronium annihilation in the 2S state: towards a new measurement of the 1S–2S transition frequency," *Hyperfine Interactions*, vol. 233, no. 1-3, pp. 67–73, 2015.

[118] R. W. Boyd, *Nonlinear optics*. Elsevier, 2003.

[119] e. P. Franken, A. E. Hill, C. e. Peters, and G. Weinreich, "Generation of optical harmonics," *Physical Review Letters*, vol. 7, no. 4, p. 118, 1961.

[120] G. Boyd and D. Kleinman, "Parametric interaction of focused Gaussian light beams," *Journal of Applied Physics*, vol. 39, no. 8, pp. 3597–3639, 1968.

[121] G. Boyd, A. Ashkin, J. Dziedzic, and D. Kleinman, "Second-harmonic generation of light with double refraction," *Physical Review*, vol. 137, no. 4A, p. A1305, 1965.

[122] Y. Mori, I. Kuroda, S. Nakajima, T. Sasaki, and S. Nakai, "New nonlinear optical crystal: cesium lithium borate," *Applied physics letters*, vol. 67, no. 13, pp. 1818–1820, 1995.

[123] N. Umemura and K. Kato, "Ultraviolet generation tunable to 0.185 μm in $CsLiB_6O_{10}$," *Applied optics*, vol. 36, no. 27, pp. 6794–6796, 1997.

[124] R. Smith, K. Nassau, and M. Galvin, "Efficient continuous optical second-harmonic generation," *Applied Physics Letters*, vol. 7, no. 10, pp. 256–258, 1965.

[125] J. Geusic, H. J. Levinstein, J. Rubin, S. Singh, and L. Van Uitert, "The nonlinear optical properties of $Ba_2NaNb_5O_{15}$," *Applied Physics Letters*, vol. 11, no. 9, pp. 269–271, 1967.

[126] A. Ashkin, G. Boyd, and J. Dziedzic, "Resonant optical second harmonic generation and mixing," *IEEE Journal of quantum electronics*, vol. 2, no. 6, pp. 109–124, 1966.

[127] R. Smith, "Theory of intracavity optical second-harmonic generation," *IEEE Journal of Quantum Electronics*, vol. 6, no. 4, pp. 215–223, 1970.

[128] R. Le Targat, J.-J. Zondy, and P. Lemonde, "75%-efficiency blue generation from an intracavity PPKTP frequency doubler," *Optics Communications*, vol. 247, no. 4-6, pp. 471–481, 2005.

[129] E. S. Polzik and H. J. Kimble, "Frequency doubling with $KNbO_3$ in an external cavity," *Optics Letters*, vol. 16, no. 18, pp. 1400–1402, 1991.

[130] J. T. Verdeyen, *Laser electronics*. Pearson, 1995.

[131] X. Wang, G. Hu, Y. Li, and J. Yao, "Numerical analysis of beam parameters and stability regions in a folded or ring cavity," *JOSA A*, vol. 11, no. 8, pp. 2265–2270, 1994.

[132] K. Kato, "Temperature-tuned 90° phase-matching properties of LiB_3O_5," *IEEE journal of quantum electronics*, vol. 30, no. 12, pp. 2950–2952, 1994.

[133] D. C. Gerstenberger, T. M. Trautmann, and M. S. Bowers, "Noncritically phase-matched second-harmonic generation in cesium lithium borate," *Optics letters*, vol. 28, no. 14, pp. 1242–1244, 2003.

[134] J. Sakuma, Y. Asakawa, and M. Obara, "Generation of 5-W deep-UV continuous-wave radiation at 266 nm by an external cavity with a $CsLiB_6O_{10}$ crystal," *Optics Letters*, vol. 29, no. 1, pp. 92–94, 2004.

[135] Y. Kaneda, J. M. Yarborough, L. Li, N. Peyghambarian, L. Fan, C. Hessenius, M. Fallahi, J. Hader, J. V. Moloney, Y. Honda, M. Nishioka, Y. Shimizu, K. Miyazono, H. Shimatani, M. Yoshimura, Y. Mori, Y. Kitaoka, and T. Sasaki, "Continuous-wave all-solid-state 244 nm deep-ultraviolet laser source by fourth-harmonic generation of an optically pumped semiconductor laser using $CsLiB_6O_{10}$ in an external resonator," *Optics Letters*, vol. 33, no. 15, pp. 1705–1707, 2008.

[136] J. Sakuma, Y. Asakawa, T. Sumiyoshi, and H. Sekita, "High-power CW deep-UV coherent light sources around 200 nm based on external resonant sum-frequency mixing," *IEEE Journal of Selected Topics in Quantum Electronics*, vol. 10, no. 6, pp. 1244–1251, 2004.

[137] K. Takachiho, M. Yoshimura, Y. Takahashi, M. Imade, T. Sasaki, and Y. Mori, "Ultraviolet laser-induced degradation of $CsLiB_6O_{10}$ and β-BaB_2O_4," *Optical Materials Express*, vol. 4, no. 3, pp. 559–567, 2014.

[138] Y. Kaneda, J. M. Yarborough, Y. Merzlyak, A. Yamaguchi, K. Hayashida, N. Ohmae, and H. Katori, "Continuous-wave, single-frequency 229 nm laser source for laser cooling of cadmium atoms," *Optics Letters*, vol. 41, no. 4, pp. 705–708, 2016.

[139] R. Zhao, X. Fu, L. Zhang, S. Fang, J. Sun, Y. Feng, Z. Xu, and Y. Wang, "High-power continuous-wave narrow-linewidth 253.7 nm deep-ultraviolet laser," *Applied Optics*, vol. 56, no. 32, pp. 8973–8977, 2017.

[140] D. Gangloff, M. Shi, T. Wu, A. Bylinskii, B. Braverman, M. Gutierrez, R. Nichols, J. Li, K. Aichholz, M. Cetina, L. Karpa, B. Jelenković, I. Chuang, and V. Vuletić, "Preventing and reversing vacuum-induced optical losses in high-finesse tantalum (V) oxide mirror coatings," *Opt. Express*, vol. 23, pp. 18014–18028, Jul 2015.

[141] R. R. Kunz, V. Liberman, and D. K. Downs, "Experimentation and modeling of organic photocontamination on lithographic optics," *J. Vac. Sci. Technol. B*, vol. 18, no. 3, pp. 1306–1313, 2000.

[142] S. F. Cooper, Z. Burkley, A. D. Brandt, C. Rasor, and D. C. Yost, "Cavity-enhanced deep ultraviolet laser for two-photon cooling of atomic hydrogen," *Optics Letters*, vol. 43, no. 6, pp. 1375–1378, 2018.

[143] G. Çelik, E. Çelik, and H. Kiliç, "Calculation of the 1S–2S two-photon excitation cross-section in atomic hydrogen," *The European Physical Journal D*, vol. 50, no. 3, p. 237, 2008.

[144] A. Kawasaki, "Magic wavelength for the hydrogen 1S–2S transition," *Physical Review A*, vol. 92, no. 4, p. 042507, 2015.

[145] C. Adhikari, A. Kawasaki, and U. Jentschura, "Magic wavelength for the hydrogen 1S–2S transition: Contribution of the continuum and the reduced-mass correction," *Physical Review A*, vol. 94, no. 3, p. 032510, 2016.

[146] J. Walraven and I. F. Silvera, "Helium-temperature beam source of atomic hydrogen," *Review of Scientific Instruments*, vol. 53, no. 8, pp. 1167–1181, 1982.

[147] P. Dubé, L.-S. Ma, J. Ye, P. Jungner, and J. Hall, "Thermally induced self-locking of an optical cavity by overtone absorption in acetylene gas," *JOSA B*, vol. 13, no. 9, pp. 2041–2054, 1996.

[148] R. W. P. Drever, J. L. Hall, F. V. Kowalski, J. Hough, G. M. Ford, A. J. Munley, and H. Ward, "Laser phase and frequency stabilization using an optical resonator," *Appl. Phys. B*, vol. 31, no. 2, pp. 97–105, 1983.

[149] T. C. Briles, D. C. Yost, A. Cingöz, J. Ye, and T. R. Schibli, "Simple piezoelectric-actuated mirror with 180 kHz servo bandwidth," *Optics express*, vol. 18, no. 10, pp. 9739–9746, 2010.

[150] D. Goldovsky, V. Jouravsky, and A. Pe'er, "Simple and robust phase-locking of optical cavities with $>$ 200 kHz servo-bandwidth using a piezo-actuated mirror mounted in soft materials," *Opt. Express*, vol. 24, pp. 28239–28246, Dec 2016.

[151] S. Chu, J. Bjorkholm, A. Ashkin, and A. Cable, "Experimental observation of optically trapped atoms," *Physical review letters*, vol. 57, no. 3, p. 314, 1986.

[152] H. Katori, M. Takamoto, V. PalChikov, and V. Ovsiannikov, "Ultrastable optical clock with neutral atoms in an engineered light shift trap," *Physical Review Letters*, vol. 91, no. 17, p. 173005, 2003.

[153] J. Ye, H. Kimble, and H. Katori, "Quantum state engineering and precision metrology using state-insensitive light traps," *science*, vol. 320, no. 5884, pp. 1734–1738, 2008.

[154] M. Stappel, R. Steinborn, D. Kolbe, and J. Walz, "A high power, continuous-wave, single-frequency fiber amplifier at 1091 nm and frequency doubling to 545.5 nm," *Laser Physics*, vol. 23, no. 7, p. 075103, 2013.

[155] T. Meier, B. Willke, and K. Danzmann, "Continuous-wave single-frequency 532 nm laser source emitting 130 W into the fundamental transversal mode," *Optics letters*, vol. 35, no. 22, pp. 3742–3744, 2010.

[156] L. S. Meng, J. K. Brasseur, and D. K. Neumann, "Damage threshold and surface distortion measurement for high-reflectance, low-loss mirrors to 100+ Mw/cm^2 CW laser intensity," *Optics Express*, vol. 13, no. 25, pp. 10085–10091, 2005.

[157] A. Aghajani-Talesh, M. Falkenau, A. Griesmaier, and T. Pfau, "A proposal for continuous loading of an optical dipole trap with magnetically guided ultra-cold atoms," *Journal of Physics B: Atomic, Molecular and Optical Physics*, vol. 42, no. 24, p. 245302, 2009.

[158] M. Falkenau, V. V. Volchkov, J. Rührig, A. Griesmaier, and T. Pfau, "Continuous loading of a conservative potential trap from an atomic beam," *Physical review letters*, vol. 106, no. 16, p. 163002, 2011.

[159] V. V. Ivanov, "Continuous loading of an atom beam into an optical lattice," *Optics Communications*, vol. 324, pp. 258–263, 2014.

[160] M. Scheid, D. Kolbe, F. Markert, T. W. Hänsch, and J. Walz, "Continuous-wave Lyman-α generation with solid-state lasers," *Optics express*, vol. 17, no. 14, pp. 11274–11280, 2009.

[161] D. Kolbe, A. Beczkowiak, T. Diehl, A. Koglbauer, M. Sattler, M. Stappel, R. Steinborn, and J. Walz, "A reliable CW Lyman-α laser source for future cooling of antihydrogen," *Hyperfine Interactions*, vol. 212, no. 1-3, pp. 213–220, 2012.

[162] T. Udem. Personal Communication, 2018.

[163] K. Mølmer, Y. Castin, and J. Dalibard, "Monte Carlo wave-function method in quantum optics," *JOSA B*, vol. 10, no. 3, pp. 524–538, 1993.

[164] J. Helffrich, M. Maley, M. Krusius, and J. Wheatley, "Hydrogen dissociation below 1 K," *Journal of low temperature physics*, vol. 66, no. 5-6, pp. 277–304, 1987.

[165] Y. Nagata and Y. Yamazaki, "A novel property of anti-Helmholz coils for in-coil syntheses of antihydrogen atoms: Formation of a focused spin-polarized beam," *New Journal of Physics*, vol. 16, no. 8, p. 083026, 2014.

[166] T. Bergeman, G. Erez, and H. J. Metcalf, "Magnetostatic trapping fields for neutral atoms," *Physical Review A*, vol. 35, no. 4, p. 1535, 1987.

[167] P. Crivelli and N. Kolachevsky, "Optical trapping of anti-hydrogen towards an atomic anti-clock," *arXiv preprint arXiv:1707.02214*, 2017.

[168] T. Hänsch, S. Lee, R. Wallenstein, and C. Wieman, "Doppler-free two-photon spectroscopy of hydrogen 1S–2S," *Physical Review Letters*, vol. 34, no. 6, p. 307, 1975.

[169] C. Foot, B. Couillaud, R. Beausoleil, and T. Hänsch, "Continuous-wave two-photon spectroscopy of the 1S–2S transition in hydrogen," *Physical review letters*, vol. 54, no. 17, p. 1913, 1985.

[170] M. Boshier, P. Baird, C. Foot, E. Hinds, M. Plimmer, D. Stacey, J. Swan, D. Tate, D. Warrington, and G. Woodgate, "Laser spectroscopy of the 1S–2S transition in hydrogen and deuterium: Determination of the 1S Lamb shift and the Rydberg constant," *Physical Review A*, vol. 40, no. 11, p. 6169, 1989.

[171] R. Kallenbach, F. Schmidt-Kaler, M. Weitz, C. Zimmermann, and T. Hänsch, "High power ultraviolet source with extreme frequency stability," *Optics communications*, vol. 81, no. 1-2, pp. 63–66, 1991.

[172] J. Flowers, "Quantum electrodynamics: A chink in the armour?," *Nature*, vol. 466, no. 7303, p. 195, 2010.